Lock-In Detection with Microfluidic Droplets for Quantitative Bioanalysis in Sub-Nanoliter Volumes

by

Kennon Shane Deal

A dissertation submitted to the Graduate Faculty of
Auburn University
in partial fulfillment of the
requirements for the Degree of
Doctor of Philosophy

Auburn, Alabama
December 14th, 2013

[droplet microfluidics, lock-in detection, on-chip hormone secretion detection, feedback control, soft lithography, segmented flow, variable fluidic resistor]

Copyright 2013 by Kennon Shane Deal

Approved by

Christopher J. Easley, Chair, Associate Professor of Chemistry and Biochemistry
Vincenzo Cammarata, Associate Professor of Chemistry and Biochemistry
Curtis Shannon, Professor of Chemistry and Biochemistry
Wei Zhan, Associate Professor of Chemistry and Biochemistry

Abstract

The following chapters introduce and describe novel droplet microfluidic techniques to assist with limits of detection of analytes with low signal-to-noise ratios. The approach is proven feasible with absorbance measurements over short path lengths and with on-chip protein assays using fluorescence detection. This is accomplished by applying a lock-in detection method to alternating sample/reference droplet formation, which allows for the recovery of low signal in the presence of overwhelming background noise. Also described are methods of droplet formation control through pressure operated variable fluidic resistors in channel. These resistors use thin membranes that deflect into the channels to alter fluidic resistance for adjusting droplet volume and frequency.

The absorbance measurements take place within a 3-channel device consisting of one oil phase channel input and two aqueous channels. The two aqueous channels contain sample and reference solutions. Absorbance measurements are used to obtain a limit of detection (LOD) of 500 nM bromophenol blue (BPB) in a phosphate buffered saline (PBS) solution, as well as to determine the extinction coefficient at varying pH.

On-chip protein assays were performed using a similar device, with the exception of having two reservoirs per aqueous channel and incorporating mixing and incubation regions on the chip after droplet formation. A fluorescence calibration curve was established showing a LOD of 10 pM fluorescein. The proximity FRET (pFRET) assay was used for on-chip hormone detection of thrombin and insulin, resulting in a decrease in fluorescence signal when analyte is present. A calibration curve was created for various concentrations of insulin. Finally, living murine pancreatic islets were loaded into a sample reservoir, then stimulated with 11 mM glucose. Secreted insulin was then mixed with probe and connector and allowed to incubate on-chip for approximately 2 minutes. Fluidic lock-in detection was used to show a decrease in signal as more insulin was released.

Finally, a variable fluidic resistor was developed and used to control droplet size and frequency on-chip. By applying pressure to thin channel ceilings, we were able to increase the fluidic resistance in the channels. Various fabrication approaches were tested, with the two most effective methods involving magnetic pins and using multiple masks to create two separate layers (multilayer photolithography) that could be plasma oxidized then aligned and bonded. The magnetic pin method was capable of fabricating devices that could control droplet size over a few nL, while the multilayer lithography approach gave devices capable of generating wide ranges of droplet sizes and frequencies on the same chip, even in the same channel.

Overall, the work outlined in this dissertation provides proof-of-concept that absorbance and fluorescent detection can be applied to droplet microfluidic devices at low signal intensity with the aid of a lock-in detection method and at high temporal resolution. In conjunction with frequency and volume control over the droplets through the use of variable resistors, this should allow further advances in on-chip, stimulated hormone secretion analysis.

Acknowledgments

My time as a graduate student in the Easley lab has been some of the most memorable years of my life. I want to share a few things about our lab that have been entertaining over the years. There will never be a shortage of tape, ever. That joke never gets old. Second, there are 3 movies every future group member should be able to quote. Learn which ones they are. Third, we learned calculus in kindergarten. Fourth, be alert because there is always a chance of flying pieces of paper or someone lurking around a corner to scare you. And finally, take care of the plants. They are just as much group members as we are. So with all that being said, there are several people I need to thank. First of all, without the support and help of my family, I never would have made it this far. I love you and respect you more than I can ever tell you. Dr. Christopher Easley, I can't thank you enough for your mentoring, your intelligence, your sense of humor, and most of all, for your patience! Dr. Kim and Dr. Ashby, thank you for all the help. Whether it was experimental, computer, or career related, it was invaluable. Leah, without you I'm not sure I would have made it this far. Thank you for the pep talks, the entertainment talks, keeping me up to date on music, the hidden notes, and allowing me to constantly scare you. Cheryl, continue to be the classiest member of the Easley group! Jessica, aka 'Grace', you are a constant source of energy. I hope you never lose that. Louis, Zac, and Ricky have to be the most focused, intelligent undergrads I have ever had the privilege of working with. I expect great things out of all three of you. To the rest of the Easley group, Jiaming, Jean, Xiangpeng, Subramaniam, Haley, Lauren, Ferdous, Amanda, and even Rebecca and Meagan, I cannot thank you enough for all the fun talks, great discussions, and memories over the past 5 years. Mike, we have been roommates for years, and I don't believe there is a more dependable person in Auburn. To the Auburn Chemistry and Biochemistry incoming graduate class of 2008, I wish you nothing but success and hope that we continue to stay in touch. Matt Smith, I couldn't ask for a better friend. I appreciate all the words of encouragement and all the laughs. To the entire Mundy family, thank you for everything. You have made me feel like a part of your family from day one. Steven and Tara Rowe, you have no idea how much our dinners together meant to me. To my committee members: Dr. Cammarata, Dr. Shannon, Dr. Zhan, and my outside reader Dr. Park, thank you for all your advice and intelligence over the years. I know it is a time-consuming job, and I truly appreciate your efforts. To the office staff, Kiley, Mrs. Lynn, and Mrs. Carol, I cannot thank you enough for all the help with our travel arrangements, reimbursements, and credit hours. You three are essential to this department. Kat West and Vesko, you guys made Organic labs way more enjoyable than they ever should have been. And finally, to the entire Auburn University Chemistry and Biochemistry department, as well as COSAM, your commitment to our success and the support you provide is unrelenting.

Thank you all.

Kennon Deal

Table of Contents

List of Tables

List of Figures

List of Abbreviations

LOD	Limit of Detection
BPB	Bromophenol blue
PBS	Phosphate Buffered Saline
pFRET	proximity Förster Resonance Energy Transfer
AMSTC	Alabama Microelectronics Science and Technology Center
PDMS	Polydimethylsiloxane
SAWs	Surface Acoustic Waves
MACS	Magnetic Activated Cell Sorting
FACS	Fluorescent Activated Cell Sorting
MS	Mass Spectrometry
PCR	Polymerase Chain Reaction
DMF	Digital Microfluidics
TTM	Toner Transfer Masking
DNA	Deoxyribonucleic Acid
ELISA	Enzyme Linked Immunosorbent Assay
NESA	Nicking Enzyme Signal Amplification
ddRPA	digital droplet Recombinase Polymerase Amplification
PC-PDMS	Photo Curable PDMS
ROI	Regions of Interest

FFT	Fast Fourier Transfer
POC	Point of Care
μTAS	Micro Total Analysis System
NIH	National Institutes of Health
PLA	Proximity Ligation Assay
BSA	Bovine Serum Albumin
DAQ	Digital Data Acquisition
PMT	Photomultiplier Tube

Chapter 1: Introduction

1.1 Microfluidic Background and Developmental Years

1.1.1: Microfluidic History

Microfluidics has grown into an encompassing field in the scientific community since its humble introduction in the 1970's with gas chromatography [1]. When fabrication began including polymer substrates, plastics, and even paper in the 1990's instead of only silicon and glass, its notoriety began to grow in research labs worldwide. In only a few decades, this has sparked the development of several commercial entities and suppliers of microfluidic devices. Applications that devices have been and may eventually be supplied for include miniaturized analytical systems for chemistry and biochemistry, biomedical research devices, and systems for fundamental research. The success of these corporations is not only attributed to fabrication processes, however. Advancements in surface coatings, optics, acoustics, mechanics, and microelectronics have all lead to the increased popularity of microfluidics.

But what does it take for a device to be considered microfluidic? In most cases, a device is categorized as "microfluidic" if the geometries of the channels are in the range of hundreds of µm or less and if the volumes associated in these channels are in the range of nanoliters or less [2-5]. The next question to be answered is why even use microfluidic devices? What are the benefits associated with a microfluidic system? How does it help? There are several characteristics that make microfluidic platforms promising alternatives to large scale devices. It is now possible to carry out chemical reactions in small volumes, at a high frequency, and at a minimized cost [4]. Another major benefit of microfluidic devices is the ability to integrate several different processes onto the same device. Controlling and manipulating miniaturized volumes on the same platform allows for extremely robust systems. The first commercially available devices produced were ink jet (or bubble jet) printers developed by IBM in 1979. The opportunity for cheap, portable, and disposable devices along with the ease of integrating multiple functions on one device makes them a great choice for field applications. Point of care applications or air quality testing requires portable, robust systems that need very little outside equipment for operation. Creating devices capable of droplet formation is also beneficial in a lab environment as well and is the driving force for the majority of the work that will be discussed here.

1.1.2: Droplet Microfluidics

First, microfluidic devices can achieve extremely high frequencies of droplet formation. Several devices are capable of creating droplets at kilohertz frequencies. Keeping in mind that each of these droplets can be considered an individual reaction vessel; it becomes possible to use the droplets as compartments for reactions to progress in an isolated, individual manner in a reasonably small time period. Microfluidics allows for thousands of picoliter to nanoliter scale reaction droplets to be generated quickly using minimal reagents. This, in turn, greatly reduces the overall cost of research being performed. Published in 2001 in *Physical Review Letters* by the Stephen Quake group is the first article that shows monodisperse droplets being formed on a chip (**Figure 1.1)** [6]. The article goes on to discuss the importance that these types of devices carry and begins to describe the many possible uses. Since then, that list of applications has grown quite rapidly in diverse fields of scientific research. These devices can be quite complex requiring syringe pumps, external power supplies for valves and fluid flow control, computers for controlling various electronics and data analysis, and storage of reagents. On the other hand, they can be quite simple for use outside of a laboratory setting. For example, as presented in this dissertation work, the use of handheld syringes is an effective and efficient way to provide the necessary pressure or vacuum to enable fluid flow and droplet formation at these high throughput values. [7]

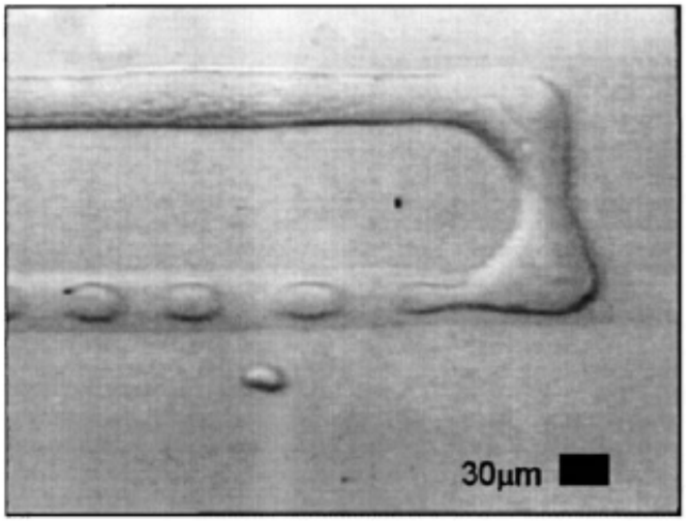

Figure 1.1 Image of the first droplet-forming microfluidic device that was capable of creating monodisperse aqueous-in-oil droplets, as presented by the Quake group in 2001. Reprinted figure with permission from [6]. Copyright 2001 by the American Physical Society.

1.2: Droplet Microfluidics with PDMS

1.2.1: Design and Fabrication of Microfluidic Devices

The production of microfluidic devices for droplet formation begins with an idea for a channel design that should form a particular droplet scheme for uses such as droplet detection, islet secretion sampling, emulsion recovery, etc. Our laboratory creates channel designs using Adobe Illustrator. Restricting all features to a 1” x 1” region allows for the use of glass slides as the foundation substrate. Typically, designs will go through 4-5 iterations from the start of a project until the design is finalized. Once the design is finished, it is sent to Fine Line Imaging (Colorado Springs, Colorado) to create a negative photomask of the Illustrator design. These masks are capable of 5 μm resolution, which is well within fabrication limits of the photoresist. Once the mask is complete, photolithographic techniques are used to create silicon-based masters using the Alabama Microelectronics Science and Technology Center (AMSTC) clean room at Auburn University. A common practice involves using a product named SU-8 to create these masters [8], which is a negative photoresist designed for spin-coating to micrometer-scale depths. This product forms through a photopolymerization process that occurs after a photoacid generator is exposed to ultra-violet (UV) light—in the pattern of the photomask—and creates a cationic chain growth when epoxide ring groups on the SU-8 molecules open (**Figure 1.2**). SU-8 activation is carried out with flood UV light source available with most mask aligners, as well as some lower-precision hand-held devices. A broad range of thicknesses can be created by simply adjusting the spin-coating speed and SU-8 viscosity. Depths range from hundreds of nm through the 500 μm range. For PDMS channels, a width-to-depth aspect ratio of ≤10 is stable and avoids collapse in most instances. Even if channels require a higher aspect ratio, simply including support posts in the channels will prevent collapse of the channel ceiling. For device master fabrication, SU-8 photoresist (MicroChem) is first spin-coated onto a silicon wafer, then a photomask is used to mask UV light exposure in the pattern designed in Adobe Illustrator (**Figure 1.3**). The SU-8 that was not exposed to UV is removed from the wafer, leaving only the chip design. The heights of channels are determined by the viscosity of SU-8 used and by the speed (rpm) used on the spin coater. In this dissertation work, 35-µm depths are used for most channels, but depths sometimes vary depending on the design. Heights up to 100 µm have been used for some chips. After baking, the SU-8/silicon wafer master can be used as early as the next day to create chips via a soft lithography process [3].

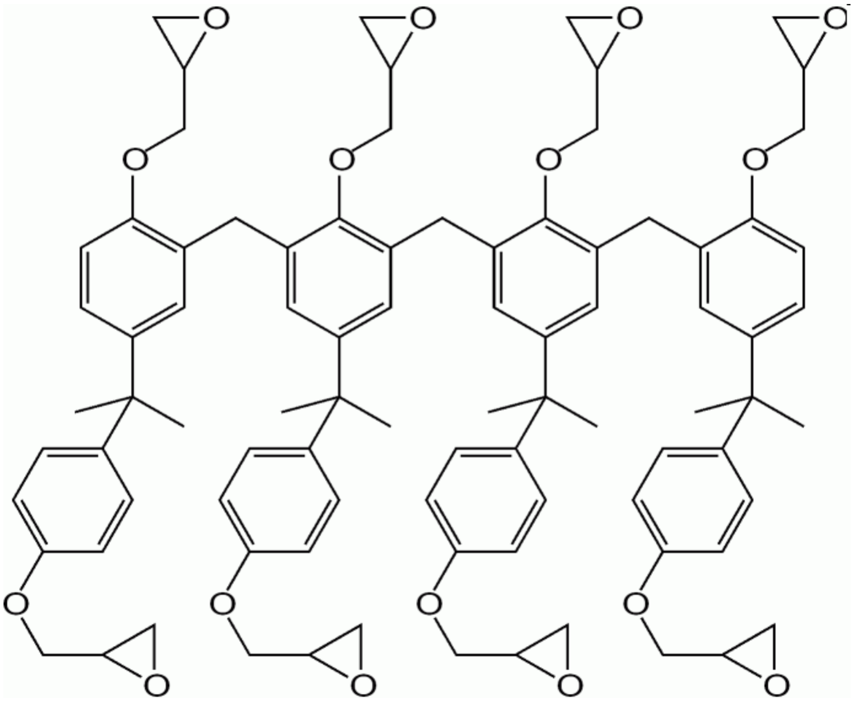

Figure 1.2 SU-8 photoresist after cationic photopolymerization induced by Lewis acid regeneration.

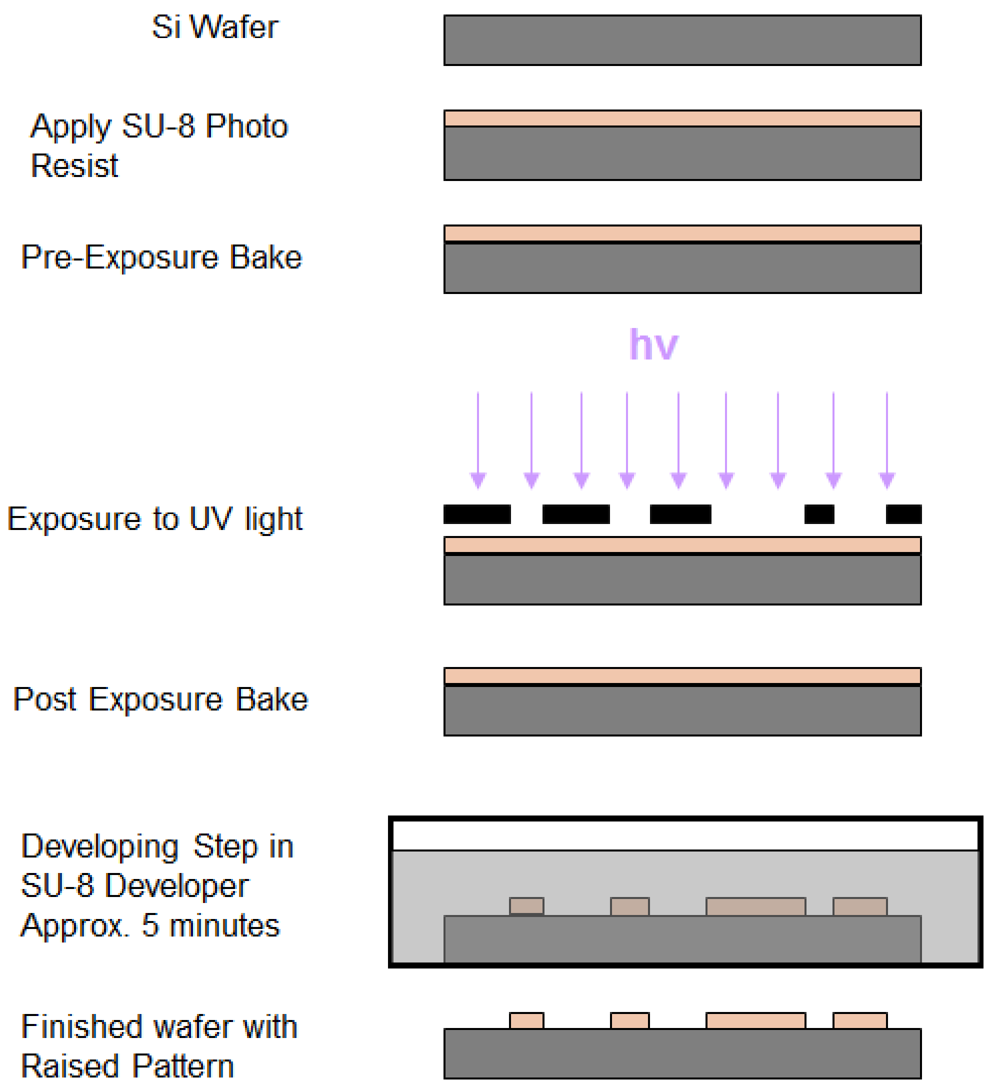

Figure 1.3 Illustration of the steps involved in creating a silicon/SU-8 master for PDMS device molding. Starting with a blank wafer, photoresist is applied by spin-coating. Next, a pre-bake, UV exposure, then post-bake are carried out, followed by a developing step to remove uncured SU-8. Leftover positive-relief SU-8 features serve molds for channel patterns in PDMS.

The soft lithography process [3] consists of casting a polymer, polydimethylsiloxane (PDMS), onto the mold to generate SU-8 defined channel designs within the PDMS. Each of our wafers usually contain six 1” x 1” designs. After curing, PDMS devices are carefully removed from the wafer, each of the 6 individual chips are cut into individual devices, and reservoirs are punched for the aqueous and oil solutions. Typically, one outlet is punched in order to connect the vacuum tubing to the chip. The chip is then cleaned with methanol, dried with air, then bonded to either a glass slide or another piece of PDMS through various methods. The most commonly used bonding methods are plasma oxidation and partial curing. Plasma oxidation uses reactive oxygen radicals to attack the Si-CH_3 groups and convert them to Si-OH groups (**Figure 1.4**). When two plasma oxidized surfaces come into contact within a few seconds of exposure, a condensation reaction between the silanol groups occurs, creating a strong bond capable of withstanding high pressures. Experiments have shown pressures as high as 300 kPa can be applied to chips with no breakthrough occurring. For partial curing, we place pieces of PDMS that are not completely cured into physical contact with one another. Essentially, uncured base from one piece interacts with the curing agent from the other piece, and the polymer chains cross link to form one piece of PDMS. Again, this forms a strong bond and makes it possible to eliminate glass substrates if desired.

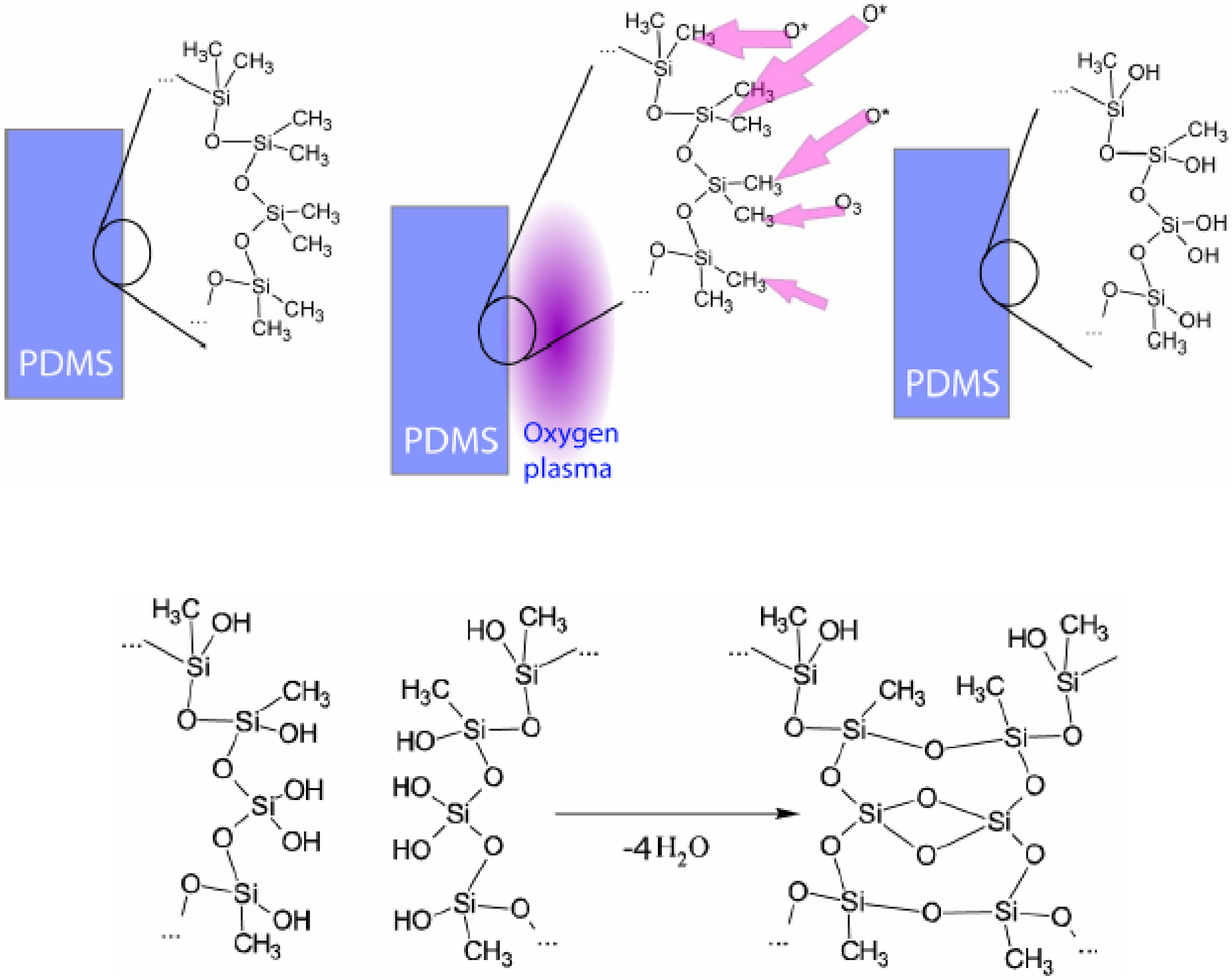

Figure 1.4 Process that occurs during plasma oxidation of glass or PDMS. Oxygen radicals convert methyl groups to hydroxyl groups. When two pieces come into contact, a condensation reaction occurs between the silanols. Used with permission from ‘Valves for Microfluidic Devices’ Alar Ainla, Thesis, 2008.

It is noteworthy that PDMS is not the only polymeric material used in microfluidic device fabrication. It is possible to make microfluidic devices in many ways, even from glass or silicon substrates. There are even methods that do not involve clean room techniques. Fabrication can be as simple as using adhesive tape and an oven to bond layers. These methods are simple, thus the designs are typically at low resolution and not very complex [12]. Other methods use PDMS to create complex designs by sandwiching many thin layers with various patterns and interconnecting them to form three dimensional devices for wide ranges of applications [13]. Single layer devices are more common—based on ease of fabrication—but multilayer design concepts are being continuously developed. Lately, for example, the Landers group has used laser printer lithography along with poly(ethylene terephthalate) to pattern valves in microfluidic devices. This technique was successfully applied to DNA analysis experiments such as amplification and extraction [14]. Many techniques involve coating of the channel surfaces with various compounds or extraction processes with a range of solvents. For our purposes, however, we have chosen PDMS as a microfluidic device substrate, based on its optical transparency, gas permeability for biological studies, ease of fabrication and replication, and the robust nature of the completed devices [3, 15]. As such, additional PDMS properties and surface treatment procedures are outlined below.

1.2.2: PDMS Fundamentals

All devices used in this research are made from polydimethylsiloxane (PDMS). PDMS is an inert, non-toxic, transparent copolymer that is gas permeable and consists of a chain of repeating siloxane units (**Figure 1.5**). It is formed by mixing a monomer solution with a curing agent/catalyst combination solution. Optimal monomer/curing agent ratios will vary depending on the desired properties of the material, but we most commonly employ a ratio of 10:1 (monomer:curing agent). Once the silcon/SU-8 wafer is fabricated, microfluidic chips can be made from PDMS within 2 hours, from start to finish. It is straightforward to bond this material to glass substrates or to another piece of PDMS through plasma oxidation or partial curing as previously described. Although using PDMS for microfluidics is relatively common, there are a few properties associated with PDMS that must be understood and dealt with to promote ideal droplet formation.

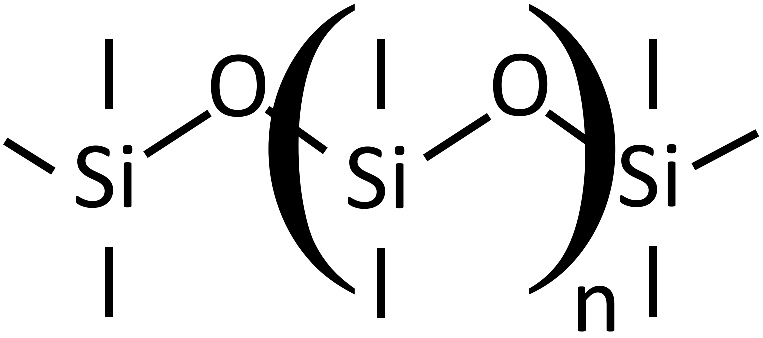

Figure 1.6 A representation depicting the polymer chains of PDMS.

1.2.3: Characteristics of PDMS microchannels

Surface composition, and sometimes even channel shapes, of PDMS have a tendency to vary over time due to the presence of uncured monomers. Once the PDMS has cured, the channel walls of the device are typically hydrophobic [9]. After plasma oxidation, they become hydrophilic for a period of time due to the creation of radicals on the surface. It has been shown that this only lasts for a period of a few hours, if not minutes, as they become hydrophobic through the reorganization of unlinked monomers [11]. This can be problematic, because it prevents a chip from maintaining consistent surface characteristics. PDMS can also allow various molecules to partition through the surface, which can cause bulk material swelling or surface fouling. These issues are related to the ratios of monomer and curing agent components used. Although problems can be caused by these effects, methods do exist to make device characteristics more consistent, as discussed in section *1.2.5*.

1.2.4: Partitioning and Swelling

Although cured PDMS is considered largely inert, there are some solvents that will affect its structure and material characteristics. These solvents actually penetrate into the walls of the channels when in contact with the PDMS. Some materials cause severe swelling of the PDMS which results in cracking as the solvent is removed, while other substances, such as some fluorescent dyes, will partition into the walls and permanently stain the PDMS. When this occurs, the dye is difficult to remove and the chip is rendered useless for fluorescence detection and other applications. The Whitesides research group has performed an extensive investigation into PDMS swelling ratios with various solvents [10]. Their compiled list, shown in **Table 1**, ranges from solvents that have little to no effect on PDMS such as mild swelling through devastating effects such as drastic swelling and cracking of the polymer, making it several times larger than its original size. **Figure 1.6** demonstrates the partitioning by showing a channel with silicone oil with a concentration of Di-I, a fluorescently labeled alkyl chain, mixed into it. Images were taken at various times after to show the rates of partitioning into the channel wall. Thus, users should take care in choosing solvents and fluorescent labels that will be loaded into PDMS devices.

Table 1:

Solvent	Swelling Ratio
water	1.00
glycerol	1.00
dimethyl sulfoxide (DMSO)	1.00
acetonitrile	1.01
dimethylformamide (DMF)	1.02
acetone	1.06
1-propanol	1.09
dioxane	1.16
ethyl acetate	1.18
chlorobenzene	1.22
benzene	1.28
toluene	1.31
cyclohexane	1.33
hexanes	1.35
ether	1.38
chloroform	1.39
xylenes	1.41
pentane	1.44
triethylamine	1.58
diisopropylamine	2.13

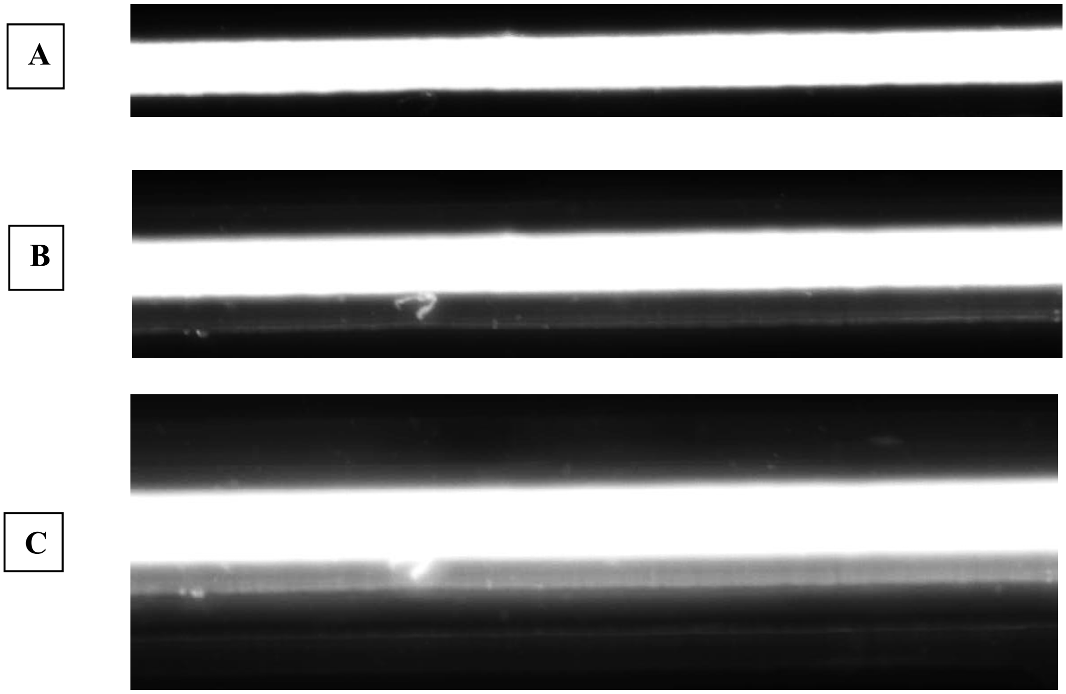

Figure 1.6 Partitioning of a fluorescent dye (DiI) into PDMS. A) Time zero. B) After 10 minutes. C) ~80 minutes.

1.2.5: Controlling surface characteristics

Although these characteristics are troublesome, other desirable properties of PDMS outweigh the drawbacks; for this reason, others have undertaken methodological research toward controlling swelling and partitioning phenomena. The Henry research group has shown that an extraction process can remove the free oligomers within the PDMS to prevent migration and surface fouling [11]. This extraction process uses 3 solvents in 2-hour washes to remove the unbound oligomers. With fewer oligomers present, the surface characteristics were shown to be stabilized for 7 days or more. Although this method works well, it is time consuming and requires several solvents and significant hands-on time.

One method that our group has employed to limit the amount of free monomers is to increase the PDMS curing time. The more it cures, the more the oligomers cross-link, and the less they are free to migrate to the surface. To test this approach, an experiment was designed to analyze the amounts of remaining monomers during differing PDMS curing times. Monomer amounts were measured by weighing pieces of PDMS (from the same batch each time), extracting monomers using the trio of solvents [11], drying the solvents from the PDMS, then weighing the remaining PDMS. The amount of uncured monomer was obtained from the weight difference from before and after extraction. PDMS samples that were cured from 30 minutes to 24 hours were tested with this approach.

After each sample was cut from the bulk PDMS, it was placed on the scale in order to obtain an original mass, usually around 2.5 grams, then immediately placed in the freezer to stop the curing process. Once all samples were ready, they were thawed, and the extraction was performed on each sample. After extraction, all samples were placed in an oven at 65 °C to remove all solvents. During drying, each sample was weighed several times over a period of a few hours to make sure the final weight was consistent and ensure that all solvents were removed. When the mass was consistent, it was compared to original mass after curing, and the percent difference for each sample was graphed (**Figure 1.7**). From this data, it was apparent that the longer the PDMS is cured, the less oligomer (by percentage) is present, as expected. Based on Henry's result we expect that for PDMS with long curing times, less monomer will be available to migrate and affect the surface [11]. Thus, by simply curing overnight, PDMS surface characteristics can be made more stable. In practice, we have observed that a chip can be used after a two hour cure if there is a need for a quick test, but in this case there is little hope of the surface characteristics being stable. Combining a long cure with any subsequent surface treatments allows chips to maintain consistent characteristics for more extended periods. This result is similar to Henry's result, but with a much simpler approach; further study may be warranted to fully characterize this approach [11]. A commercially available perfluorocarbon glass-coating reagent, Aquapel, is applied to the walls of channels in droplet generating devices discussed in this dissertation. Aquapel is an autophobic, perfluorocarbon-based water repellent that chemically bonds to PDMS microchannel walls via silanization in a matter of seconds. Filling up the reservoirs in a microfluidic device, then applying a vacuum to flow the liquid through the device provides consistent channel surfaces that are wetting to perfluorocarbon oils.

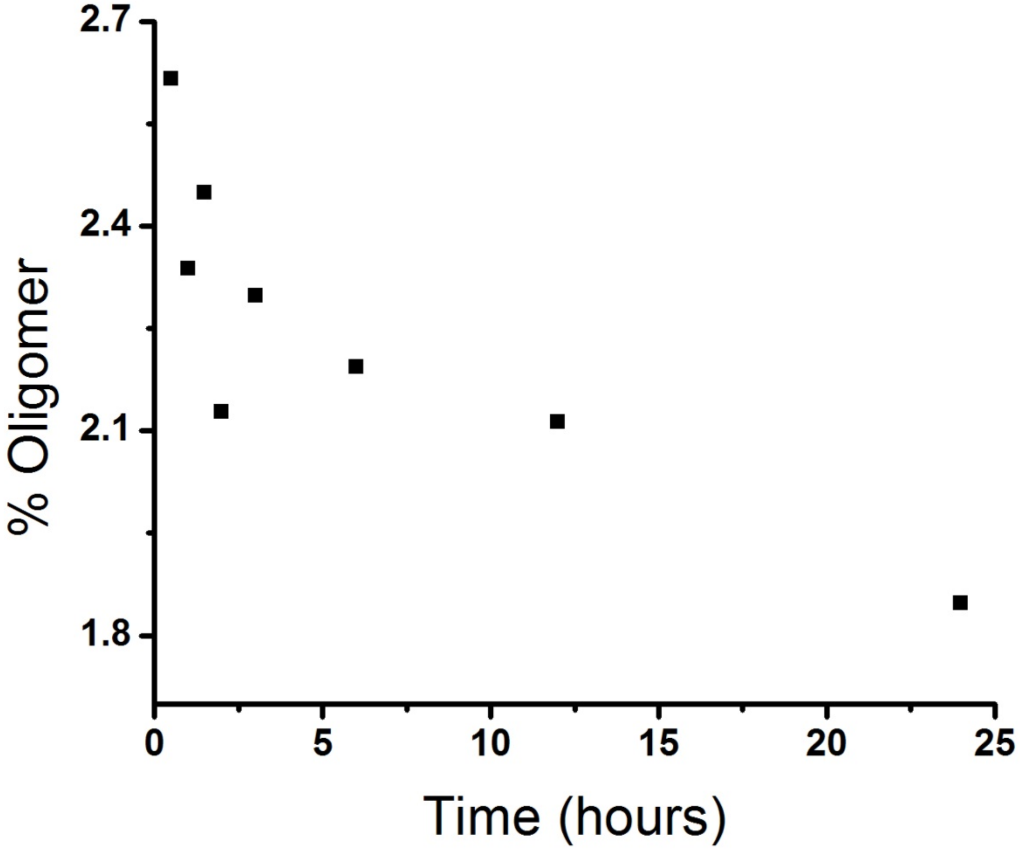

Figure 1.7 Graphical representation of the effects of curing time versus percent uncured oligomer, as calculated by comparing starting mass of PDMS to mass after curing and oligomer extraction.

1.3: Droplet Formation

1.3.1: Dynamics in Microchannels

1.3.1.1: Capillary Number

Three parameters are typically used to describe droplet formation in a microfluidic device. They are the dimensionless capillary number and Reynolds number, as well as the Young-LaPlace pressure. Each one describes a different aspect of fluid flow within a device. They can be used together to predict if a particular microfluidic system will allow droplet formation to occur and if the device can be used for a specific function. The capillary number describes the effect of the viscous forces versus the surface tension acting on an interface. The formula is as follows:

$$Ca = \frac{\mu V}{\gamma} \qquad \text{Equation 1}$$

where μ is the fluid viscosity, V is the velocity, and γ is the surface tension. For most microfluidic devices these are liquid-liquid interfaces [16]. *Ca* is a dimensionless number ranging from $10^{-8} – 10^{-2}$ and can be used to determine the droplet coalescence probability within a device and whether or not droplets will even form. Coalescence will occur at lower capillary numbers making the device unusable for droplet applications.

1.3.1.2: Reynolds Number

The Reynolds number is a way to characterize the flow of fluid through a channel and is the ratio of inertial forces to viscous forces.

$$Re = \frac{\rho V L}{\mu} \qquad \text{Equation 2}$$

Re is determined by the density (ρ) of the fluid, the mean velocity of the fluid (v), a characteristic length (L, depth and width) and the dynamic viscosity of the fluid (μ), and it is also a dimensionless number [17]. The Reynolds number, Re, can describe the type of flow that occurs in a device, either turbulent or laminar (**Figure 1.8**). Nearly all microfluidic devices exhibit non-turbulent, laminar flow because of the small size or mass and correspondingly small inertial values. Reynolds numbers of 100 or less results in completely laminar flow, and many microfluidic systems exhibit $Re < 1$.

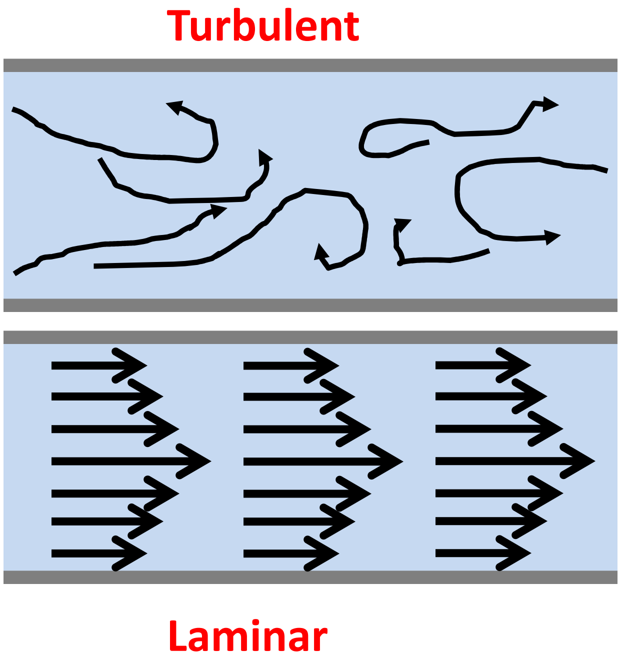

Figure 1.8 Different types of flow that is possible in a channel depending on the respective Reynolds numbers.

1.3.1.3: Young-Laplace Equation

The Young-LaPlace pressure is a description of the relationship between the pressure differential across a fluid interface and the curvature of that interface.

$$\Delta P = \gamma\left(\frac{1}{R_1} + \frac{1}{R_2}\right) \quad \text{Equation 3}$$

Related to the surface tension and droplet size, the Young-Laplace value is a description of the pressure difference between the interior of the droplet and that of the continuous phase (**Figure 1.9**) [18]. Smaller droplet radii give higher curvatures and thus a higher pressure difference across the interface. A 100-µm droplet will have a pressure difference of approximately 0.028 atm, whereas a 10-nm droplet will have a pressure difference of 280 atm, if the surface tension is 0.071 mN/m in an oil/pure water system. It is clear from this analysis that smaller droplets are less stable without manipulation of the surface tension.

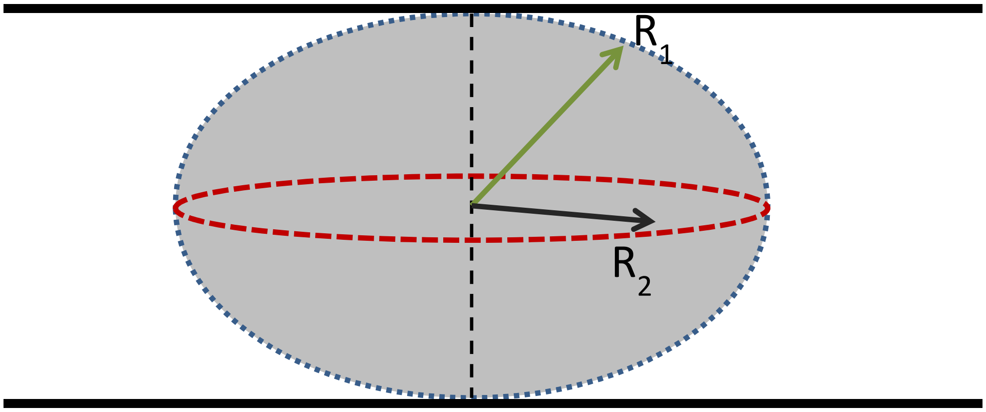

Figure 1.9 In order to calculate the Young-LaPlace pressure difference, the two radii of a droplet along with the surface tension at the fluidic interface must be known. Respective radii are shown in this illustration.

1.3.2: Surfactants

Droplet-based experiments for *in vitro* and *in vivo* biological systems have proven themselves beneficial. These systems provide the high throughput capabilities, precise volume control, reagent addition, incubation, and detection all on one platform [19-21]. The minimum requirement for picoliter to nanoliter scale biochemical reactions is that the droplets remain individual droplets without coalescence for the entire reaction. Therefore, surfactants are required in order to stabilize droplets throughout the entire process of a drop based experiment. Unfortunately, biocompatible surfactants that promote high droplet stability are rare. After droplet formation and especially when incubation steps are required, stabilization is needed when droplets are tightly packed against each other in enclosed channels. Surfactants stabilize the droplet interface and assist with the biocompatibility of reagents. To assist in droplet formation, surfactants are included in the carrier oil. There are several carrier oils available commercially and several others reported in literature. These are chosen based on the various phases being used, substrate material to prevent any unwanted interactions, and the application. Surfactant is coined from 'surface active agent,' and these molecules contain hydrophilic and hydrophobic moieties that drive the surfactant molecule to the surface of the droplets. This in turn lowers the surface tension and prevents droplet coalescence [22-24]. We have used two different surfactants depending on the requirements of our experimental system. Either Krytox, from DuPont, or Jeffamine-bound Krytox, made in house, is added to the carrier oil, which is HFE-7500 perfluorocarbon oil from 3M. One of the surfactants is a product produced by DuPont called Krytox-157 FSL (**Figure 1.10**). The 'L' stands for low molecular weight. If droplet formation is the only concern, Krytox works well. This combination is formed by dissolving it in methanol then converting the Krytox into an ammonium salt and allowing the solvent to evaporate. The leftover viscous material can then be dissolved into the perfluorocarbon oil, HFE-7500. The second surfactant is made with an aqueous Jeffamine additive with Krytox, using a method developed in-house [25]. If we are using proteins in the investigation, Jeffamine additives are used to prevent protein precipitation at the droplet surface. These combinations of carrier oil and surfactant prove most beneficial.

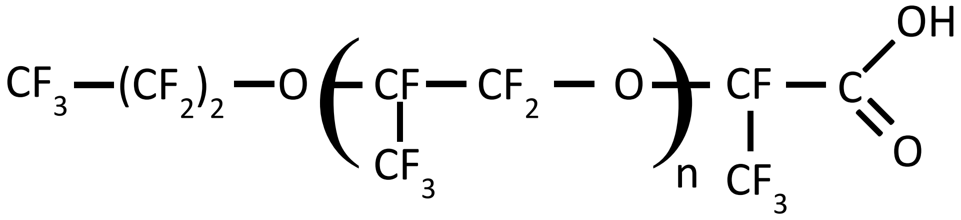

$$CF_3-(CF_2)_2-O\left(-\underset{CF_3}{\underset{|}{CF}}-CF_2-O-\right)_n\underset{CF_3}{\underset{|}{CF}}-C\overset{OH}{\underset{O}{}}$$

Figure 1.10 Krytox, whose structure is depicted above, is a surfactant manufactured by DuPont that was used with our carrier oil to stabilize droplets.

At this point, with device design and surfactant chosen, droplet trains can be formed with minimal effort. One must simply take the device out of the oven, insert tubing, fill reservoirs with carrier phase and aqueous phase, and pull a vacuum with a hand-held syringe. It usually takes less than 2 minutes to form stable, consistent droplets. There are various geometries used for droplet formation. Depending on the application, each has specific characteristics that can be used to determine which one is best suited for that particular device.

1.3.3: Droplet Formation and their Geometries

There are several designs for droplet formation used frequently in microfluidics today. All have their usefulness for certain applications. All allow for monodisperse, consistent size and shape of droplets as opposed to creating droplets through bulk emulsification, which results in drops of varying sizes and characteristics. The following droplet generation techniques allow for minimal droplet size variation, usually less than 2%, as well as frequency control. These methods exploit channel geometries, flow rates, surface characteristics, and shear forces that are unique to each approach [26, 27].

1.3.3.1: T-Junction

One of the more common systems—and the method of choice for our laboratory—employs oil and aqueous channels that come into contact with one another in a perpendicular fashion that resembles a capital 'T'. Since the majority of experiments presented in this dissertation utilize the T-Junction droplet formation scheme, it is important to understand the physics behind this droplet formation. There are 4 steps to droplet formation in a T-Junction device: 1) The aqueous phase enters the main channel, 2) The aqueous portion begins to block the main channel, 3) The droplet gets larger in the main channel and is forced downstream, 4) The droplet is separated from the bulk aqueous phase. During this process, there are 3 main forces that act on a liquid during droplet formation: shear stress force, surface tension force, and the increasing resistance due to flow around the droplet as it increases in size. These will be discussed briefly. Shear stress force is exerted on the forming droplet by the continuous phase. This force is calculated based on the continuous phase flow rate and the size of the gap between the immerging droplet and the channel wall. As a droplet gets bigger, the larger downstream side is more stable, and the increase in pressure pinches the smaller upstream side of the droplet against the aqueous phase channel wall. The surface tension force on the droplet is related to the radial and axial curvature of a droplet and is directly correlated to the Laplace pressure on that droplet. There is a pressure drop that occurs in the liquid along the main channel axis towards the small side of the droplet. It is a combination of this pressure drop and the shear stress from the continuous phase that distorts the droplet in the downstream direction. Resistance occurs as the droplet enters the continuous phase channel and begins to block it. The larger it becomes, the more resistance occurs until finally the flow of the continuous phase separates the droplet from the main aqueous phase and forces the droplet downstream. It is speculated that this increase in resistance is the leading contributor for droplet detachment in the channel.

Based on this mechanism, the geometries of the channels (the ratio of width and height to the continuous and aqueous phase) become extremely important in determining the size of the aqueous phase portion entering the continuous phase. The values of these forces depend on the sizes of drops and the relationship between the drop size and channel size. Droplet formation is highly dependent on the capillary number (*Ca*) of the two flows. As the aqueous phase begins to protrude into the continuous phase, a pressure gradient begins to occur as shear forces and interfacial tensions are thrown out of balance where the two phases intersect. As the aqueous droplet gets bigger, it is forced downstream by the continuous phase until the back of the droplet becomes very thin. When this occurs, the shear force clips the aqueous phase, the droplet is formed, and is carried downstream with the continuous phase. The pressure gradient is decreased, and the aqueous phase retreats into the aqueous channel until the pressure on that channel forces the aqueous phase into the continuous phase again, repeating the cycle for each drop. For this droplet formation, not only is the capillary number important, but also the viscosity of the two phases, the flow rates of each, and the ratio of the channel geometries to each other. Typically, at high capillary numbers, these droplets are smaller than the channel they are formed in as a result of the drag accompanied with the continuous phase. Lower capillary numbers result in droplets that are larger than the channel due to a plug effect that occurs because the continuous phase drag is not as high. The aqueous phase is allowed to grow large enough to block the channel until the continuous phase pressure becomes high enough to force the aqueous phase into a droplet and downstream (**Figure 1.11)** [28-30].

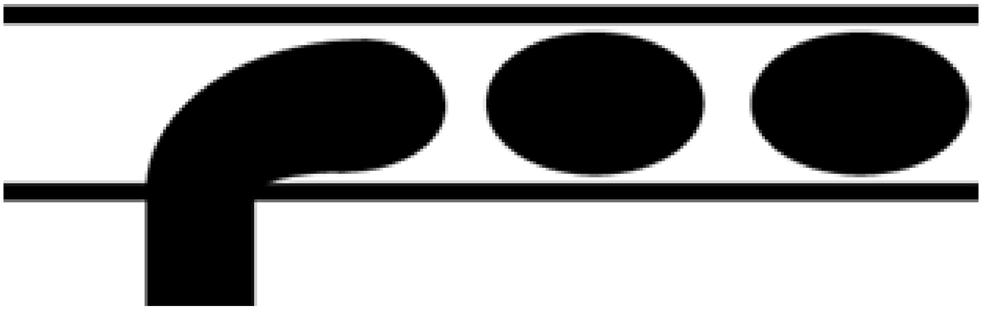

Figure 1.11 T-junction aqueous-in-oil droplet formation with black ovals representing the aqueous phase droplets.

1.3.3.2: Flow Focus

For this method of droplet formation, symmetric channels containing the continuous phase surround the aqueous phase. As the aqueous phase flows into the open channels, the continuous phase forces the aqueous phase through a small orifice leading into a larger channel with more continuous phase. Droplets are formed as both phases are forced through the orifice. The continuous phase provides pressure to drive the droplets through as well as the shear forces to separate the phases into different droplets. This design allows for more controllable droplets by simply changing flow rates or surfactant concentrations in the continuous phase or by changing the device geometry such as the orientation of the symmetric channels or their size in comparison to the aqueous phase. Emulsions, which are heavily used in personal care products, foods, and topical drug delivery, require droplet production control in order to maintain uniformity. There are several methods for making emulsions but the majority use large batches of two immiscible liquids, leading to polydisperse droplets with a wide range of sizes formed. For flow focusing techniques, droplet size, velocity, and frequency can be tuned through controlling the flow rates, controlling the inlet pressures, varying the phase viscosities, and controlling the orifice size **(Figure 1.12)** [31-33].

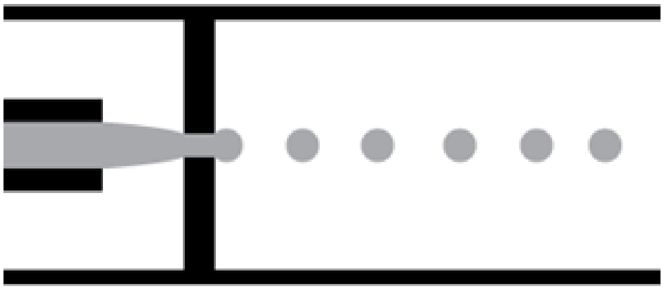

Figure 1.12 Representation of Flow Focus droplet formation with aqueous phase (gray) surrounded by continuous phase and 'focused' through a narrow opening to create the droplets.

1.3.3.3: Co-Flow

There are two basic types of co-flow systems. Dripping and jetting are highly dependent on the flow rates of the liquids. Water running from a kitchen faucet demonstrates both of these phenomena depending on how fast the water is flowing. At low flow rates, dripping is the predominant regime and is the product of an absolute instability as the forces acting on the stream of water occur at a specific frequency and location in the stream. At higher flow rates, jetting is predominant and is the result of convective instabilities. As water flows out of the faucet at a higher rate of speed, the effects that lead to droplet break-up travel along the jet of water and become more random as they interact with the continuous stream. If monodispersed droplet formation is required, a system affected by absolute instabilities would be desired. In a microfluidic set up, this is achieved through careful control of the dynamics affecting the droplet formation. Co-flow systems are also highly dependent on fluid velocities, viscosities, surface tension and the densities of the liquids. The geometry of the droplet formation region in the microfluidic device is important as well. Co-flow in microfluidics occurs as aqueous phase is forced through a small capillary that is contained and centered inside a larger diameter channel with continuous phase flowing parallel to the aqueous phase. As the continuous phase surrounds the aqueous phase, the viscous shear force becomes larger as the diameter of the aqueous phase increases. Eventually, the drag and interfacial tension force equal each other at the tip of the capillary and a droplet forms and is pinched off from the aqueous phase still inside the capillary [34, 35]. By establishing an absolute instability in the system and optimizing all the variables, droplets can be formed at uniform frequencies and sizes (**Figure 1.13).**

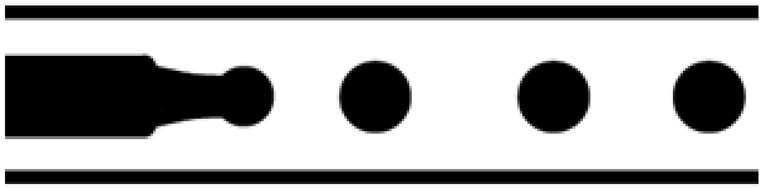

Figure 1.13 Representation of Co-Flow droplet formation with black circles representing aqueous phase.

1.3.4: After droplet formation

Once droplets have been formed, there are many downstream techniques used on the droplets, depending on the manner they are being utilized. Mixing, encapsulation, storage, sorting, and sensing have all been performed with great success. It is the ability to perform these steps on-chip that allows microfluidic designs to serve so many different purposes.

1.3.4.1: Mixing

The majority of reactions involving microfluidic droplets require some combination of reagents to be mixed together. If temporal resolution is important—as is the case with some of our applications—the reagents should not be mixed then loaded on the chip before droplet formation. Instead, it is better to load all reagents individually on the chip, and then combine them into a droplet at the same time. This allows for the timing of reactions to be controlled. Unfortunately, at this scale, mixing is not easy to accomplish. Flow is generally laminar throughout the channels, so no turbulent mixing occurs. The only method of mixing is molecular diffusion, which is generally not fast enough for the amount of time the droplets spend on the chip. Therefore, it is necessary to create some type of mixing region for most multi-reagent experiments. These range from passive operation to active operation mixers utilizing geometric designs or external fields, respectively [36-40]. Passive operation generally uses a set of turns in a channel or uneven patterns on the surfaces of the channel to create a chaotic regime (**Figure 1.14).** Active mixers require an outside input that may be electrical, acoustic, or magnetic. One creative instance uses a piezoelectric disk to create bubbles to mix reagents in a channel [41]. Whichever method is chosen depends on the requirements of the experiment and the location of the device, be that in a lab setting or in remote regions. Our devices use a passive technique that employs a series of turns in the channel that cause violent shifts in the droplet that promotes mixing (**Figure 1.15).**

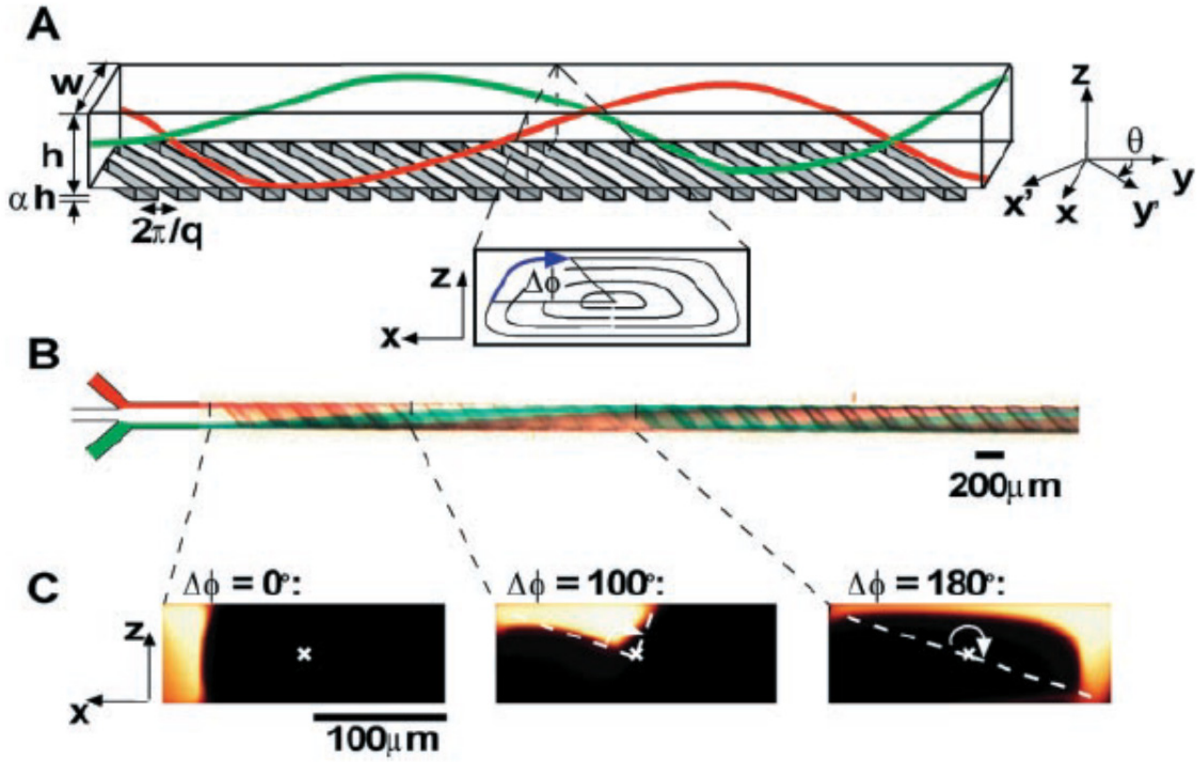

Figure 1.14 Mixing in channel through geometric designs. Ridges on the bottom of the channel create a vortex that combines the two phases together. From Stroock, A. D.; Dertinger, S. K. W.; Ajdari, A.; Mezić, I.; Stone, H. A.; Whitesides, G. M. *Science* **2002,** 295, 647-650. Reprinted with permission from AAAS.

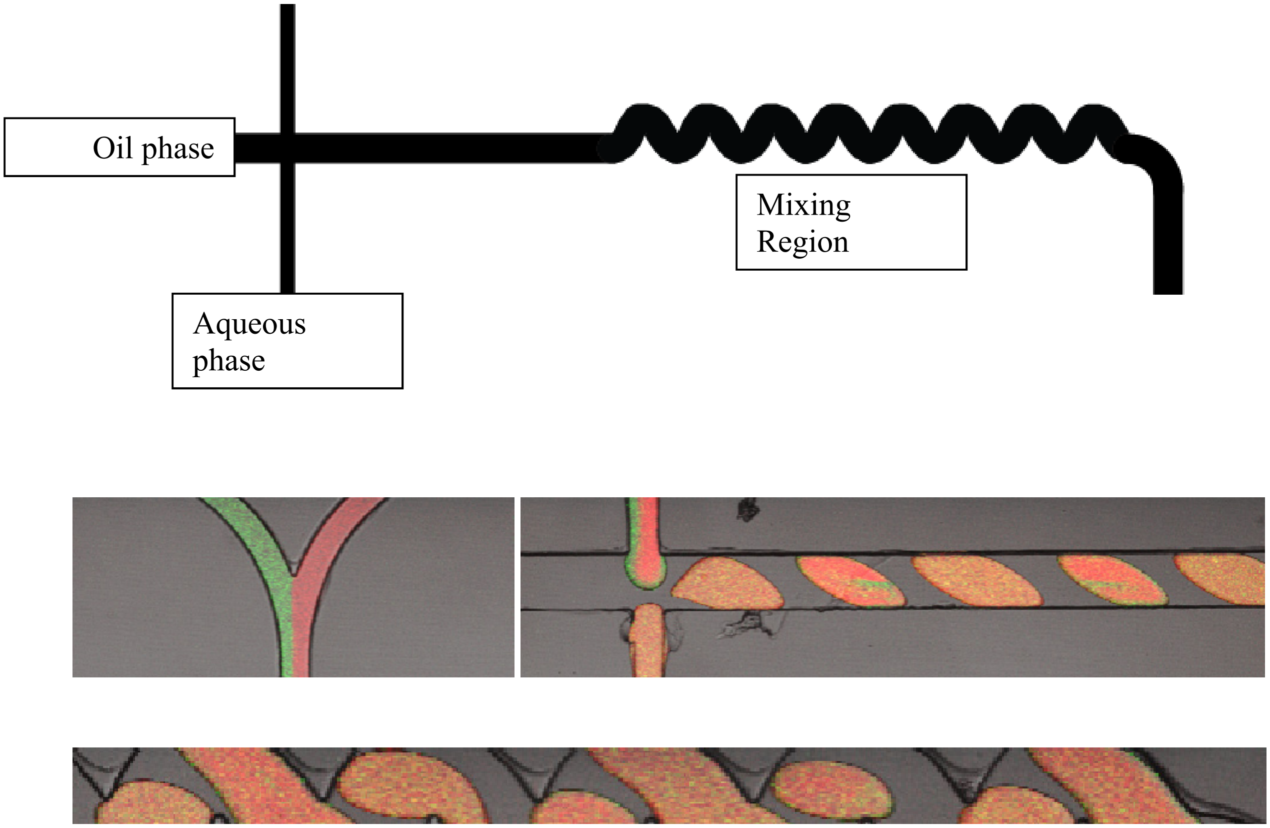

Figure 1.15 Droplet device showing a mixing region consisting of several sharp curves after droplet formation. Lower images show confocal fluorescence frames of laminar flow with co-flowing streams of fluorescein (green) and Cy5 (red) in the top left image. The top right image shows the lack of mixing in sample droplets from the top channel (red and green), while the bottom image shows more complete mixing through a 'folding' mechanism after passing through sharp channel turns.

1.3.4.2: Encapsulation, storage, and sorting

One advantage of microfluidic devices is their high throughput capabilities. It is possible to produce droplets at a frequency of 1 kHz or more relatively easy on some devices. In order to take advantage of this high number of individual reaction compartments, it must be possible to handle each one individually. Proteins, Cells, microbeads, etc. can be encapsulated on chip through various methods such as cell-triggered encapsulation, gel particle encapsulation, ordered encapsulation, or controlled encapsulation, as well as many other methods (**Figure 1.16)** [42-49]. These droplets are stable for extended periods because of the surfactants which make storage and incubation possible, allowing reactions to progress over necessary lengths of time [50, 51]. Once the required time frame has passed, it is often necessary to sort these droplets. Many techniques have been developed to do just this. Specific geometries have been developed to handle droplets mechanically. For instance, pillar arrays have been used to sort droplets based on size. Hydrodynamic effects can be employed, as droplets tend to focus themselves in certain regions of flow based on their size (**Figure 1.17).** Lasers play an important role in droplet sorting through fluorescence excitation of labeled droplets or for use as optical tweezers. Surface acoustic waves (SAWs) provide methods of sorting droplets label free while magnetic activated cell sorting (MACS) utilize magnetic nanoparticles in the droplet, which can be manipulated to control which direction the droplet goes [42]. MACS is not as efficient as other methods, however, with sorting rates around 20 droplets per second. Use of electric fields is also a common method of droplet sorting. Droplets can be electrostatically charged, allowing them to be manipulated by controlling downstream electric fields. Probably the most recognizable method is fluorescence-activated droplet sorting. Most of these techniques require a trigger mechanism through some sort of sensing device. Fluorescent labeling is a common practice as well as using electrodes in close proximity to detect some sort of signal. Mass spectrometry (MS) and Raman spectroscopy have also been applied as well as magnetic particles, as noted earlier [52-56].

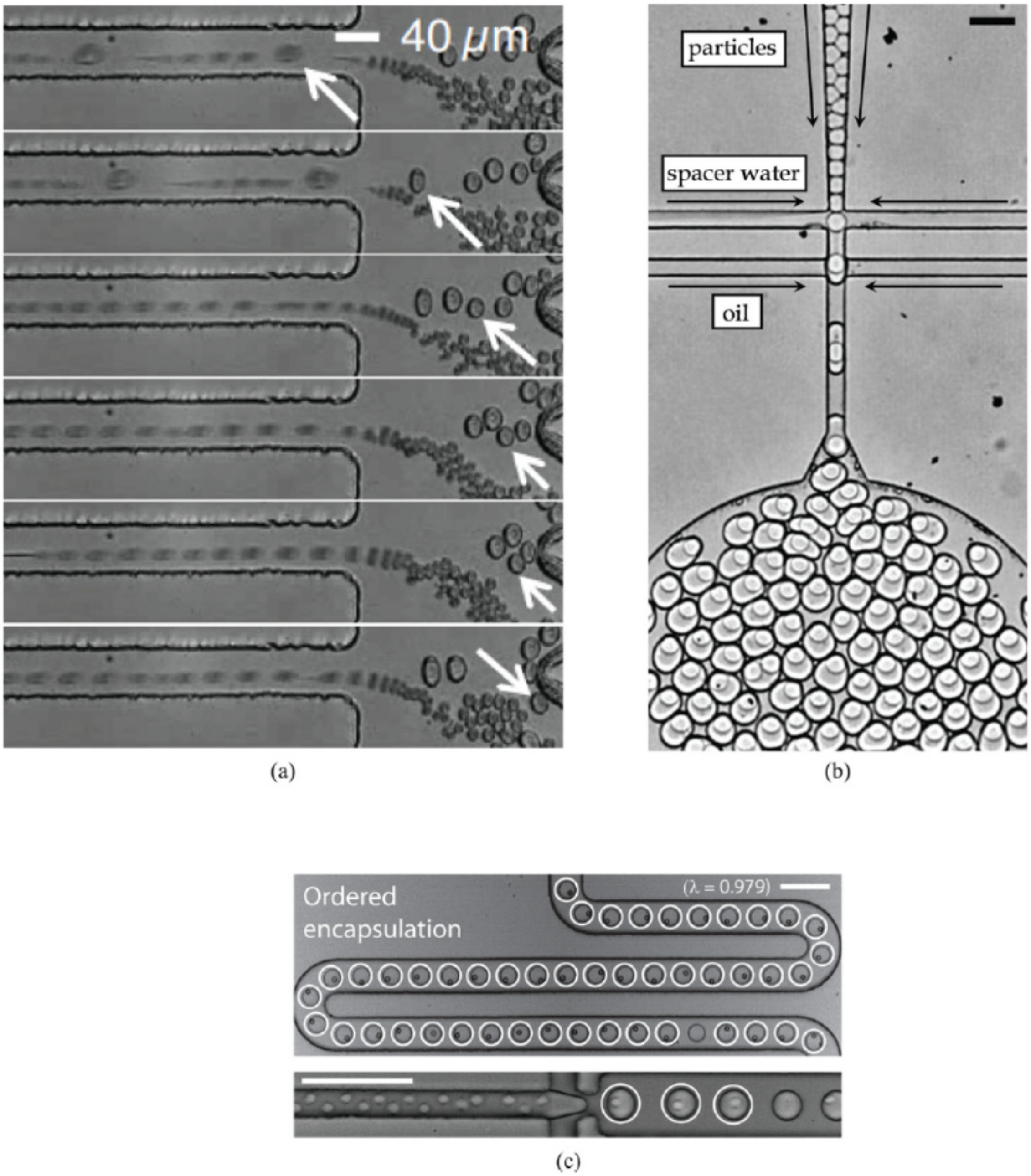

Figure 1.16 Various methods of encapsulation of materials on chip: a) Cell-triggered encapsulation Chabert, Max; Viovy, Jean-Louis *Proc. Natl. Acad. Sci USA* **2008,** 105, 9, 3191-3196. b) Gel-Particle encapsulation Adapted from Ref. 47 with permission from The Royal Society of Chemistry. c) Ordered encapsulation Adapted from Ref. 48 with permission from The Royal Society of Chemistry.

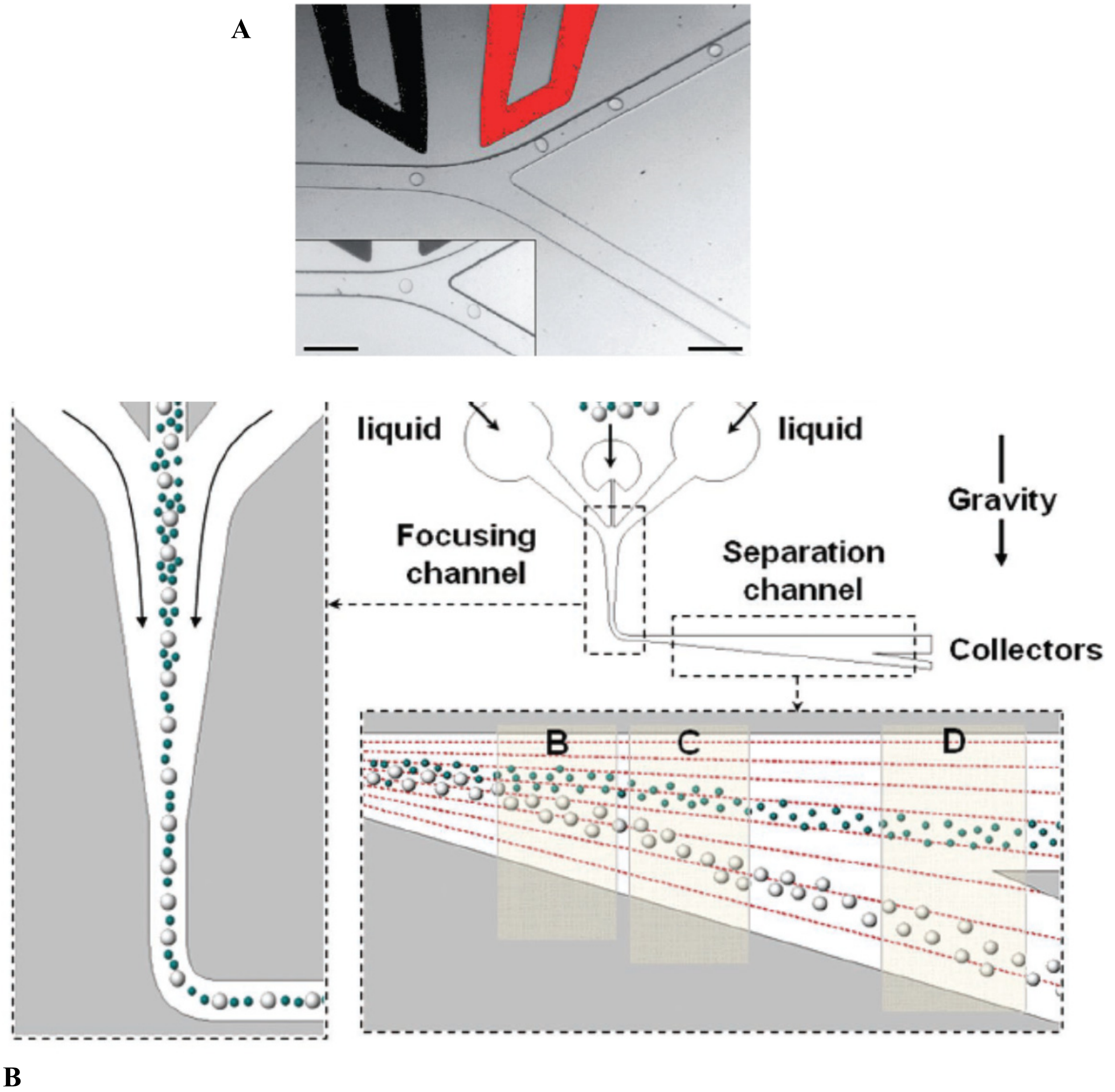

Figure 1.17 Various sorting methods A) Fluorescence activated droplet sorting. When a fluorescent signal is detected, an electric field is applied across the electrode, deflecting the droplet into a different channel. Adapted from Ref. 51 with permission from The Royal Society of Chemistry B) Mass dependent particle separation by gravity. Heavier droplets fall faster allowing them to flow into a separate channel. Adapted with permission from Huh, D.; Bahng, J. H.;Ling, Y.; Wei, H.; Kripfgans, O. D.; Fowlkes, J. B.; Grotberg, J. B.; Takayama, S. *Anal. Chem.* **2007,** 79, 1369-1376. Copyright 2007 American Chemical Society.

1.3.4.3: Applications

The applications of droplet microfluidics are wide-ranging. It would be a futile effort to list all applications, but there are a few techniques and areas of research that should be mentioned here. Use of droplet microfluidics for screening assays introduces novel advantages. Assays play a major role in screening large numbers of samples, but particularly for bioassays, the expense of reagents can become prohibitive. High throughput analysis at smaller volumes has been shown to greatly improve the effectiveness of these assays [57-60]. Droplet microfluidics has already been applied to various types of screening, single cell gene expression, as well as cell growth assays for biological and pharmaceutical screens [61-63]. Possibly the most important applications are to antibody screens as well as with directed evolution for enzymes and proteins. The method has also been used to detect mutations in rare cancer cells [64]. Research involving single molecule DNA, protein analysis, and nanoparticle synthesis use microfluidic systems because of the precise control of droplet size and volume and the high throughput capabilities [65-73]. Arrays for fluorescent detection schemes for use in methods such as digital polymerase chain reaction (PCR) are becoming popular, and capillary electrophoresis and mass spectrometry systems are becoming more predominant in the literature [74-79]. Lately, there has been a push for research involving digital microfluidics (DMF) which is a technique involving individual droplets that can be manipulated in various ways including moving, merging, and splitting [80]. And finally, applications for food and agriculture are appearing more frequently in the literature [81].

1.4: Lock-in Detection

1.4.1: Fundamentals of Lock-in Detection

As suggested, this research uses lock-in detection to assist in droplet analysis. Lock-in detection allows for the recovery of a signal in conditions of overwhelming noise or background, even when the ratio of signal to noise is unity or less. This is accomplished by modulation of a reference signal at the same frequency and phase as the sample. Since this reference is 'locked into' the sample, this is where the method gets its name. The method is capable of amplifying the signal of the sample without amplifying the noise or background. Most systems will use an optical chopper to switch the investigating beam between the sample and reference (**Figure 1.18).** Here, we are keeping the interrogating beam fixed and switching back and forth between the sample and reference through alternating sample/reference droplets in microfluidic channels. During development, our work progressed through various designs and fabrication techniques. First we utilized toner transfer masking (TTM) for device fabrication [82]. We then switched to more precise fabrication with photolithography, with which iterations lead through complex designs and ended on a rather simple solution. These designs and experiments are discussed in Chapter 2.5.

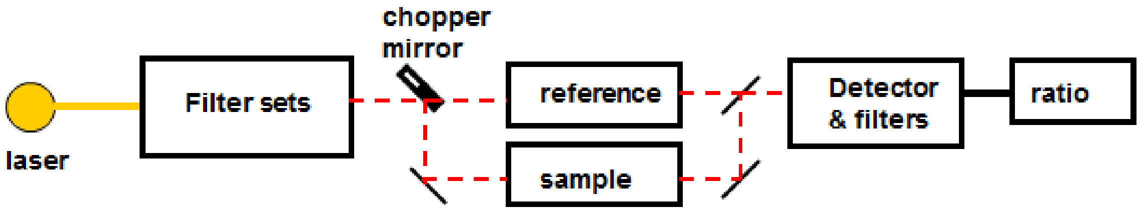

Figure 1.18 Block diagram for a typical lock-in detection system using a chopper mirror to switch the investigation beam between sample and reference.

1.4.2: Microfluidic sample chopper for lock-in detection

With droplet microfluidics segmenting the flow, the combination of microfluidics and a lock-in detection scheme can be useful. First, each drop serves as its own reaction vessel, mimicking the idea of sample and reference chambers for typical lock-in detection set-ups. Instead of alternating the beam used to investigate the sample and reference, our idea was that microfluidics could automatically alternate droplets containing sample and reference. First, this would result in a cheaper, easier-to-use reference system, with no need for complicated optical or electrical systems to control the light source. Second, the time scale of microfluidic droplet formation is extremely useful to provide high-throughput, multi-sample analysis. Some systems operate on the order of kHz droplet formation frequencies, which is much faster than a user of an optical lock-in setup can switch out samples and perform analysis. Third, a lockin setup is beneficial for microfluidics as well. Due to the size of the channels, some analytical methods such as absorbance are nearly impossible to perform, since the signal is too low and is overwhelmed by background noise. Lock-in detection allows the sample signal to be amplified while maintaining a constant signal for the background, greatly improving optical limits of detection of microfluidic systems.

1.5: Droplet based secretion sampling on microfluidic devices

As most processes in the human body are quite complex, research groups have continuously tried to find ways to simplify experimental approaches in order to obtain as much information as possible without being forced to use humans or animal models. As microfluidic devices began gaining notoriety in the late 1990's to early 2000's, they were being used to analyze cell contents through a variety of analytical methods such as capillary electrophoresis, analysis of proteins in conjunction with mass spectrometry, and analysis of deoxyribonucleic acid (DNA) [83-85]. Other groups began using microfluidics to monitor small molecules through these same analytical techniques by using the cells as sensors as early as 2002 [86-88]. A few years later, real time, quantitative analysis of the stimulated response of cells was being obtained. An application of this type of analysis was to murine islets of Langerhans from the pancreas which serves a major role in blood glucose levels. Islets of Langerhans secrete various types of hormones and are directly linked to diabetes, obesity, and other metabolic deficiencies that are predominant in society at a major cost to public health care [88]. When these islets are stimulated, an oscillatory response occurs as they secrete insulin to maintain blood glucose homeostasis. Earlier analyses of the secretion usually required tens to hundreds of islets as the techniques to monitor this process, such as enzyme-linked immunosorbent assay (ELISA), were not sensitive enough at small volumes [89]. Since microfluidics uses individual chambers in the form of droplets, it is capable of achieving much higher temporal resolution than is possible in bulk sampling systems. Combined with the greatly minimized dilution in microfluidic droplet generation, fewer islets would be required as these pulses would be secreted and compartmentalized in a small amount of time. This is beneficial because islet harvesting for research is a time consuming, tedious, and expensive process; additionally, new biological information is attainable with improved temporal resolution. In 2009, zinc secretion from islets was quantitatively measured by Dr. Easley and coworkers at almost an order of magnitude improvement in temporal resolution using a droplet-generating microfluidic device [90]. This work formed the basis of the droplet secretion sampling methods used in the Easley laboratory today. In 2011, our laboratory developed a passively operated system used to measure secretion from 8 individual murine islets in parallel, revealing pg/islet/min secretion levels at low temporal resolution (**Figure 1.19**) [91]. The next step for our laboratory was to use the droplet-based lock-in detection method for fluorescence sensing, combined with an islet secretion sampling chip and direct protein sensing technique to achieve stimulated islet secretion levels at high temporal resolution, all on one device. The analytical methodology to achieve this goal, i.e. the droplet generation and detection strategies, are outlined in this dissertation.

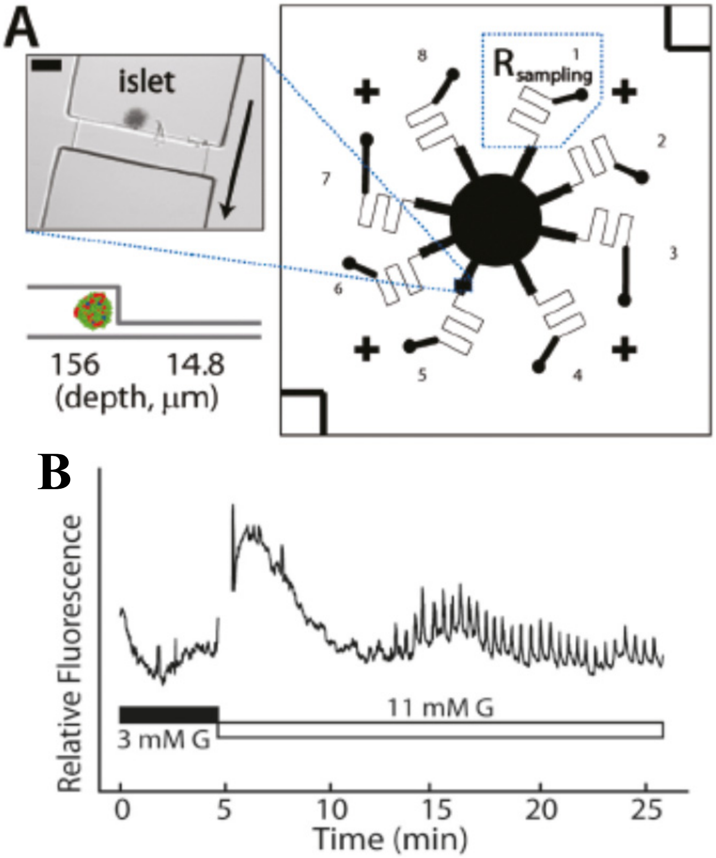

Figure 1.19 Passive microfluidic device allowing 8 islets to be stimulated and monitored in parallel. [87] Used with permission from Godwin, L. A.; Pilkerton, M. E.; Deal, K. S.; Wanders, D.; Judd, R. L.; Easley, C. J. *Anal. Chem.* **2011,** 83, 7166-7172. Copyright 2011. American Chemical Society.

References

1. Terry, S. C.; Jerman, J. H.; Angell, J. B. *IEEE Trans. Electron. Devices* ED-26, **1979,** 1880.
2. Nge, P. N.; Rogers, C. I.; Wooley, A. T. *Chem. Rev.* **2013,** 113, 2550-2583.
3. McDonald, J. C.; Duffy, D. C.; Anderson, J. R.; Chiu, D. T.; Wu, H.; Schueller, O. J. A.; Whitesides, G. M. *Electrophoresis* **2000,** 21, 27-40.
4. Kovarik, M. L.; Ornoff, D. M.; Melvin, A. T.; Dobes, N. C.; Wang, Y.; Dickinson, A. J.; Gach, C.; Shah, P. K.; Allbritton, N. L. *Anal. Chem.* **2013,** 85, 451-472.
5. Whitesides, G. M. *Nature.***2006,** 442, 368-373.
6. Thorsen, T.; Roberts, R. W.; Arnold, F. H.; Quake, S. R. *Phys. Rev. Lett.* **2001,** 86, 4163-4166.
7. Abate, A. R.; Weitz, D. A. *Biomicrofluidics* **2011,** 5, 014107.
8. Lorenz, H.; Despont, M.; Fhrni, N.; La Bianca, N.; Renaud, P.; Vettiger, P. *J. Micromech. Microeng.* **1997,** 7, 121-124.
9. Maheshwari, N.; Kottantharayil, A.; Kumar, M.; Mukherji, S. *Applied Surface Science* **2010,** 257, 451-457.
10. Lee, J. N.; Park, C.; Whitesides, G. M. *Anal. Chem.* **2003,** 75, 6544-6554.
11. Vickers, J. A.; Caulum, M. M.; Henry, C. S. *Anal. Chem.* **2006,** 78, 7446-7452.
12. Thompson, C. S.; Abate, A. R. *Lab Chip* **2013,** 13, 632-635.
13. Jo, B.; Van Lerberghe, L. M.; Motsegood, K. M.; Beebe, D. J. *J. Microelectromech. Syst.* **2000,** 9, 76-81.
14. Ouyang, Y.; Wang, S.; Li, J.; Riehl, P. S.; Begley, M.; Landers, J. P. *Lab Chip* **2013,** 13, 1762-1771.

15. Material Property Database http://www.mit.edu/~6.777/matprops/pdms.htm (accessed Sep 24, 2013)

16. Anna, S. L., *et al. Lab Chip,* **2009,** 9, 1102-1109.

17. Gupta, A.; Kumar, R. *Microfluid Nanofluid* **2010,** 8, 799-812.

18. Agresti, J. J.; Antipov, E.; Abate, A. R.; Ahn, K.; Rowatt, A. C.; Baret, J. C.; Marquez, M.; Klibanov, A. M.; Griffiths, A. D.; Weitz, D. A. *Proc. Natl. Acad. Sci USA,* **2010,** 107, 4004-4009.

19. Yoon, S.; Kim, J. A.; Lee, S. H.; Kim, M.; Park, T. H. *Lab Chip,* **2013,** 13, 1522-1528.

20. Fallah-Araghi, A.; Baret, J. C.; Ryckelynck, M.; Griffiths, A. *Lab Chip,* **2012,** 12, 882-891.

21. Berg, J. C. (2010) *An Introduction to Interfaces and Colloids: The Bridge to Nanoscience,* Co., Singapore: World Scientific Publishing

22. Holtze, C.; Rowat, A. C.; Agresti, J. J.; Hutchison, J. B.; Angilé, F. E.; Schmitz, C. H. J.; Köster, S.; Duan, H.; Humphry, K. J.; Scanga, R. A.; Johnson, J.S.; Pisignano, D.; Weitz, D. A. *Lab Chip* **2008,** 8, 1632-1639.

23. Baret, J. C. *Lab Chip* **2012,** 12, 422-433.

24. Baret, J. C.; Kleinschmidt, F.; El Harrak, A.; Griffiths, A. D. *Langmuir* **2009,** 25, 6088-6093.

25. DeJournette, C. J.; Kim, J.; Medlen, H.; Li. X.; Vincent, L. J.; Easley, C. J. *Anal. Chem.* **2013,** DOI: 10.1021/ac4026048.

26. Zhu, Z.; Jenkins, G.; Zhang, W.; Zhang, M.; Guan, Z.; Yang,C.J. *Anal. Bioanal. Chem.* **2012,** 403, 2127-2143.

27. Tran, T. M.; Thompson, C. S.; Abate, A. R. *J. Phys. D: Appl. Phys.* **2013,** 46, 114004.

28. Tan, Y.C.; Fisher, J. S.; Lee, A. I.; Cristini, V.; Lee, A. P. *Lab Chip* **2004,** 4, 292-298.

29. Garstecki, P.; Fuerstman, M. J.; Stone, H. A.; Whitesides, G. M. *Lab Chip* **2006,** 6, 437-446.

30. Abate, A. R.; Poitzsch, A.; Hwang, Y.; Lee, J.; Czerwinska, J.; Weitz, D. A. *Phys. Rev. E* **2009,** 80, 026310.

31. Takeuchi, S.; Garstecki, P.; Weibel, D. B.; Whitesides, G. M. *Adv. Mater.* **2005,** 17, 1067-1072.

32. Nie, Z.; Seo, M.; Xu, S.; Lewis, P. C.; Mok, M.; Kumacheva, E.; Whitesides, G. M.; Garstecki, P.; Stone, H. *Microfluid Nanofluid* **2008,** 5, 585-594.

33. Anna, S. L; Bontoux, N.; Stone, H. A.; *Appl. Phys. Lett.* **2003,** 82, 364-366.

34. Utada, A. S.; Fernandez-Nieves, A.; Stone, H. A.; Weitz, D. A. *Phys. Rev. Lett.* **2007,** 99, 094502.

35. Utada, A. S.; Fernandez-Nieves, A.; Gordillo, J. M.; Weitz, D. A. *Phys. Rev. Lett.* **2008,** 100, 014502.

36. Song, H.; Tice, J. D.; Ismagilov, R. F. *Angew. Chem. Int. Ed.* **2003,** 42, 767-772.

37. Li. Y.; Xu, Y.; Feng, X.; Liu, B. *Anal. Chem.* **2012,** 84, 9025-9032.

38. Casadevall I Solvas, X.; Srisa-Art, M.; deMelllo, A. J.; Edel, J. B. *Anal. Chem.* **2010,** 82, 3950-3956.

39. Stroock, A. D.; Dertinger, S. K. W.; Ajdari, A.; Mezić, I.; Stone, H. A.; Whitesides, G. M. *Science* **2002,** 295, 647-650.

40. Kane, A. S.; Hoffmann, A.; Baumgärtel, P.; Seckler, R.; Reichardt, G.; Horsley, D. A.; Schuler, B.; Bakajin, O. *Anal. Chem.* **2008,** 80, 9534-9541.

41. Wang, S.; Huang, X.; Yang, C. *Lab Chip* **2011,** 11, 2081-2087.

42. Lagus, T. P.; Edd, J. F. *J. Phys. D: Appl. Phys.* **2013,** 46, 114005.

43. Chen, A.; Byvank, T.; Chang, W.; Bharde, A.; Vieira, G.; Miller, B.; Chalmers, J. J.; Bashir, R.; Sooryakumar, R. *Lab Chip* **2013,** 13, 1172-1181.

44. Tan, Y.; Ho, Y. L.; Lee, A. P. *Microfluid Nanofluid* **2008,** 4, 343-348.

45. Clausell-Tormos, J.; Lieber, D.; Baret, J. C.; El-Harrak, A.; Miller, O. J.; Frenz, L.; Blouwolff, J.; Humphry, K. J.; Köster, S.; Duan, H.; Holtze, C.; Weitz, D. A.; Griffiths, A. D.; Merten, C. A. *Chemistry & Biology* **2008,** 15, 427-437.

46. Chabert, Max; Viovy, Jean-Louis *Proc. Natl. Acad. Sci USA* **2008,** 105, 9, 3191-3196.

47. Abate, A. R.; Chen, C. H.; Agresti, J. J.; Weitz, D. A. *Lab Chip* **2009,** 9, 2628-2631.

48. Edd, J. F.; Carlo, D. D.; Humphry, K. J.; Köster, S.; Irimia, D.; Weitz, D. A.; Toner, M. *Lab Chip* **2008,** 8, 1262-1264.

49. Lagus, T.P.; Edd, J.F. *J. Visualized Exp.* **2012,** 64, 4096.

50. Edgar, J. S.; Milne, G.; Zhao, Y.; Pabbati, C. P.; Lim, D. S. W.; Chiu, D. T. *Angew. Chem. Int. Ed.* **2009,** 48, 2719-2722.

51. Boukellal, H.; Selimović, Š.; Jia, Y.; Cristobal, G.; Fraden S. *Lab. Chip* **2009,** 9, 331-338.

52. Bernate, J. A.; Liu, C.; Lagae, L.; Konstantopoulos, K.; Drazer, G. *Lab Chip* **2013,** 13, 1086-1092.

53. Huh, D.; Bahng, J. H.;Ling, Y.; Wei, H.; Kripfgans, O. D.; Fowlkes, J. B.; Grotberg, J. B.; Takayama, S. *Anal. Chem.* **2007,** 79, 1369-1376.

54. Christopher, G. F.; Bergstein, J.; End, N. B.; Poon, M.; Nguyen, C.; Anna, S. L. *Lab Chip* **2009,** 9, 1102-1109.

55. Tan, Y.; Ho, Y. L.; Lee, A. P. *Microfluid Nanofluid* **2008,** 4, 343-348.

56. Baret, J. C.; Miller, O. J.; Taly, V.; Ryckelynck, M.; El-Harrak, A.; Frenz, L.; Rick, C.; Samuels, M. L.; Hutchison, J. B.; Agresti, J.J.; Link, D. R.; Weitz, D. A.; Griffiths, A. D. *Lab Chip* **2009,** 9, 1850-1858.

57. Wang, W.; Yang, C.; Li, C. M. *Lab Chip* **2009,** 9, 1504-1506.

58. Huebner, A.; Bratton, D.; Whyte, G.; Yang, M.; deMello, A. J.; Abell, C.; Hollfelder, F. *Lab Chip* **2009,** 9, 692-698.

59. Mary, P.; Chen, A.; Chen, I.; Abate, A. R.; Weitz, D. A. *Lab Chip* **2011,** 11, 2066-2070.

60. Guo, M. T.; Rotem, A.; Heyman, J. A.; Weitz, D. A. *Lab Chip* **2012,** 12, 2146-2155.

61. Karns, K.; Vogan, J. M.; Qin, Q.; Hickey, S. F.; Wilson, S. C.; Hammond, M. C.; Herr, A. E. *J. Am. Chem. Soc.* **2013,** 135, 3136-3143.

62. Brouzes, E.; Medkova M.; Savenelli, N.; Marran, D.; Twardowski, M.; Hutchison, J. B.; Rothberg. J. M.; Link, D. R.; Perrimon, N.; Samuels, M. L. *Proc. Natl. Acad. Sci. U.S.A.* **2009,** 106, 14195-14200.

63. Theberge, A. B.; Mayot, E.; El Harrak, A.; Kleinschmidt, F.; Huck, W. T. S.; Griffiths, A. D. *Lab Chip* **2012,** 12, 1320-1326.

64. Pekin, D.; Skhiri, Y.; Baret, J. C.; Corre, D. L.; Mazutis, L.; Salem, C. B.; Millot, F.; Harrak, A. E.; Hutchison, B.; Larson, J. W.; Link, D. R.; Laurent-Puig, P.; Griffiths, A. D.; Taly, V. *Lab. Chip* **2011,** 11, 2156-2166.

65. Piepenburg, O.; Williams, C. H.; Stemple, D. L.; Armes, N. A. *PLoS Biol.* **2006,** 4, doi: 10.1371/journal.pbio.0040204.

66. Kumaresan, P.; Yang, C. J.; Cronier, S. A.; Blazej. R. G.; Mathies, R. A. *Anal. Chem.* **2008,** 80, 3522-3529.

67. Srisa-Art, M.; deMello, A. J.; Edel, J. B. *Anal. Chem.* **2007,** 79, 6682-6689.

68. Meier, M.; Sit, R.; Pan, W.; Quake, S. R. *Anal. Chem.* **2012,** 84, 9572-9578.

69. Apori, A. A.; Brozynski, M. N.; El-Sayed, I. H.; Herr, A. E. *J. Proteome Res.* **2013,** 12, 1254-1265.

70. Tia, S. Q.; Brown, K.; Chen, D.; Herr, A. E. *Anal. Chem.* **2013,** 85, 2882-2890.

71. Fredriksson, S.; Gullberg, M.; Jarvius, J.; Olsson, C.; Pietras, K.; Gústafsdóttir, S. M.; Östman, A.; Landegren, U. *Nature Biotechnology* **2002,** 20, 473-477.

72. Horrocks, M. H.; Li, J.; Shim, J.; Ransinghe, R. T.; Clarke, R. W.; Huck, W. T. S.; Abell, C.; Klenerman, D. *Anal. Chem.***2012,** 84, 179-185.

73. Mazutis, L.; Araghi, A. F.; Miller, O. J.; Baret, J. C.; Frenz, L.; Janoshazi, A.; Taly, V.; Miller, B. J.; Hutchison, J. B.; Link, D.; Griffiths, A. D.; Ryckelynck, M. *Anal. Chem.* **2009,** 81, 4813-4821.

74. Hatch, A. C.; Fisher, J. S.; Tovar, A. R.; Hsieh, A. T.; Lin, R.; Pentoney, S. L.; Yang, D. L.; Lee, A. P. *Lap Chip* **2011,** 11, 3838-3845.

75. Lim, J.; Gruner, P.; Konrad, M.; Baret, J.C. *Lab Chip*

76. Mellors, J. S.; Black, W. A.; Chambers, A. G.; Starkey, J. A.; Lacher, N. A.; Ramsey, J. M. *Anal. Chem.* **2013,**

77. Shih, S. C. C.; Yang, H.; Jebrail, M. J.; Fobel, R.; McIntosh, N.; Al-Dirbashi, O. Y.; Chakraborty, P.; Wheeler, A. R. *Anal. Chem.* **2012,** 84, 3731-3738.

78. Paegel, B. M.; Hutt, L. D.; Simpson, P. C.; Mathies, R. A. *Anal. Chem.* **2000,** 77, 3030-3037.

79. Croushore, C. A.; Supharoek, S.; Lee, C. Y.; Jakmunee, J.; Sweedler, J. V. *Anal. Chem.* **2012,** 84, 9446-9452.

80. Shih, S. C. C.; Barbulovic-Nad, I.; yang, X.; Fobel, R.; Wheeler, A. R. *Biosensors and Bioelectronics* **2013,** 314-320.

81. Neethirajan, S.; Kobayashi, I.; Nakajima, M.; Wu, D.; Nandagopal, S.; Lin, F. *Lab Chip* **2011,** 11, 1574-1586.

82. Easley, C. J.; Benninger, R. K. P.; Shaver, J. H.; Head, W. S.; Piston, D. W. *Lab Chip* **2009,** 9, 1119-1127.

83. Kameoka, J.; Craighead, H. G.; Zhang, H. W.; Henion, J. *Anal. Chem.* **2001,** 73, 1935-1941.

84. Figeys, D.; Gygi, S. P.; McKinnon, G.; Aebersold, R. *Anal. Chem.* **1998,** 70, 3728-3734.

85. Koutny, L. Schmalzing, D.; Salas-Solano, O.; El-Difrawy, S.; Adourian, A.; Buounocore, S.; Abbey, K.; McEwan, P.; Matsudaira, P.; Ehrlich, D. *Anal. Chem.* **2000,** 72, 3388-3391.

86. Yang, M. S.; Li, C. W.; Yang, J. *Anal. Chem.* **2002,** 74, 3991-4001.

87. Heo, J.; Thomas, K. J.; Seong, G. H.; Crooks, R. M.; *Anal. Chem.* **2003,** 75, 22-26.

88. Roper, M. G.; Shackman, J. G.; Dahlgren, G. M.; Kennedy, R. T. *Anal. Chem.* **2003,** 75, 4711-4717.

89. Dishinger, J. F.; Reid, K. R.; Kennedy, R. T. *Anal. Chem.* **2009,** 81, 3119-3127.

90. Easley, C. J.; Rocheleau, J. V.; Head, W. S.; Piston, D. W. *Anal. Chem.* **2009,** 81, 9086-9095.

91. Godwin, L. A.; Pilkerton, M. E.; Deal, K. S.; Wanders, D.; Judd, R. L.; Easley, C. J. *Anal. Chem.* **2011,** 83, 7166-7172.

Chapter 2: Concepts in Design and Fabrication of Microfluidic Devices

This chapter outlines the variety of microfluidic channel design and fabrication techniques used throughout my dissertation work. Although some of the approaches were not ultimately adopted, the pilot studies shown within the chapter have likely opened new avenues worthy of exploration by others in the future.

2.1: Toner transfer masking

2.1.1: Principles

In our first attempts in developing a signal/reference microfluidic chip, we utilized a technique called toner transfer masking (TTM). This process is a rapid prototyping technique that allows a pattern to be designed, a mask to be printed, a master to be made, and a chip to be produced within only a few hours. It is also inexpensive and simple to perform, and it is a great way to introduce students to microfluidics. With this rapid prototyping, if a design fails, it is possible to make adjustments and try again within a few hours, even the same day. The technique uses printer ink that is thermally transferred to a brass master that can be etched using an ammonium persulfate solution [$(NH_4)_2S_2O_8$]. The user simply molds PDMS chips from that master. [1]

2.1.2: Early signal/reference device

Our goal was to produce devices capable of alternating production of signal and reference droplets without active control, i.e. devices that would promote passive switching between the two streams. The first design included one oil and two aqueous channels that came together through a branched rectangular channel network with a curved entrance to the outlet (**Figure 2.1).** The hypothesis was that droplets generated from one aqueous inlet would impede flow and promote droplet generation by the other inlet, followed by alternating generation via the same mechanism. Typically, however, one aqueous channel would form droplets better than the other, which varied among chips. These inconsistencies made it difficult to perform any real comparisons between each droplet. It is believed that variability in the channel wall structure from the etching process made one of the two channels more favorable for fluid flow (lower resistance). The brass master etching process in TTM is highly dependent on surface contact and design of the channels. The design also may have led to problems with formation. By having the 2 aqueous inputs partially shielded from each other, significant variation in fluid flow may occur around the rectangular pattern, and the intended fluidic coupling between the droplet generators may have been dampened. Also, we began to have problems with the thermal transfer process in TTM. We discovered that the composition of the paper used as the transfer material was changed by the company, rendering it nearly useless for the technique. Since this is a major step in the TTM process, it became difficult to fabricate devices. At this point, it was decided that changing to the more standard SU-8 based photolithography would be the best route. As described in Chapter 3, the much more precise SU-8 based masters allowed us to achieve our goal.

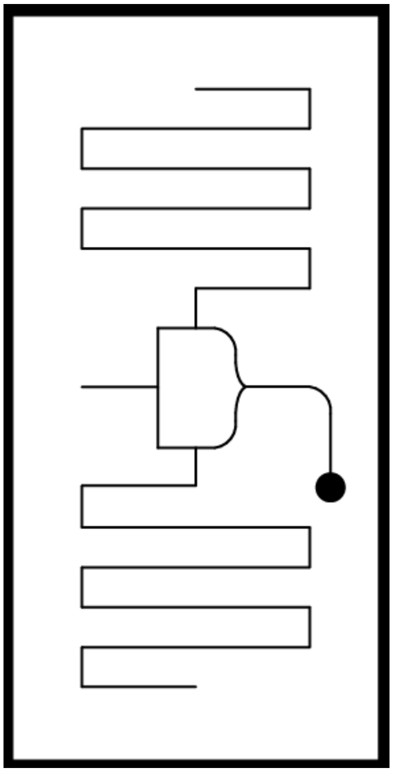

Figure 2.1 Original design for the microfluidic sample/reference chip.

2.2: Fluidic Capacitance

There are several comparisons that can be made between microfluidic components and electrical circuit components. A few examples are the flow of fluid compared to the flow of electrons, storing of fluid to be released later as in an electrical capacitor, or preventing flow through the use of structures similar to diodes in channels, which allow flow in one direction [2,3]. Our goal was to leverage prior work on fluidic capacitance and design microfluidic chips that would allow solutions to be stored in channels and released whenever needed, and as a means of buffering pulses in channels resulting from the use of valves and pumps to control fluid flow [3].

2.2.1: Monolithic and multilayer fluidic capacitors

A disadvantage of previously designed fluidic capacitors is that they require multilayer soft lithography, increasing device fabrication times by 2- or 3-fold [3]. We set out to design an SU-8 master that would allow a single PDMS molding step, yet still include fluidic capacitors with relatively high capacity. Several chips were designed with the same basic concept in mind, but with varying thicknesses of PDMS membranes between channels. As shown by the example chip in **Figure 2.2**, each chip included a straight channel surrounded by two rectangular regions on each side of the channel. These regions are approximately 3 times deeper than the channel and are intended to contain only air. The gap between the channel and voided regions defined the PDMS membrane thickness (10 to 50 μm), which was varied as along with the length of the voided regions (5 to 25 mm) (**Figure 2.2).** The ends of the channel were punched out in order to have a reservoir for an outlet and an inlet to allow pressure to be applied. During each experiment, the channel and void regions were monitored by light microscopy to measure the amount of deflection, or storage, allowed by each set of variables, e.g. gap size and length

(**Figure 2.3).** Various pressures were applied to the channel making the channel walls bulge, which was detectable by microscopy. This deflection can provide a direct analogy to the available 'fluidic capacitance' of each chip (**Figure 2.4).** Unfortunately, it was discovered that the capacitance of this design was fundamentally hindered by the fact that the walls of the void were bound to the glass substrate and were still relatively shallow. This problem prevented the PDMS membranes from moving significantly, therefore preventing the channel wall from being able to expand and limiting the fluidic capacitance. As shown by the nonlinear least squares fitting of the data in **Figure 2.4**, the maximum fluidic capacitance measured was $4.63 \pm 0.74 \times 10^{-5}$ mm^3 kPa^{-1} leading to an RC value of 3.64 ± 0.57 seconds which was far larger than needed for functional devices.

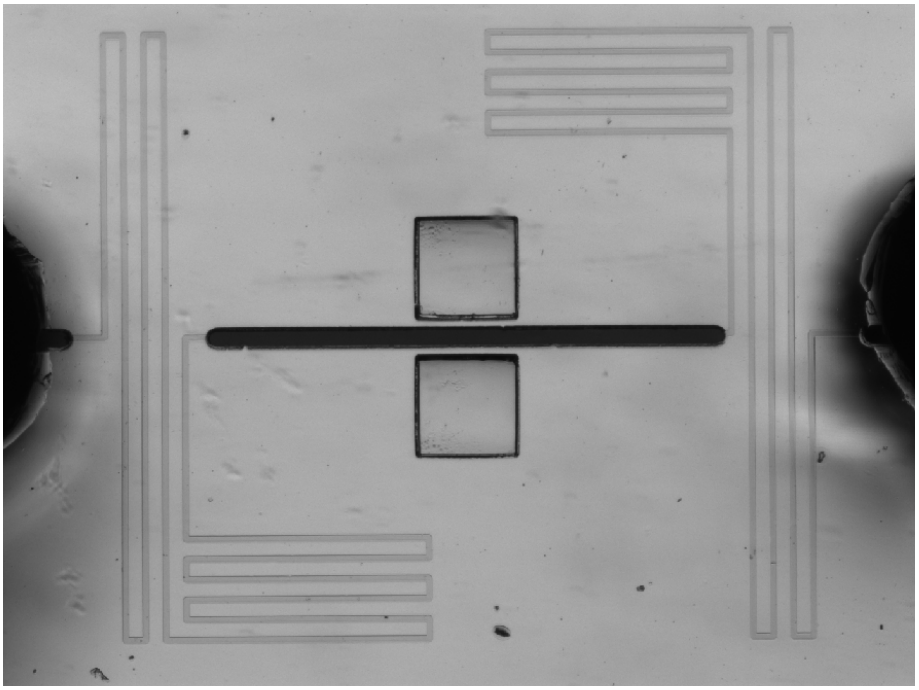

Figure 2.2 Monolithic fabrication of fluidic capacitors. This device was made with a single cured layer of PDMS. Central channel and void regions were fabricated deeper to give maximal capacity.

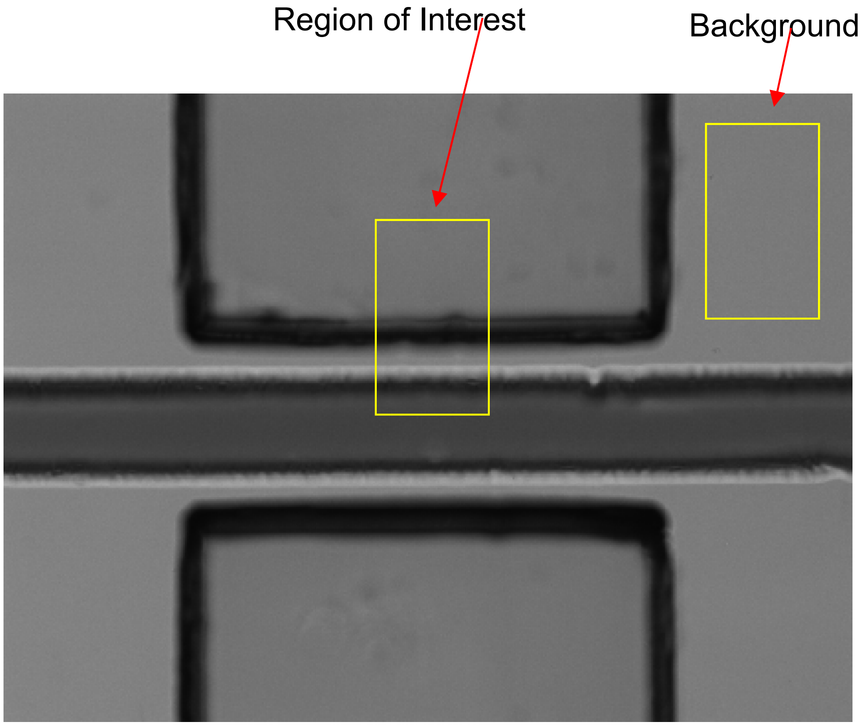

Figure 2.3 Zoomed in view of microscope image of single-layer fluidic capacitor, showing the area used for data analysis with as well as region used for background correction.

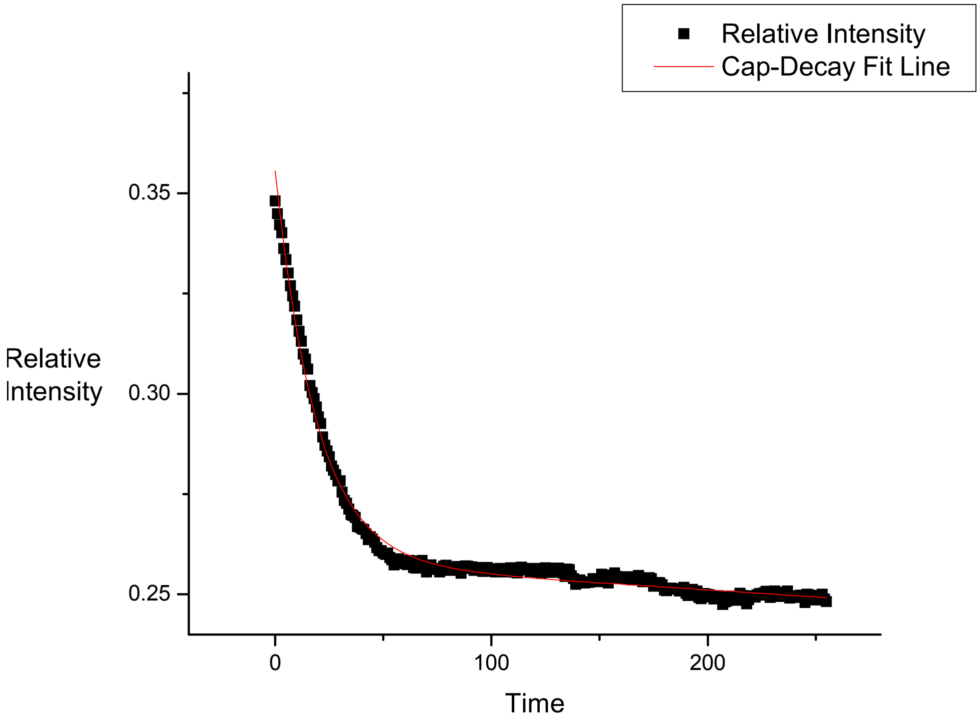

Figure 2.4 Plot of intensity obtained from region of interest on capacitance chip as pressure is applied to channel. Nonlinear least squares fitting of a single exponential decay is shown in red.

Because of this geometric hindrance, it was decided that a change in design should be implemented. Instead of the channel walls moving laterally, the ceiling of the channel should be allowed to move, as in previous work [3] Although this design requires multilayer fabrication of PDMS devices, a much wider range of fluidic capacitances should be accessible. We set out to provide the first characterization of fluidic capacitance versus PDMS ceiling thickness. The thinner the PDMS ceiling is, the more deflection will be allowed. Additionally, another factor could be exploited to modulate the capacitance of the system. Normally, PDMS is made in a 10:1 ratio of elastomer to curing agent. This ratio can be changed, for example to 5:1, 15:1, or 20:1, while maintaining much of the substrate integrity. The higher the percentage of elastomer, the more flexible the material becomes, allowing it to deflect more under pressure. To give a wide range of capacitances, a simple test device was made with multiple holes punched through it (**Figure 2.5).** Various ratios of PDMS were mixed, degassed, then spin coated onto a silicon wafer. They were allowed to partially cure, and then a hole-punched slab of thick PDMS was placed on top of this thin layer. Through this partial curing process, the two layers bonded creating reservoirs with thin membranes on the bottom. A tube was inserted into the top of the holes and connected to a syringe. On the bottom side of the thin membrane, a mark was made with a permanent marker, and the device was placed onto the microscope. The objective was focused onto this mark, and the z-position of the focus was recorded to monitor membrane deflection. Controlled pressures were applied to the reservoir, and the membrane deflection was monitored in this way. This procedure was carried out 5 times for each membrane and repeated on all mixing ratios. The deflection distance is plotted vs. thickness of the membrane for all PDMS ratios made (**Figure 2.6).** As expected, membrane deflection at constant pressure was inversely related to its thickness at all mixing ratios. However, the trends with mixing ratio were difficult to interpret. As such, further work is needed to fully characterize this system.

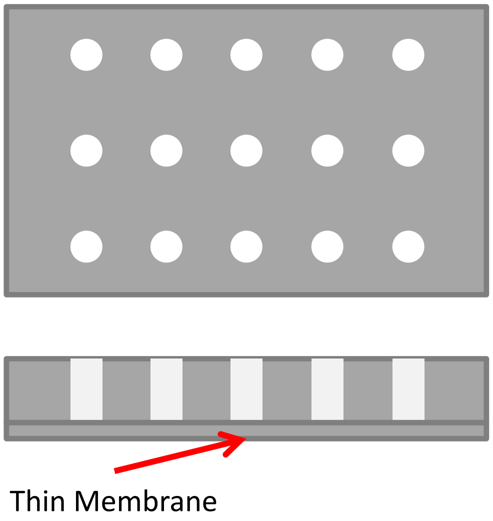

Figure 2.5 This chip design was used to test the flexibility of various cure ratios of PDMS.

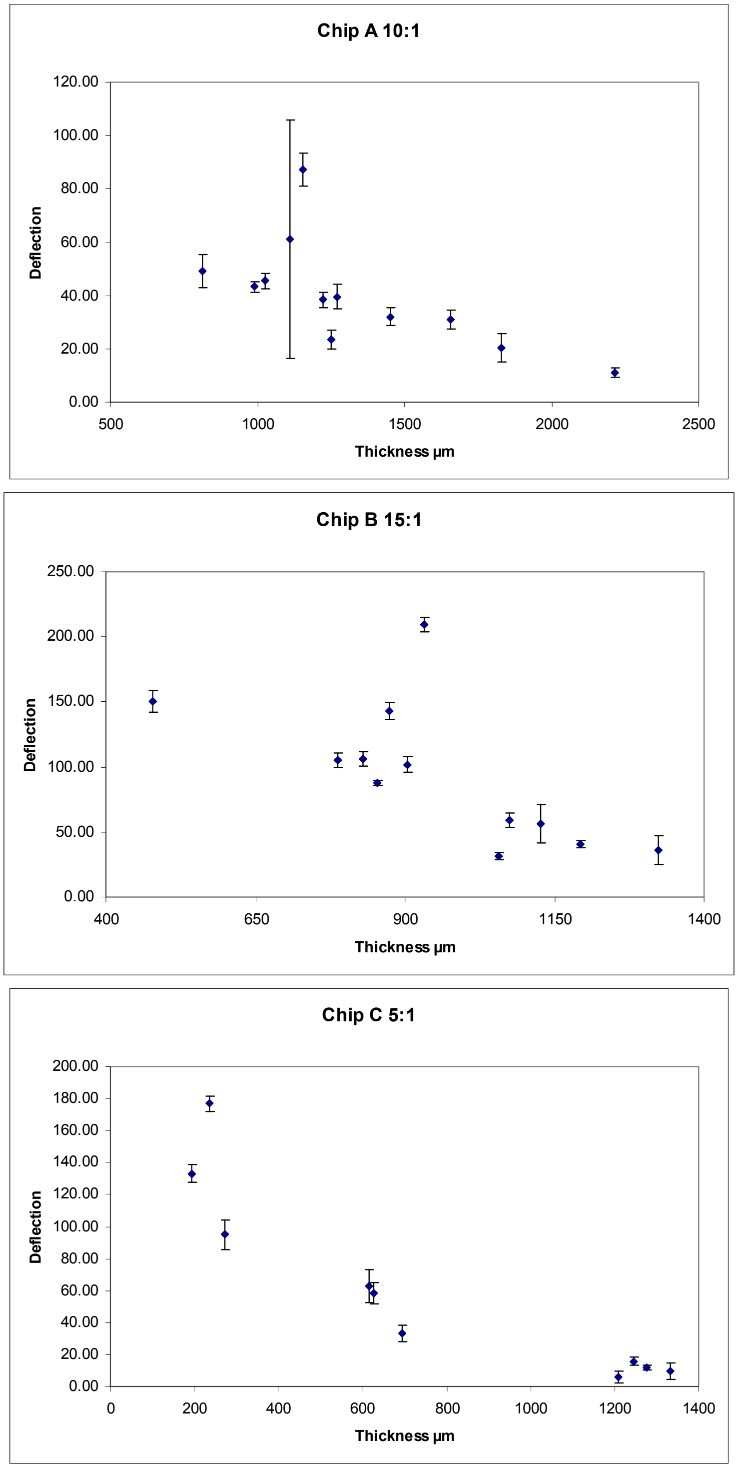

Figure 2.6 Plot of deflection vs. membrane thickness of PDMS for various mixture ratios.

2.2.2: Electrical capacitance measurement for droplet detection

One of the major goals in the Easley laboratory is to establish a feedback control system for droplet formation. Before arriving at our final design, several approaches were explored for droplet detection. The idea of using the electrical capacitance of the liquids was thought to have potential, since the dielectric constant of oil and water are so different, at 80.1 and 5.3 respectively. It seemed as though it would be possible to identify which droplet was aqueous and which was oil as it passed by a capacitive detector. The detector would need to be a conductive material that is placed in the channel or in close proximity on each side of the droplet channel. A solder was purchased from IndiAlloy, composed of 52 % indium and 48 % tin, one that was easy to work with and has a high conductivity. The chip used consisted of several channels running parallel with each other and separated by 20 μm, but only three of the channels were used (**Figure 2.7**). The middle channel contained the water in oil droplets, while the two neighboring channels contained Indialloy that was injected above its melting temperature via syringe. Wires were connected to the solder and then connected to a capacitance to digital converter (Analog Devices) interfaced to a computer. Unfortunately, the change in electrical capacitance between water and oil was very near the limit of detection of this system.

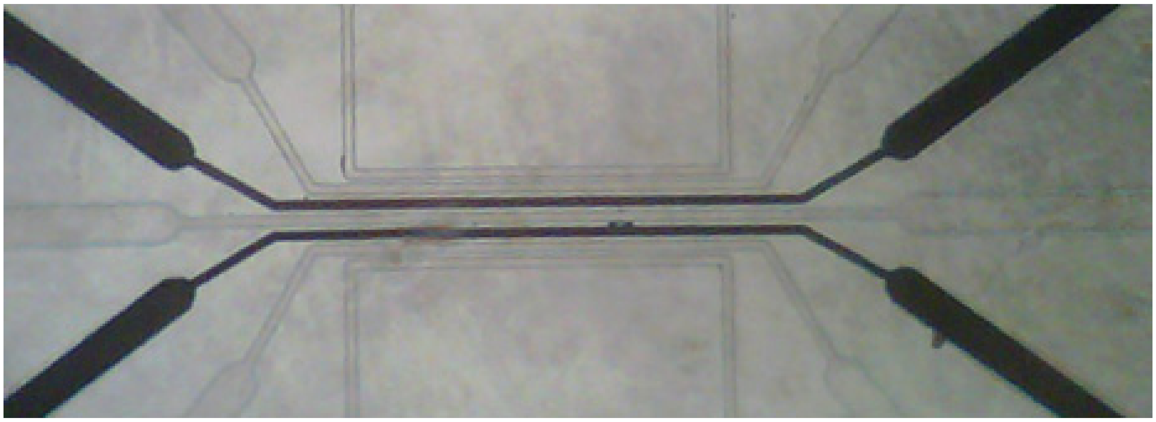

Figure 2.7 Multichannel device used in attempts to use electrical capacitance for droplet detection. Two channels are filled with IndiAlloy (dark), while the middle channel contained water or oil.

Through collaboration with Prof. Robert Dean (Auburn University, Electrical and Computer Engineering), we determined several variables that should be improved. First, was the detection region was made to be a similar size as the droplets to eliminate interferences between successive droplets. Secondly, it was thought that a sandwich effect would work well for detection with electrodes above and below the channel with droplets running through. A thin layer of PDMS was spin coated onto a wafer with channel designs. Solder was placed into two separate pieces of PDMS. These pieces were then bound above and below the droplet channel (**Figure 2.8**).

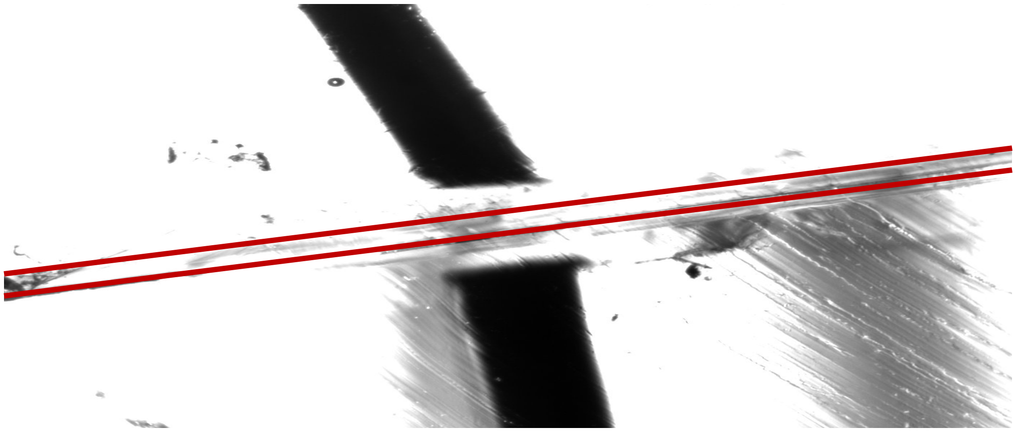

Figure 2.8 Droplet channel is shown (outlined in red) sandwiched between two fabricated solder electrodes. No capacitive signal was detected, likely because the gap between electrodes and channel was over 200 μm.

Each phase, oil and water, were passed through the channel as well as aqueous droplets in the oil phase. After multiple attempts, no detectable signal was observed, likely due to the gap size between electrodes and channels.

After further discussions with our collaborator, a new design was created that included prealigned electrode channels and a completely duplicate system for constant referencing (**Figure 2.9).** These devices have yet to be fabricated, since we chose to move to the more sensitive optical techniques discussed later. However, simple calculations by our collaborators indicate that the design has promise for future work.

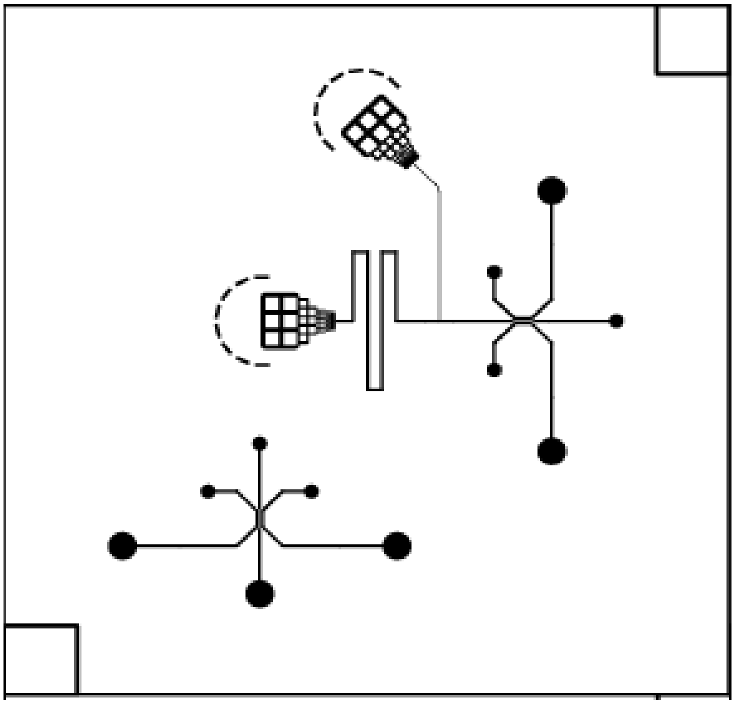

Figure 2.9 New design for droplet detection via electrical capacitance, with reference system included (lower left channels).

2.3: Fluidic Diodes

2.3.1: Photocurable PDMS

Continuing with the analogies of electrical components to microfluidic flow control components, it has been shown possible to make diodes in channels that will only allow flow of various materials in one direction [2, 4-6], preventing backflow as in a macroscale one-way valve. Based on the similarity to electrical diodes, we chose fluidic diode structures developed by the Takayama group in 2010 [6]. These are made in 3 layers: the top layer being two channels that are not connected, the middle layer being a via, and a bottom layer consisting of a void region for the middle layer to deflect and open to allow fluid to pass through. Originally, to fabricate vias, we used a product called photo curable PDMS (PC-PDMS), which uses UV light to cure it instead of heat. We spin coated PC-PDMS onto a silicon wafer, then used a photomask and UV light to generate cured PDMS with small vias (through-holes). Our first attempts failed, because once the PC-PDMS was cured, it would not release from the wafer without ripping or ruining the design. Next, we tried applying a releasing agent, chlorotrimethylsilane, which was vapor coated onto the wafer in order to facilitate thin membranes being removed easily. Unfortunately, this product interfered with the development steps of PC-PDMS by creating a viscous, slimy material on the wafer, destroying the membrane. After several attempts, PC-PDMS was abandoned due to these fabrication problems, in addition to the high cost and short shelf life of the product. The shelf life of PC-PDMS was only one month at a cost of $1 000 per bottle, thus it was decided to search for another method of producing vias.

2.3.2: Thin membranes using PDMS

2.3.2.1: Spin coating and via formation

Chlorotrimethylsilane was deposited onto silicon wafers as described earlier, then PDMS was spin coated over and allowed to partially cure. A small punch, 350 µm in size, was then used to punch vias through the PDMS on the wafer, then a thick top layer of PDMS (~0.7 cm) containing the channel patterns was aligned over the vias. A small amount of Si oil was placed on the lowest portion of the top layer to prevent it from bonding to the thin membrane. The two layers were allowed to cure together overnight through partial curing. Once cured, the wafer and device with the thin membrane were removed from the oven, and a scalpel was used to cut around the chip, thus freeing the thin membrane from the PDMS around it. Slowly, one corner of the chip was lifted up and the chip and membrane were removed from the wafer. Although not 100% efficient (success rate was around 70%), the bonded device with membrane with the via could typically be removed intact. The 3rd layer could now be attached to the other 2 layers by plasma oxidation, using a microscope to align the layers and making sure all three components were in the correct position. The three photomask designs used to fabricate these fluidic diode structures are shown separately in **Figure 2.10**.

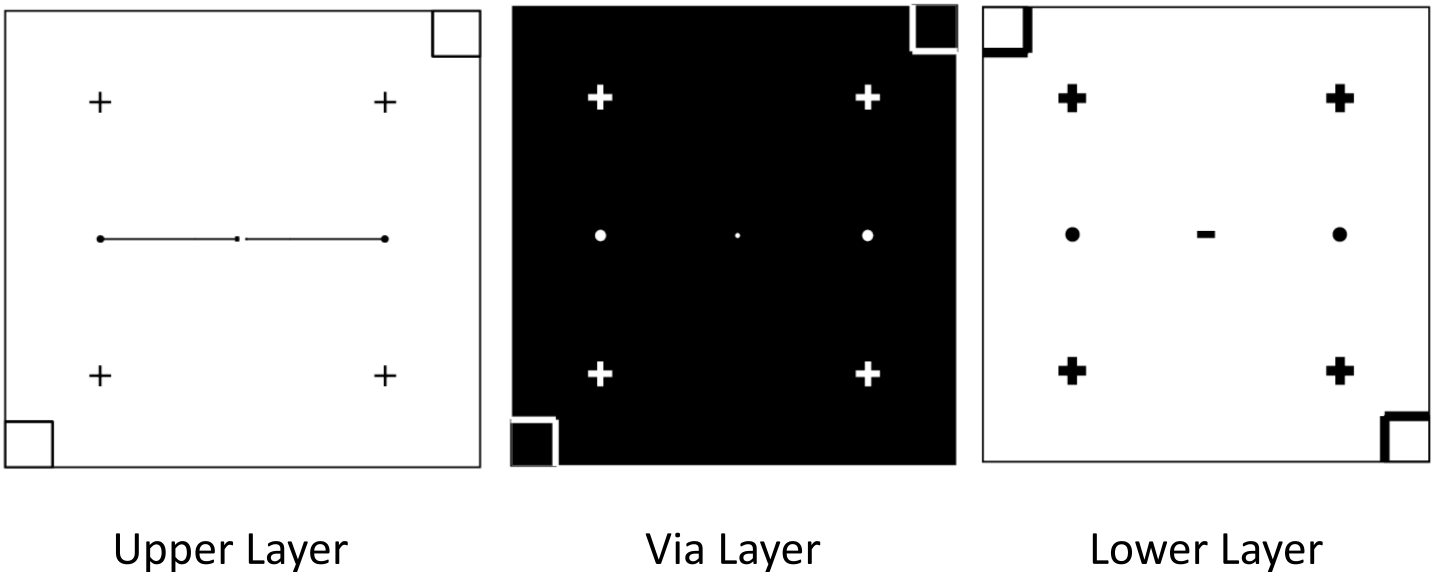

Upper Layer

Via Layer

Lower Layer

Figure 2.10 Photomask designs of the 3 layers used to fabricate fluidic diodes. The PDMS layers were molded individually, then aligned and bonded to create the final device.

2.3.2.2: Prototypes of functional diodes

A schematic of the completed design is shown in **Figure 2.11**, where each individual layer is illustrated. Reservoirs were punched on the inlet side of the device for adding solutions, and a vacuum outlet could be punched on the other side of the device. Flow rate through diodes at varying pressures were measured by marking position of the outlet fluid in a clear tube of known dimensions, then recording distance travelled after a period of 5 minutes. Vacuum levels applied to different chips were varied, and flow rate vs. pressure curves were generated. Although fabrication success rates were low, several chips were functional. **Figure 2.12** shows results from a successfully fabricated device, where the expected proportional relationship between flow rate and pressure were observed, while backflow was completely inhibited at all tested pressures. These results are encouraging for future work in applying fluidic diode structures to droplet generation and manipulation, as well as for possible applications in secretion sampling.

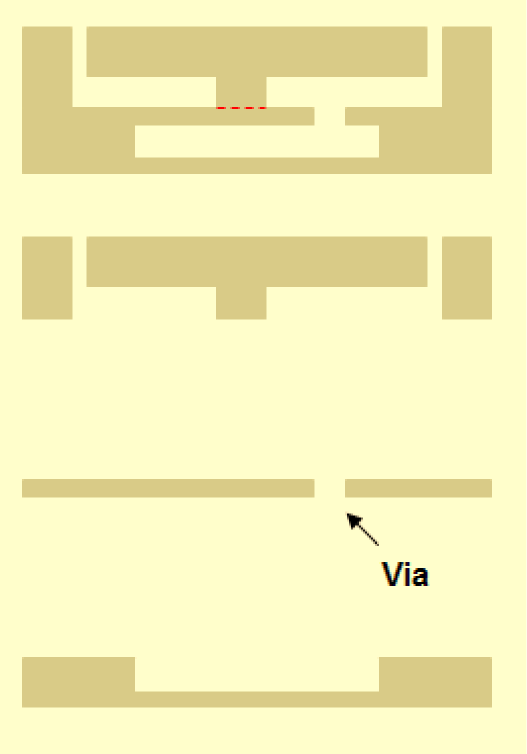

Figure 2.11 Schematic of a cross sectional view of the completed diode chip and the 3 individual layers. The bottom layer allows the thin membrane with the via to flex, the middle layer contains the via, and the top layer contains the two channels and wall that serves as the functioning portion of the diode. The dotted line represents non-bonded PDMS region.

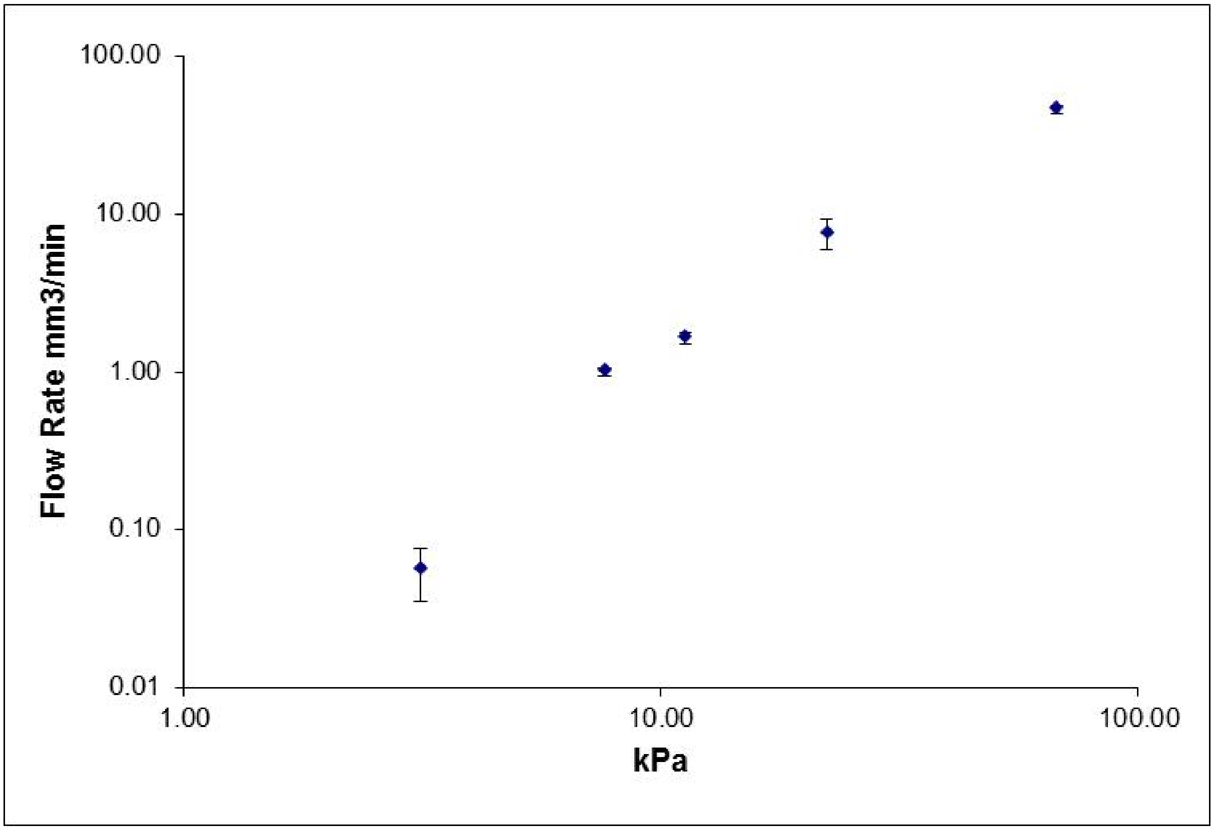

Figure 2.12 Flow rates through three successfully fabricated microfluidic diodes showed the expected proportional increase in flow rate with pressure in forward operation, while backflow was prevented at all tested pressures.

2.4: Handheld Syringe Validation

Throughout this dissertation work, most devices were operated passively, where the flow control system consisted of a PDMS chip, tubing, and a handheld syringe to apply vacuum to the outlet. Although other groups have shown this approach to be very consistent [7], our system was also validated by performing 30 pressure measurements over an extended period of time. Vacuum sensors reported a voltage, which was recorded using an in-house written LabVIEW application (National Instruments) (**Figure 2.13).** Wooden spacers were used to more consistently define the starting and stopping points of the syringe plunger. At a constant pressure of ~8 kPa, the sensor voltage was 0.229 ± 0.005, representing a relative standard deviation of 2.16 % over 30 separate applications of vacuum. These results were encouraging for our flow control system and matched that of previous reports [7].

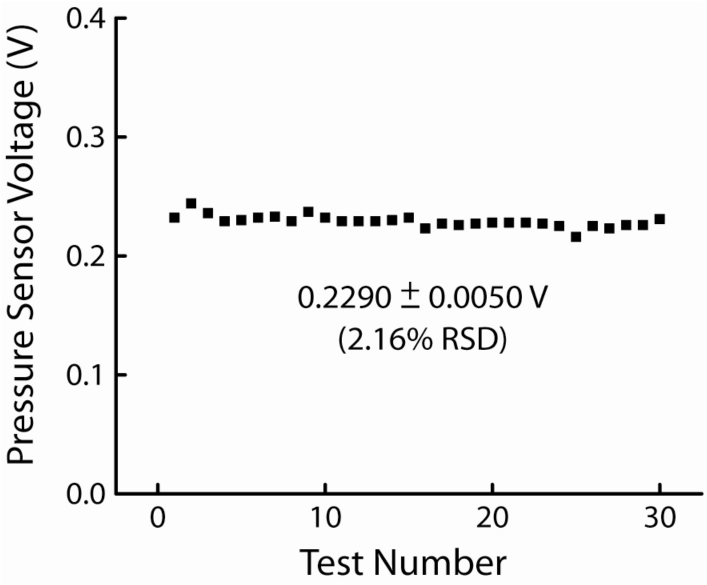

Figure 2.13 A vacuum pressure sensor was used to determine the precision of vacuum levels generated using the handheld, 100-mL syringe filled with air. Each of the 20 points represents a separate starting and stopping of the syringe plunger, using spacers to generate a vacuum of ~8 kPa. This approach was shown to be highly consistent, with approximately 2% relative standard deviation.

2.5: Leading up to Microfluidic Lock-in Detection

2.5.1: Toner transfer masking based designs

The TTM design uses 3 inlets, 1 oil, 2 aqueous coming together in the center of the chip, then connecting to the outlet channel. These are connected through a rectangular region where the oil splits into 2 different channels, each leading to one of the aqueous channels then joining back together to create the outlet. The major problem with this design was that droplets were difficult to form. We believe this to be from variations in the design due to etching problems.

2.5.2: Final design with directly opposing droplet generators

Since fabrication consistency was a problem with TTM, we chose to use the more consistent SU-8 based soft lithography for fabrication of future signal/reference generating droplet devices Also, a change in design was introduced, in which fluidic pressure coupling between droplet generators was increased by removing channel branching. A master was fabricated with this new design, which again consisted of 3 channels: 1 oil and 2 aqueous channels (**Figure 2.14).** The oil channel was 100 μm wide, and the aqueous channels were 50 μm wide. All channels were approximately 30 μm in height. Interestingly, this simplified design of directly opposing droplet generators did indeed increase fluidic pressure coupling, providing consistent alternation of sample and reference droplets. This is believed to be caused by a more dramatic change in pressure associated with each channel. It appears that as one drop begins to exit the aqueous channel and expands into the oil channel, this creates a pressure increase in the oil channel, as the oil is partially blocked. As this droplet is segmented and swept away by the oil, a decrease in pressure is created at the droplet formation region of that channel, thereby allowing the buildup of pressure in the opposing generator to force out aqueous phase and begin the steps of droplet formation there. The process is repeated over and over, allowing droplets to be created alternately by each channel at high consistency. With this new design, we were able to apply lock-in analysis methods. Since the device passively chops the fluidic sample, rather than an optical beam, we referred to this device as the μChopper. This device was used in the chapters to follow for improving sensitivity in absorbance and fluorescence detection.

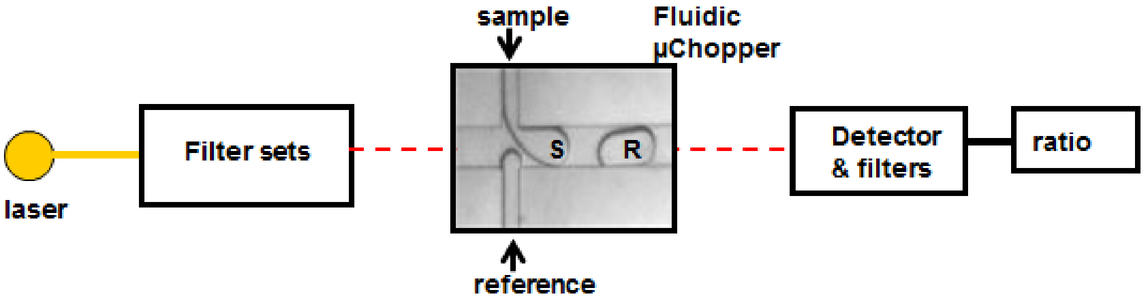

Figure 2.14 Block diagram of µChopper set-up using our alternating droplet design as a fluidic chopper instead of a chopper mirror.

2.6: References

1. Easley, C. J.; Benninger, R. K. P.; Shaver, J. H.; Head, W. S.; Piston, D. W. *Lab Chip* **2009,** 9, 1119-1127.
2. Rissin, D. M.; Walt, D. R. *Nano. Lett.* **2006,** 6, 520-523.
3. Koo, H.; Velev, O. D. *Biomicrofluidics* **2013,** 7, 031501.
4. Zheng, Y.; Shojaei-Baghini, E.; Wang, C.; Sun, Y. *Biosens. Bioelectron.* **2013,** 42, 496-502.
5. Leslie, D. C.; Easley, C. J.; Seker, E.; Karlinsey, J. M.; Utz, M.; Begley, M. R.; Landers, J. P. *Nature Phys.* **2009,** *5*, 231-235.
6. Mosadegh, B.; Kuo, C. H.; Tung, Y. C.; Torisawa, Y. S.; Bersano-Begey, T.; Tavana, H.; Takayama, S. *Nature Phys.* **e** *6*, 433-437.
7. Leslie, D. C.; Melnikoff, B. A.; Marchiarullo, D. J.; Cash, D. R.; Ferrance, J. P.; Landers, J. P. *Lab Chip* **2010,** *10*, 1960-1966.

Chapter 3: Lock-in Detection for Microfluidic Absorbance Measurements

3.1: Introduction.

Microfluidic systems have found widespread use in a variety of fields, including single-cell analysis, emulsion formation, cell secretion sampling, oligonucleotide synthesis, cell concentration, chemical waveform generation, millisecond kinetic measurements, and even for purification of rare circulating tumor cells from blood [1-8]. Various optical detection methods have been interfaced with microfluidics, most notably fluorescence detection due to its high sensitivity and low background [9]. However, absorbance detection has found limited use with the microfluidic platform. There exists a fundamental incompatibility in the use of absorbance detection with microfluidic systems, namely, the path length dependence of the Beer−Lambert law [10-12]. As light transmits through the micrometer-scale path lengths of these fluidic channels, absorption even by high concentrations of analytes can be indistinguishable from that of the blank solution. Various avenues have been explored to overcome this incompatibility;

for example, integration of fiber optics during device fabrication, geometric extension of path lengths, and thermo-optical laser absorbance methods [13-15]. However, these methods typically require specialized, expensive, or tedious fabrication procedures to accomplish. As such, there is a need for a simpler, robust method to overcome the path length limitation and bridge absorbance detection with microfluidic analyses. A simplified microfluidic platform for absorbance detection could greatly expand analytical capabilities for biological applications, such as interrogating small numbers of cells, and would nicely complement the successes of fluorescence and electrochemical detection methods at this scale [16-20].

Herein, we show that droplet microfluidics (i.e., segmented flow) can provide a fluidic system analogous to an optical beam chopper, permitting lock-in detection for femtomole analyte detection limits with absorbance through an optical path length of only 27 μm. As with optical beam choppers, our droplet fluidics approach is capable of modulating an input signal to higher frequencies (~10 Hz), which enables low frequency noise to be ignored through constant referencing to a control sample. This is accomplished without adding steps to the standard soft lithography and without specialized optical coupling to the microdevice [21]. Key to this advancement is the self-regulated, robust formation of alternating signal and reference droplets afforded by directly opposing droplet generators that empty into a single measurement channel. Similar to our previous fluorescence referencing approach, Marz et al. have recently employed this referencing concept with surface-enhanced Raman scattering (SERS), using mixing of multiple droplet trains and without utilizing lock-in analysis [16-22]. Our system for absorbance measurements is more simplified, including passive flow control using a hand-held syringe, self-regulated droplet alternation routed into a single output channel, no requirement for droplet mixing, and detection via optical microscopy [16, 23, 24]. Throughout this dissertation work, we refer to this system as a microfluidic sample chopper (μChopper). Although we validate the system with visible absorbance detection, the μChopper concept is general and should be immediately applicable to reducing noise in other optical methods such as UV or IR absorption, Raman scattering, and fluorescence. In fact, a fluorescence version of the μChopper is the subject of the following chapter.

3.1.1: Materials.

Polydimethylsiloxane (PDMS) precursors were obtained from Dow Corning (Sylgard 184). Tubing (TGY-020- 5C; 0.02 in. ID, 0.06 in. OD, 0.02 in. wall) and blunt needles (NE-223PL-C 22G) for interfacing to the microdevice were obtained from Small Parts. Bromophenol blue (BPB) (EMD Chemicals) and fluorescein (Alfa Aesar) were obtained from Sigma Aldrich. Buffered aqueous solutions were in either phosphate buffered saline (pH 7.4) or were made from varying ratios of citric acid monohydrate and dibasic sodium phosphate (pH 2.76−7.79), both obtained from Sigma-Aldrich. Two reference solutions were utilized in this work. Absorbance calibration was accomplished using a phosphate buffered saline solution as the reference (pH 7.4), while the nanoliter pH sensing was carried out using citric acid/sodium phosphate buffer as a reference (pH 4.7). Droplet carrier fluid was a fluorocarbon oil and surfactant, namely, 1.8% w/w Krytox 157 FSL surfactant (Dupont) in HFE-7500 oil (3M) [25]. The fluorocarbon carrier and surfactant helps to minimize exchange of compounds between aqueous and oil phases, as well as preventing adsorption to the channel walls. To prepare the carrier fluid, 20 g of Krytox 157 FSL was dissolved in 180 g of methanol. A faint white solution formed, to which ~0.6 g of ammonium hydroxide was added dropwise with stirring, resulting again in a transparent solution. Excess ammonium hydroxide and methanol were evaporated by stirring overnight in a fume hood, resulting in the solidified ammonium carboxylate salt of the surfactant. A portion of this solid was weighed and added to HFE-7500 oil to give a 1.8% w/w mixture. This mixture was heated and stirred to dissolve the surfactant and was used as the droplet carrier fluid.

3.1.2: Microchip Fabrication.

PDMS microchips were fabricated using standard soft lithography [21]. PDMS elastomer base and curing agent were mixed in a 10:1 ratio, poured over the master defined by photoresist (SU-

8, Microchem) on a silicon wafer, and cured overnight at 65 °C. Patterned PDMS was removed from the silicon master, cleaned with methanol, air-dried with a nitrogen stream, and then bonded immediately to glass slides after exposure to an air plasma for 45 s (Harrick Plasma). Microchannels were then treated with Aquapel (Pittsburgh Glass Works), rinsed with methanol, and placed in an oven at 65 °C overnight prior to use. Flow control in the microfluidic devices was achieved passively using a hand-held, 100-mL syringe (SGE Analytical Science) connected to the devices via 0.02 in. ID Tygon tubing (Small Parts).

3.1.3: Absorbance Measurements.

Standard absorbance measurements were performed using a NanoDrop 1000 (Thermo Scientific) with a 1 mm optical path length. Microchip absorbance measurements (27 μm optical path) were made using a confocal microscope in transmission mode with a 561 nm laser (Nikon A1R), collecting 512 × 32 pixel images (12 bit intensity) at 196 frames per second. Droplet formation was monodispersed and was maintained at ∼7−10 Hz from each channel (∼14−20 Hz total droplet frequency). For calibration, data was collected for 30 s for each BPB concentration, including the blank solution. A washing step was performed between sample changes in the inlet reservoir by removing the remaining volume of BPB solution, adding the next concentration to the reservoir in excess, and rinsing 2 or 3 times. Vacuum application was maintained, and a wait period of 5 min was observed between sample changes to ensure complete replacement with the new solution. Image analysis was performed using NIS Elements software (Nikon) and Microsoft Excel. Spikes in data recorded in regions of interest (ROIs) for further analysis were removed using a standard deviation filter (Nikon Elements software), an efficient approach to ignore droplet edges when necessary.

For pH sensing, a citric acid/sodium phosphate buffer with a pH of 4.72 was used as the reference, with each sample containing 100 µM BPB in a range of the same type of buffers from pH 2.76 to 7.79. Vacuum was applied to the chip, and droplet formation was allowed to stabilize during a wait time of 5 min. Each solution was placed in the sample or reference reservoirs, and data was collected for 30 s for each run (200− 300 droplets of each type, 400−600 total). The sample reservoir was rinsed, washed, and then refilled with the next buffer, and the chip was allowed to run for 5 min to ensure complete washing between sample changes. Image analysis was performed as described above and in the text.

3.1.4: Droplet Frequency Measurements.

Measurements of droplet formation frequency at various pressures in different microchip designs were performed in quadruplicate by imaging formation of aqueous fluorescein-filled droplets with an inverted fluorescence microscope (Nikon Ti-E) at ~40 frames per second. Image analysis was performed using NIS Elements software (Nikon) followed by Matlab. Vacuum pressure measurements were performed using an in-house built instrumentation amplifier and two differential pressure sensors (Honeywell 26PCCFB6G, Allied Electronics) interfaced with an in-house written LabVIEW application (National Instruments). One sensor was connected in parallel to the syringe and microchip, while the other was referenced to atmospheric pressure. Vacuum pressure (lower than atmospheric pressure) is represented as a positive value in the manuscript.

3.2: Results and Discussion

3.2.1: Device Design and Operation.

The microfluidic device design consisted of three inputs and a single output and was designed for entirely passive operation using a single hand-held syringe (**Figure 3.1).** The aqueous (sample and reference) and oil inputs were interfaced with the microchannels through particulate filters built into the chip design to prevent clogging during operation [25]. The intersection of the two aqueous channels (50 μm widths) with the oil channel (100 μm width) resulted in two opposing T-junction droplet generators [16, 26]. As in our previous work, droplet formation was achieved passively by applying vacuum to the outlet with a single hand-held syringe, providing a simplified user interface for device operation [16, 23]. With the two directly opposing droplet generators, alternating droplet formation from each aqueous channel occurred effortlessly in a self-regulated manner (**Figure 3.2).** For clarity, the image montage in Figure 3.2 is a decimated version of a segment of the video, depicting every third image collected at 196 fps. This preferred alternating temporal response of the fluidic system was the key functionality that allowed sample droplets to be immediately followed by reference droplets in a consistent manner, which was the enabling feature in performing lock-in detection in this system. The sample chopping and lock-in detection allowed for significant rejection of noise at frequencies and phases different from that of the droplet formation, particularly the high magnitude 1/f noise or drift. The consistent frequency and phase of droplet formation is described below.

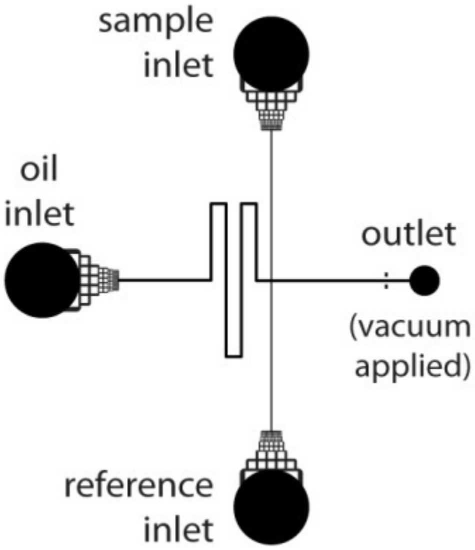

Figure 3.1 The microchannel layout is shown, with punched reservoirs depicted by filled black circles and labels for the two aqueous inlets (sample and reference), one oil inlet, and one outlet. A hand-held syringe was used to apply vacuum to the outlet. Used with permission from the Copyright Clearance Center and Deal, K. S.; Easley, CJ. *Anal. Chem.;* **2012,** 84, 1510-1516. Copyright 2012. American Chemical Society.

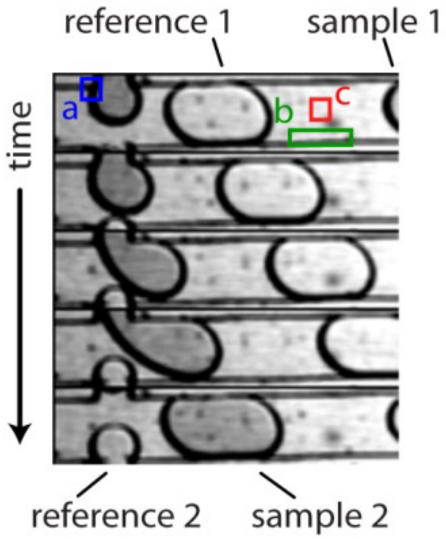

Figure 3.2 The two opposing droplet generators exist at the intersection of the three input channels. An image montage shows a decimated segment of video collected at 196 fps (~15 ms between images) in transmitted light mode during the self-regulated switching of sample (darker droplets) and reference aqueous inputs at the droplet formation regions. Used with permission from the Copyright Clearance Center and Deal, K. S.; Easley, CJ. *Anal. Chem.;* **2012,** 84, 1510-1516. Copyright 2012. American Chemical Society.

3.2.2: Characterization of Device and Methodology.

We first characterized droplet formation within the μChopper as a function of applied vacuum level and oil channel length. Three device configurations with different lengths of oil input channels were characterized, referred to as short, medium, and long resistors (15.24, 20.32, and 25.36 mm in length, respectively). In these experiments, a wide-field microscope was used to measure the formation frequency of fluorescent droplets. As shown in **Figure 3.3**, a proportional increase in droplet formation frequency was observed as a function of pressure for all three device designs, with only a modest difference observed among the different oil channel lengths. A consistently higher frequency of droplet formation was observed for the longest channel, presumably since the more resistant oil channel necessitated that the aqueous solution flow rate be higher. No significant change was observed in droplet size at different pressures. These results suggested that droplet formation was more dependent on channel dimensions and surface chemistry at the T-junction droplet generators than by the relative fluidic resistances of the input channels, consistent with previous reports [26]. Guided by this characterization, for proof-of-concept of the μChopper system, we chose conservative formation frequencies of ∼10 Hz. This helped to avoid under-sampling in droplet imaging at 196 frames per second and simplified data analysis. All experiments to follow in calibration and pH sensing were performed at 5−6 kPa of vacuum pressure using the middle length device (20.32 mm oil channel length), resulting in 7−10 Hz formation of each droplet.

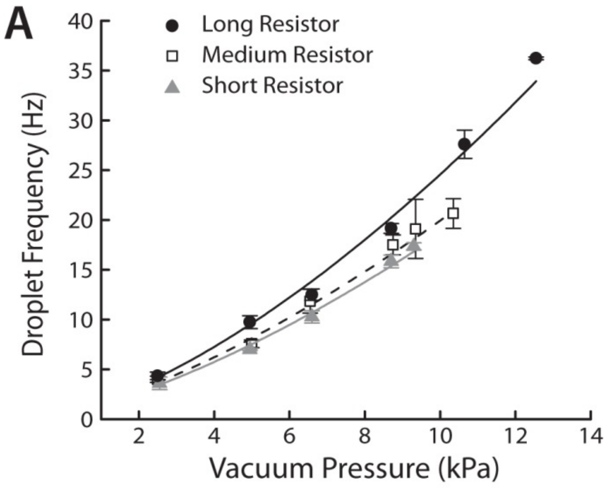

Figure 3.3 The formation frequency for each set of droplets was found to be proportional to applied vacuum levels. Varying oil channel lengths (resistors) showed modest differences in response, suggesting a more important role for surface chemistry and channel dimensions at the droplet generators. Error bars represent standard deviations of triplicate runs. Used with permission from the Copyright Clearance Center and Deal, K. S.; Easley, CJ. *Anal. Chem.;* **2012,** 84, 1510-1516. Copyright 2012. American Chemical Society.

An important benefit of the self-regulated, consistent droplet alternation was that the frequency and phase of the lock-in trigger data (green and blue traces in **Figure 3.4**) would automatically adjust, even if applied vacuum levels were variable. This added to the ease of operation of our device, making it less important to tightly regulate vacuum pressure levels in the syringe connected to the outlet channel. **Figure 3.5** shows the frequency and phase spectra from Fast Fourier Transfer analyses (FFT) of the fluorescence imaging of droplet formation. These are examples of spectra used to assemble the plot in Figure 3.3. As depicted in Figure 3.5, and at all applied pressures, the fundamental frequencies of sample and reference droplet formation were always equal (f_S, black trace; f_R, gray trace). Observed lower intensity harmonics were expected, since this frequency-domain pattern is consistent with the recorded time domain fluorescence data that resembled a truncated sawtooth waveform. In addition, the phase of sample (θ_S) and reference (θ_R) droplet formation were always of opposite sign and approximately equal magnitude (θ_S, blue trace; θ_R, cyan trace). At the fundamental frequency, the relative phase of sample and droplet formation (θ_S/θ_R) at all pressures was measured as -1.06 ± 0.17. This essentially 180° phase shift defined the self-regulated alternation, or switching, between sample and reference droplets, which allowed fluidic sample chopping.

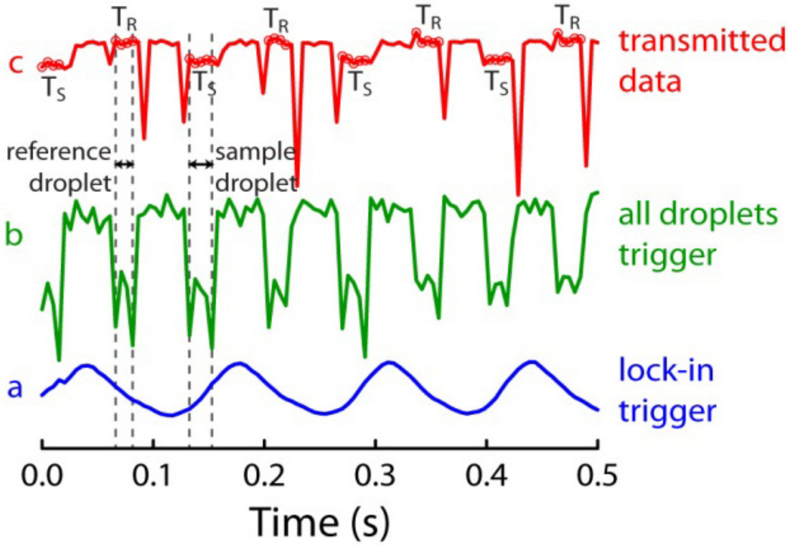

Figure 3.4 Regions of interest (ROIs) used for data analyses are color coded and labeled. Example raw transmitted light data, used for lock-in analysis, is color coded with the respective ROIs. The droplet and lock-in triggers are used to automatically determine droplet identity, even when signal is indistinguishable between sample and reference droplets. Used with permission from the Copyright Clearance Center and Deal, K. S.; Easley, CJ. *Anal. Chem.;* **2012,** 84, 1510-1516. Copyright 2012. American Chemical Society.

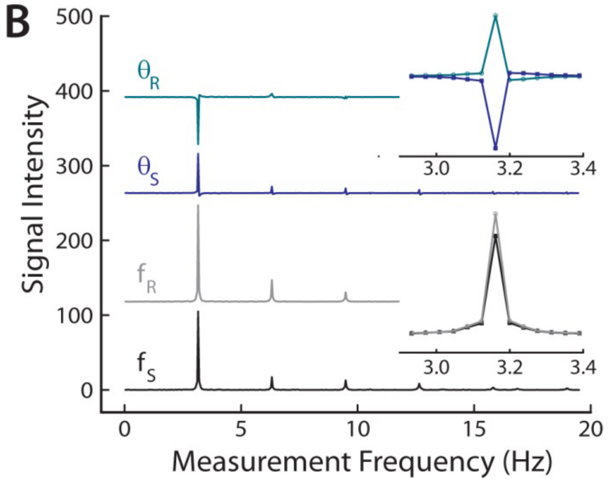

Figure 3.5 Example data from Fourier analyses. The frequency and phase spectra of sample droplet formation (f_S and θ_S, respectively) and for reference droplet formation (f_R and θ_R, respectively) are plotted versus measurement frequency. Inset plots show that the fundamental frequencies of each set of droplets were equal ($f_S = f_R$) and that $\theta_S \approx -\theta_R$, which was consistent at all applied pressures. Used with permission from the Copyright Clearance Center and Deal, K. S.; Easley, CJ. *Anal. Chem.;* **2012,** 84, 1510-1516. Copyright 2012. American Chemical Society.

3.2.3: Absorbance Detection in Micrometer Optical Paths.

The absorbance detection of BPB was achieved on-chip by imaging droplets just downstream of the droplet generators (Figure 3.2) in transmitted light mode with a confocal microscope (561 nm laser). Absorbance was defined as $\log(T_R/T_S)$, where T_R is the mean transmitted light intensity within ROI-c for the reference droplet and T_S is the mean transmitted light intensity within ROI-c for the sample droplet. The lock-in detection approach was made possible by also analyzing regions of interest (ROIs) at one of the droplet generators (ROI-a, blue) and at the edge of the channel downstream (ROI-b, green). With dark droplet edges giving a decrease in transmitted light signal, data from ROI-b allowed us to confirm passage of every droplet as a signal decrease in the green trace, serving as a trigger for all droplets. Of chief importance was the signal from the sample droplet input (ROI-a, blue), which was automatically locked-in to the frequency and phase of sample droplet formation from the upper aqueous channel. In contrast to the other ROIs, the droplet edge never actually leaves ROI-a; thus, the percentage of droplet edge in ROI-a gives a signal fluctuation that is locked-in to the downstream droplet train. As shown in the blue trace in Figure 3.4 (right), ROI-a served as the lock-in trigger, which always showed positive slope during passage of a sample droplet through the detection region (ROI-c) and negative slope during passage of a reference droplet. Data from ROI-a (blue) gave us the ability to discriminate between sample and reference droplets, even when the sample droplet contents were undetectable, analogous to the tracking signal from an optical beam chopper in an electronic lock-in detector. On the contrary, no additional effort was required to synchronize the lock-in trigger, since this data was intrinsically locked-in to droplet formation, even during changes in formation frequency. Data alignment is marked with dashed gray lines in Figure 3.4. With sample and reference droplets at equal frequency and 180° out of phase, the lock-in trigger (blue) could consistently identify the origin of each droplet for further analysis. Using Figure 3.4 to summarize the analysis, data in the red trace (mean of ROI-c) was processed as sample droplet data (T_S) only when two conditions were met: (1) the green trace (ROI-b) was in the lower state and (2) the blue trace (ROI-a) had positive slope. Similarly, data in the red trace was processed as reference droplet data (T_R) only when these conditions were met: (1) the green trace (ROI-b) was in the lower state and (2) the blue trace (ROI-a) had negative slope. Selected data are represented in Figure 1 as open red circles superimposed on the red trace from ROI-c; each set is labeled with either T_R or T_S for reference or sample transmittance, respectively. Treating all nonselected data from ROI-c as zero intensity, the selected data (open red circles) was then averaged with the zeroed data using a specific time constant of the lock-in analysis (1.9 s chosen below) and then renormalized on the basis of the duty cycle to give continuous traces of transmitted intensity that will later be described in detail. Absorbance traces were then generated, dividing the reference trace by the sample trace and then taking the logarithm of this data ($\log(T_R/T_S)$. Note that negative spikes in data from ROI-b and ROI-c represent droplet edges, which were filtered from the selected data in ROI-c using a simple standard deviation filter using Nikon Elements software. Following this analysis permits the translation of sample and reference droplet pairs at ∼10 Hz into continuous absorbance traces with significantly reduced noise levels, which defines the main function of the μChopper.

Upon inspection of the traces in Figure 3.4, it can be seen that T_S was clearly of lower intensity than T_R . This result was expected, since BPB absorbs significantly at 561 nm. The concept of low absorbance in short path lengths can be illustrated here by the relatively low signal-to-noise at high BPB concentration, and the middle image montage shows only modest differences in intensity between signal and reference at 100 μM BPB (Figure 3.2.). Lower concentrations of BPB were undetectable by direct observation of images or raw data. The lock-in detection methodology was, therefore, necessary for recovery of low signal-to-noise absorbance measurements in this 27 μm optical path, as much as 200-fold lower than that shown in Figure 3.4.

To calibrate the system, the μChopper device was used with microscopy to fluidically chop and measure absorbance of various concentrations of BPB, followed by analysis as described above. **Figure 3.6** shows continuous data after processing with much of the lock-in methodology, excluding the final ratiometric calculation that determines absorbance. This way, the relative magnitudes of signal and 1/f noise or drift can be visualized. The reference (red) and sample (black) traces represent the transmitted intensity of the 561 nm laser in each droplet train over time. Breaks in data traces separate duplicate runs of the same sample (~200 droplets each). Dotted lines mark breaks in collection, in which inlet solutions were replaced with the next BPB concentration followed by wait periods; thus, the plot is not meant to show continuous acquisition. As shown in this data, drifts in signal as large as ~75 intensity units were observed over the full data collection period (~1.5 h, real time), and other low frequency noise was clearly present. This was an important observation, since even the solution with the highest BPB concentration (100 μM) resulted in only ~75 units of differential intensity, approximately equal to that of the drift. The correcting effect of the constant referencing to neighboring droplets is illustrated by **Figure 3.7**, which shows the continuous absorbance trace that was calculated from data in Figure 3A. The large drifts were corrected by this process, and other low frequency noise components were essentially negated.

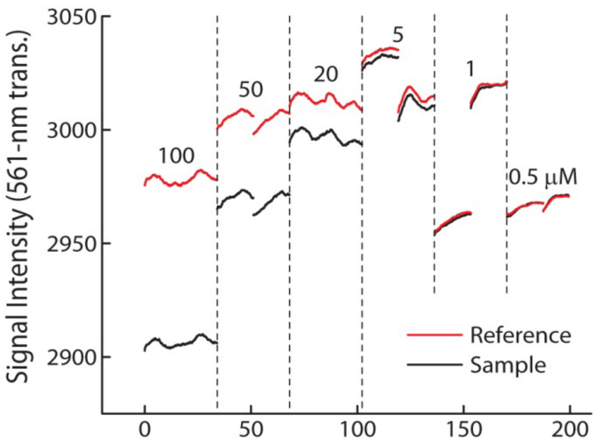

Figure 3.6 Absorbance of 561-nm light by BPB in a 27-μm deep channel. Processed data is shown just before the final ratiometric step, showing large signal drifts that would typically make these measurements impossible. Used with permission from the Copyright Clearance Center and Deal, K. S.; Easley, CJ. *Anal. Chem.;* **2012,** 84, 1510-1516. Copyright 2012. American Chemical Society.

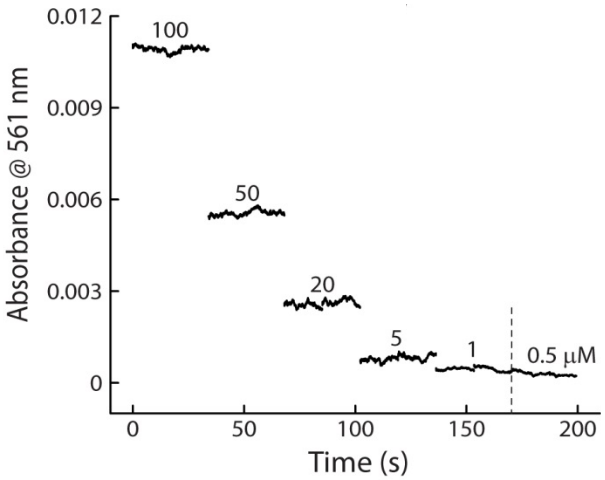

Figure 3.7 Constant referencing with alternating sample and reference droplets at ~10 Hz each eliminated much of these low frequency noise components. Used with permission from the Copyright Clearance Center and Deal, K. S.; Easley, CJ. *Anal. Chem.;* **2012,** 84, 1510-1516. Copyright 2012. American Chemical Society.

The entire data sets shown in Figure 3 .6, 3.7 were not required for calibration but are shown for purposes of illustration. To determine the minimum amount of data required for analysis, i.e., to find the optimal time constant for lock-in analysis using the μChopper, time constants were varied between 0.16 and 5.1 s (~1 droplet to ~40 droplets). The standard deviation of the blank measurement (σ_{blank}) was determined at each time constant, and the result is plotted in **Figure 3.8**. Measurements represent quadruplicate analyses of two separate runs. It was clear from the figure that a minimum level of noise was detected at a time constant of 1.9 s (~15 droplets). This time constant was applied to the data to follow.

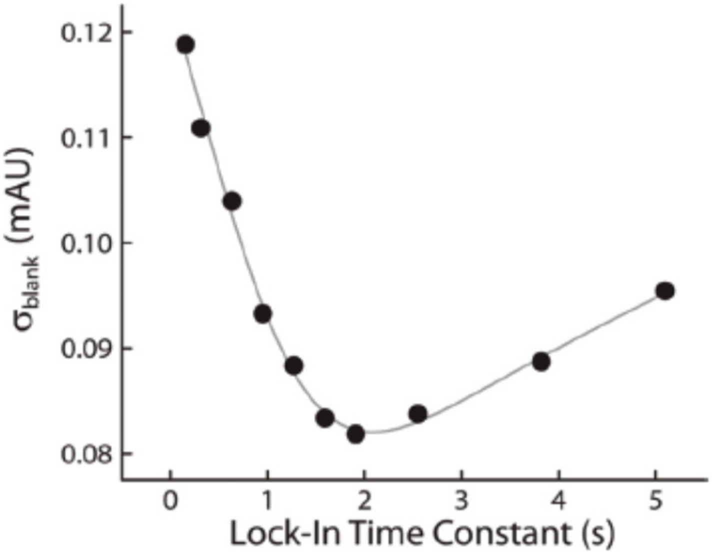

Figure 3.8 Characterization of the effect of time constant in the lock-in analysis revealed minimal noise at a time constant of 1.9 seconds. Used with permission from the Copyright Clearance Center and Deal, K. S.; Easley, CJ. *Anal. Chem.;* **2012,** 84, 1510-1516. Copyright 2012. American Chemical Society.

From data such as that shown in Figure 3.6 and 3.7, a calibration curve was assembled (**Figure 3.9**). This curve was generated from quadruplicate measurements on two runs at each concentration, using a lock-in time constant of 1.9 s. The absorbance response was linear (R^2 = 0.9988), and the extinction coefficient measured with the 27 μm optical path length at 561 nm was 39 600 ± 800 M−1 cm−1. This value was in good agreement with the 42 300 ± 700 M−1 cm−1 value measured with a standard spectrometer, validating that the μChopper could successfully perform absorbance measurements in short optical paths (27 μm), i.e., validating that the Beer−Lambert law applies to our optical system. Although absorbance of 561 nm light by BPB is only 56% of its maximal absorbance at 592 nm, the experimentally determined detection limit (>3σ) of BPB in the μChopper system was 3.0 × 10−4 absorbance units (AU) or 500 nM (Figure 3.9, inset) using only 59 nL of sample volume (122 droplets), corresponding to 29 fmol of BPB. The extrapolated detection limit (=3σ) was slightly lower, at 2.5 × 10−4 AU or 410 nM BPB. When the same μChopper data were analyzed without the use of constant referencing or lock-in detection, detection limits were as much as 40- to 200-fold higher, depending on the mode of analysis, and absorbance values were significantly less accurate and precise. By comparison, other microfluidic systems engineered for absorbance detection have reported experimentally determined detection limits between 10−3and 10−1AU through path lengths from 23 μm to 1 mm, and more complex thermooptical absorbance approaches have given experimental limits of detection between 1 × 10−5 and 4 × 10−4 AU through path lengths of 30−40 μm [27-29, 30, 31]. Thus, the μChopper compares favorably to previously developed microsystems for absorbance detection, with the added benefit of compatibility with droplet fluidics.

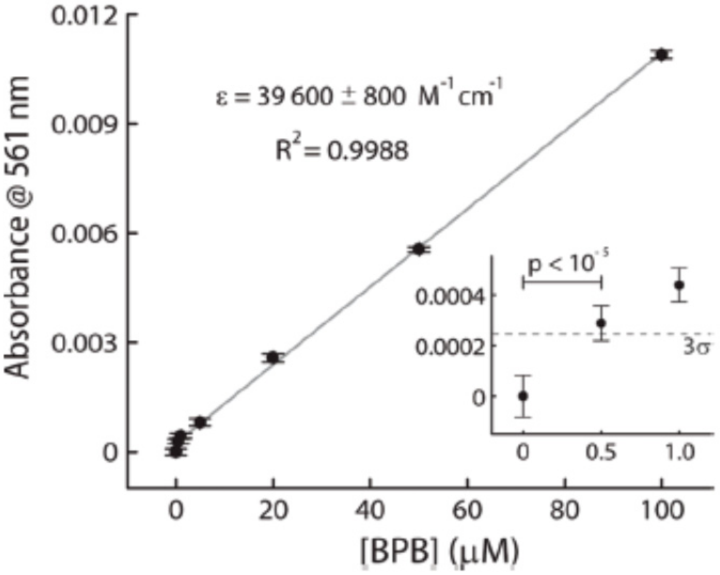

Figure 3.9 The absorbance response was linear, with a measured extinction coefficient (39 600 ± 800 M^{-1} cm^{-1}) in good agreement with that measured using a standard spectrophotometer (42 300 ± 700 M^{-1} cm^{-1}). As shown in the inset, the BPB detection limit (3σ) was 500 nM or 2.9×10^{-4} absorbance units in only 124 nL, corresponding to 62 fmol of BPB. Error bars represent standard deviations. Used with permission from the Copyright Clearance Center and Deal, K. S.; Easley, CJ. *Anal. Chem.;* **2012,** 84, 1510-1516. Copyright 2012. American Chemical Society.

3.2.4: Nanoliter pH Sensing with the μChopper.

Since BPB is an acid/base indicator, it can be used as a pH sensor via optical absorbance readout. Visually, BPB solutions appear yellow at low pH and turn purple as the solution becomes more basic. Using BPB absorbance at 561 nm, the μChopper system was proven capable of pH sensing in nanoliter volumes (**Figure 3.10**). The μChopper was used to chop 100 μM BPB solutions at various pH values (2.76−7.79), and optical microscopy was again used for the readout in transmitted light mode. As shown in Figure 3.10, after processing as described above (1.9 s time constant) to determine absorbance of each solution, we calculated the extinction coefficient (ε) of each solution (filled black circles) to facilitate comparison to a standard spectrometer (open gray squares). The accuracy of our methodology, i.e., adherence to the Beer−Lambert law, was further validated by these results, in which the response versus pH was essentially identical with both methods (two different optical path lengths). Interestingly, the relative error using the μChopper was consistently smaller than that with the standard spectrometer. Thus, pH sensing with the μChopper was possible using only about a hundred droplets of ~500 pL volume, for a total sampled volume of ~50 nL at each pH.

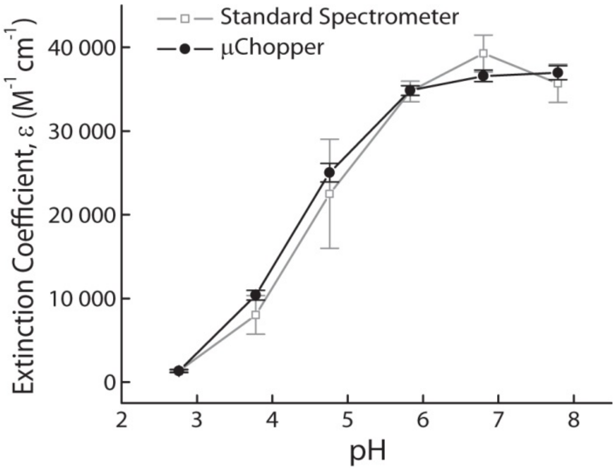

Figure 3.10 Nanoliter pH sensing with the µChopper. Absorbance of 561-nm light by 100 µM BPB was measured by the µChopper at various pH values (2.76-7.79). The trend of extinction coefficient versus pH using the µChopper (filled black circles) was consistent with that using a standard spectrometer (open gray squares), further validating the accuracy of our system. Even though we interrogated a total sampled volume of ~140 nL for each run, error bars (standard deviation) show that the µChopper was consistently more precise than the standard spectrometer for pH sensing. Used with permission from the Copyright Clearance Center and Deal, K. S.; Easley, CJ. *Anal. Chem.;* **2012,** 84, 1510-1516. Copyright 2012. American Chemical Society.

3.3: Conclusions

We have presented the μChopper, a hand-operated microfluidic system that utilizes two directly opposing droplet generators to segment or chop sample and reference solutions into ~500 pL droplets. The μChopper's self-regulated switching between sample and reference droplets is the key functionality that permits the application of a lock-in detection approach for optical measurements. Low frequency noise or drift is essentially negated, allowing sensitive absorbance detection in a 27 μm optical path length.

Since droplets are automatically arranged and then emptied into a single outlet channel for detection, the optical configuration could be simplified in the future to further improve detection limits and to achieve higher droplet throughput than the ~10 Hz shown here (~20 Hz including reference droplets). Additionally, the μChopper approach should be immediately useful with other optical detection methods such as UV or IR absorption, Raman scattering, and fluorescence [32, 33]. For example, a fluorescence-based version of the μChopper could be very useful in measuring secretions from small numbers of cells [16, 23], and this application is described in the following chapter. In contrast to optical choppers, which are decoupled from the fluid under interrogation, the μChopper is capable of limiting diffusion of analytes to allow higher temporal resolution in secretion sampling [16]. Alternatively, with sensitive absorbance detection in the μChopper, droplets from high-throughput, small-volume screening could be reinjected into a μChopper to leverage the variety of available chromogenic assays that are normally incompatible with microfluidics. The μChopper thus has the potential to expand the analytical realm of droplet-based microfluidic systems.

3.4: REFERENCES:

1. Sims, C. E.; Allbritton, N. L. *Lab Chip* **2007,** 7, 423-440.
2. Abate, A. R.; Thiele, J.; Weitz, D. A. *Lab Chip* **2011,** *11*, 253-258.
3. Clark, A. M.; Sousa, K. M.; Chisolm, C. N.; MacDougald, O. A.; Kennedy, R. T. *Anal. Bioanal. Chem.* **2010,** *397*, 2939-2947.
4. Lee, C.; Snyder, T. M.; Quake, S. R. *Nucleic Acids Res.* **2010,** *38*, 2514-2521.
5. Warrick, J.; Casavant, B.; Frisk, M.; Beebe, D. *Anal. Chem.* **2010,** *82*, 8320-8326.
6. Zhang, X.; Grimley, A.; Bertram, R.; Roper, M. G.; *Anal. Chem.* **2010,** *82*, 6704-6711.
7. Song, H.; Ismagilov, R. F. *J. Am. Chem. Soc.* **2003,** *125*, 14613-14619.
8. Nagrath, S.; Sequist, L. V.; Maheswaran, S.; Bell, D. W.; Irimia, D.; Ulkus, L.; Smith, M. R.; Kwak, E. L.; Digumarthy, S.; Muzikansky, A.; Ryan, P.; Balis, U. J.; Tompkins, R. G.; Haber, D. A.; Toner, M. *Nature* **2007,** *450*, 1235-1239.
9. Johnson, M. E.; Landers, J. P. *Electrophoresis* **2004,** *25*, 3513-3527.
10. Kuswandi, B.; Nuriman; Huskens, J.; Verboom, W. *Anal. Chim. Acta.* **2007,** *601*, 141-155.
11. Ro, K. W.; Lim, K.; Shim, B. C.; Hahn, J. H. *Anal. Chem.* **2005,** *77*, 5160-5166.
12. Malcik, N.; Ferrance, J. P.; Landers, J. P.; Caglar, P. *Sens. Actuators B* **2005,** *107*, 24-31.
13. Lei, L.; Mattos, I. L.; Chen, Y. *Microelectron. Eng.* **2008,** *85*, 1318-1320.
14. Petersen, N. J.; Mogensen, K. B.; Kutter, J. P. *Electrophoresis* **2002,** *23*, 3528-3536.
15. Mawatari, K.; Ohashi, T.; Ebata, T.; Tokeshi, M.; Kitamori, T. *Lab Chip* **2011,** *11*, 2990-2993.
16. Easley, C. J.; Rocheleau, J. V.; Head, W. S.; Piston, D. W. *Anal. Chem.* **2009,** *81*, 9086-9095.

17. Roper, M. G.; Shackman, J. G.; Dahlgren, G. M.; Kennedy, R. T. *Anal. Chem.* **2003,** *75*, 4711-4717.

18. Sameenoi, Y.; Mensack, M. M.; Ewing, R.; Dungchai, W.; Chailapakul, O.; Cropek, D. M.; Henry, C. S. *Analyst* **2011,** *136*, 3177-3184.

19. Gunasekara, D. B.; Hulvey, M. K.; Lunte, S. M. *Electrophoresis* **2011,** *32*, 832-837.

20. Viskari, P. J.; Landers, J. P. *Electrophoresis* **2006,** *27*, 1797-1810.

21. Duffy, D. C.; McDonald, J. C.; Schueller, O. J. A.; Whitesides, G. M. *Anal. Chem.* **1998,** *70*, 4974-4984.

22. März, A.; Bocklitz, T.; Popp, J. *Anal. Chem.* DOI: 10.1021/ac2015799. Published online: September 14, 2011.

23. Godwin, L. A.; Pilkerton, M. E.; Deal, K. S.; Wanders, D.; Judd, R. L.; Easley, C. J. *Anal. Chem.* **2011,** *83*, 7166-7172.

24. Leslie, D. C.; Easley, C. J.; Seker, E.; Karlinsey, J. M.; Utz, M.; Begley, M. R.; Landers, J. P. *Nat. Phys.* **2009,** *5*, 231-235.

25. Abate, A. R.; Weitz, D. A. *Biomicrofluidics* **2011,** *5*, 014107, 1-8.

26. Garstecki, P.; Fuerstman, M. J.; Stone, H. A.; Whitesides, G. M.; *Lab Chip* **2006,** *6*, 437-446.

27. Duggan, M; P.; McCreedy, T.; Aylott, J. W. *Analyst* **2003,** 128, 1336-1340.

28. Mogensen, K. B.; Eriksson, F.; Gustafsson, O.; Nikolajsen, R. P. H.; Kutter, J. P. *Electrophoresis* **2004,** 25, 3788-3795.

29. Jindal, R.; Cramer, S. M. *J. Chromatogr., A* **2004,** 1044, 277-285.

30. Uchiyama, K.; Hibara, A.; Sato, K.; Hisamoto, H.; Tokeshi, M.; Kitamori, T. *Electrophoresis* **2003,** 24, 179-184.

31. Dennis, P. J.; Welch, E. F.; Alarie, J. P.; Ramsey, J. M.; Jorgenson, J. W. *Anal. Chem.* **2010,** 82, 4063-4071.

32. Marriot, G.; Mao, S.; Sakata, T.; Ran, J.; Jackson, D. K.; Petchprayoon, C.; Gomez, T. J.; Warp, E.; Tulyathan, O.; Aaron, H. L.; Isacoff, E. Y.; Yan, Y. *Proc. Natl. Acad. Sci. U.S.A.* **2008,** 105, 17789-17794.

33. Mao, S.; Benninger, R. K. P.; Yan, Y.; Petchprayoon, C.; Jackson, D.; Easley, C. J.; Piston, D. W.; Marriot, G. *Biophys. J.* **2008,** 94, 4515-4524.

Chapter 4: Modifications of Microfluidic Sample Chopping for Fluorescence Based Lock-In Detection

4.1: Introduction

Microfluidics has established itself as an important scientific field that continues to expand and develop as a robust tool in new and exciting areas of science. Interest in droplet microfluidics has increased sharply over the last several years and the approach has been combined with many fields of physical and biological science. This opens many doors and eases the development for laboratory and clinical applications in various fields including screening assays, directed evolution of enzymes, PCR applications, and eventually leading up to point-of-care (POC) technologies [1-3]. Although there are many applications of droplet microfluidics, one unique opportunity afforded by picoliter-scale droplet formation that we would like to exploit is for secretion sampling from endocrine tissues. Our laboratory has applied this concept to sampling and quantification of zinc secretion from pancreatic islets, as previously described [4]. However, there are fundamental limitations with currently available assays for protein detection which hinder the progress of developing quantitative microfluidic secretion sampling platforms. Recently, other members of the Easley laboratory have developed new methods for protein detection using direct fluorescence readout that can be applied within picoliter droplets. These assays exploit proximity assembly of antibody-oligonucleotide probes signaled by Förster Resonance Energy Transfer (FRET), and they have been termed proximity FRET assays (pFRET). It has been shown previously that FRET pairs could be used for biomolecular recognition in microfluidic channels using synthetic microbeads [5]. As further developments were made, these applications began branching out to many different assays for a number of molecules and proteins of interest in the mid 2000's [6-8]. For most assays to function properly, it is necessary to have components thoroughly mixed and provide incubation times to provide the best chance for interaction and probe binding to occur. In microfluidics, laminar flow is dominant, and although diffusion will eventually mix all components, the time scale for this process is too great to provide results within a useful time period. There are several microfluidic mixers that have been described in the literature of various designs but all with the same end result [9-14]. Here, we introduce a passively operated microfluidic system capable of completing all aspects of hormone secretion quantitation: endocrine cell secretion sampling, mixing of secreted proteins, thorough incubation with proximity probes, and finally optical quantitation of proteins using fluorescence.

4.2: Experimental

4.2.1: Materials

All chips are made from Polydimethylsiloxane (PDMS) precursors, Sylgard® 184 elastomer base and curing agent, which were obtained from Dow Corning (Midland, Maryland, USA). Silicon wafers were obtained from Silicon Inc. (Boise, ID, USA), SU-8 photoresist and developer were purchased from Microchem (Newton, Massachusetts, USA), and trichloromethysilane was purchased from GFS Organic Chemicals (Columbus, OH). Aquapel for channel coating was purchased from Pittsburgh Glass Works. Tubing for interfacing syringes and devices was obtained from Small Parts (TGY-020-5C; 0.02 in. ID, 0.06 in. OD, 0.02 in. wall), as were blunt ended needles (NE-223PL-C 22G). Carrier oil consisted of HFE-7500 (3M) and Jeffamine additive with a Krytox surfactant based off of a previous method but adjusted to our needs and made in house [15]. Alexa Fluor 647 and Cascade Blue were obtained from Invitrogen (Grand Island, NY) while Fluorescein was obtained from Sigma-Aldrich (St. Louis, MO). LOD and insulin assay uses antibodies from Fitzgerald Industries International (Acton, MA) and oligonucleotides from Integrated DNA Technologies (Coralville, IA). Antibody-oligonucleotide conjugates were made using Solulink conjugation kits (San Diego, CA).

4.2.2: Chip fabrication

The standard soft lithography technique was used for chip fabrication [16]. The microfluidic channel layout was designed in Adobe Illustrator software and sent to Fineline Imaging (Colorado Springs, CO) for photomask printing at 65 024 DPI resolution (negative image). The SU-8 silicon master was fabricated using standard photolithography. After master fabrication, PDMS was mixed in a 10:1 elastomer to curing agent ratio, poured over the silicon master, and allowed to cure overnight at 60 ºC. Once cured, the chips were cut out, holes were punched for vacuum tubing, oil and aqueous phases, and the chip was cleaned with methanol and dried with air. The chip was then plasma oxidized to a clean glass slide and vacuum tubing was inserted. (Harrick Plasma) Channel treatment with aquapel was performed (Pittsburgh Glass Works) then channels were rinsed with methanol, and placed in the oven overnight to remove any leftover solvent.

4.2.3: Chip and experimental design

The chip consists of 3 reservoirs and channels as shown in **Figure 4.1**: one for carrier oil and 2 for aqueous phases. Although there are 2 reservoirs for each aqueous phase, only one reservoir was punched. This design can be used for other experimental set-ups, mainly, direct protein detection, as will be discussed in a later section. The aqueous phases consist of a reference and a sample phase. The reference contains Cascade Blue and Alexa Fluor 647 at 1 µM concentrations along with fluorescein at a concentration of 5 nM for the LOD investigation. The sample consists of Alexa Fluor 647 at 1 µM concentration along with a range of fluorescein concentrations from a blank up to 25 nM. After droplet formation, the droplets move downstream into a mixing region consisting of several turns in a zigzag pattern. Following the mixing region, the droplets enter the incubation portion of the chip. For this portion of the chip, preventing coalescence is mandatory and as previously described, the surfactant being used is an important decision as the droplets will be in close proximity with each other for long periods of time so the surfactant must be able to stabilize them [17]. Originally, this region of the chip consisted of 8 columns ~ 500 µm wide and 100 µm deep chamber with turns at the top and bottom to connect them as shown in **Figure 4.2.A** and **4.2.B.** This design was altered after our preliminary temporal resolution results suggested the design needed to be adjusted to consist of several chambers interconnected by channels just wide enough for single droplets to pass through as seen in **Figure 4.3.A** and **4.3.B** [18]. This design enhances the temporal resolution which is desired for the insulin assays. To reach this conclusion, we used two droplet tracking investigations that allowed droplets to be monitored as they flowed through an incubation channel, as described in the upcoming section.

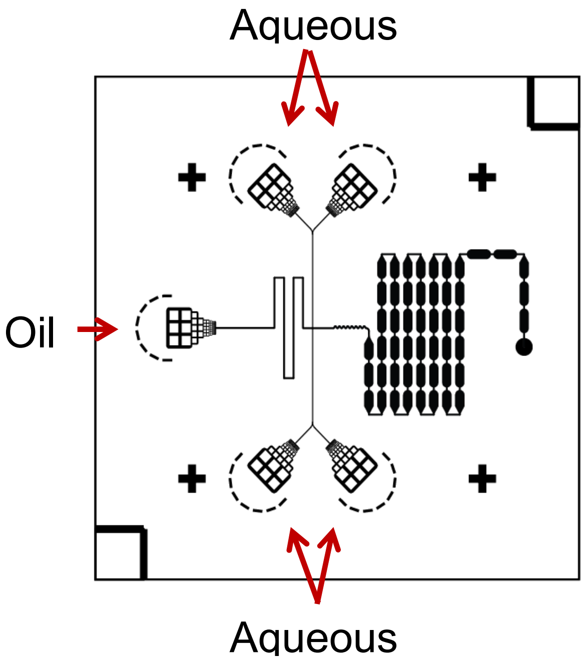

Figure 4.1 Chip design for fluorescent μChopper. This design contains oil, sample aqueous, and reference aqueous phases as well as multiple reservoirs for various reagents, a mixing region after droplet formation, and an incubation region to insure enough time for proper probe and sample interaction to occur.

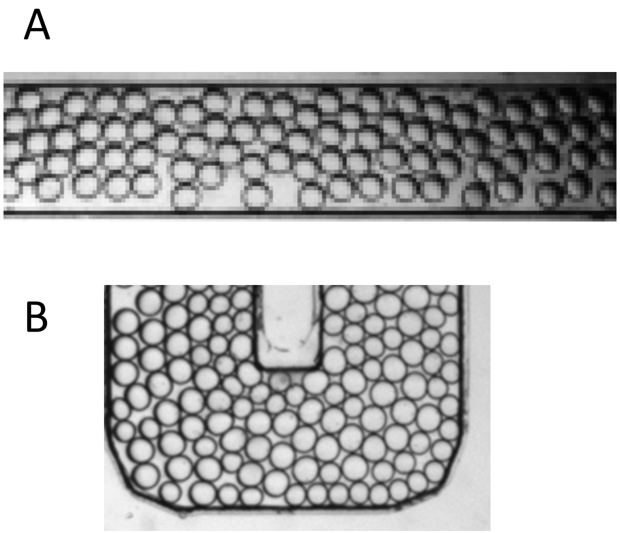

Figure 4.2 Original design of the incubation region of chip utilizing wide channels and wide turns. This design proved detrimental for temporal resolution of the droplets, due to the 'racetrack effect' observed around turns, where inside droplets would overtake outer droplets.

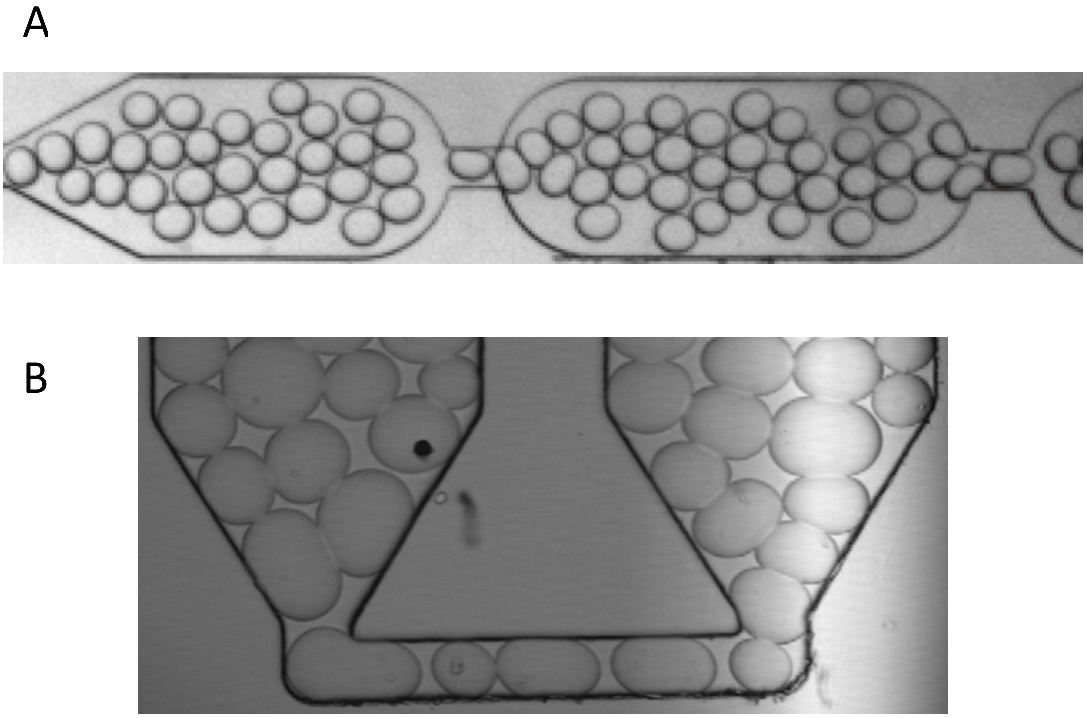

Figure 4.3 Modified design incorporating single droplet channels between chambers and around turns to promote consistent ordering after secretion sampling and greatly improve temporal resolution of the droplet sampling system. (Note: Distortion in image A is occurring due to pixilation.)

4.2.4: Data analysis

Previously, we have shown that a lock-in method can be used with our µChopper system for sensitive absorbance detection [19]. Our goal was to adapt this lock-in methodology for our direct fluorescence based protein assays (pFRET). For our fluorescent lock-in detection, we are using 3 laser lines tuned to the excitation of the 3 fluorescent dyes being used at 405, 488, and 650 nm. In order to perform data analysis with this set-up, we used a confocal microscope to collect the data. We have 2 populations of droplets, a sample and a reference. Each has different fluorescent dyes to distinguish between the 2 populations, and the signal from each dye can be collected separately and split into multiple collection channels via the automated optical layout in the laser-scanning confocal microscope (Nikon A1R), as shown in **Figure 4.4**. We collected data for 20 seconds in triplicate. Fiji or NIS Elements software was then used to isolate intensity data from sample and reference droplets, allowing collection for each frame of the 20 second videos at either 3.6 or 7.0 frames per second. The various dyes allow us to identify droplets as sample or reference with high precision, thus we can constantly lock-in to reference droplets and greatly reduce any noise that is not at the same frequency and phase as the droplets. The data from the train of sample droplets is then compared to the reference data to obtain an intensity ratio, which is directly proportional to analyte or protein concentration.

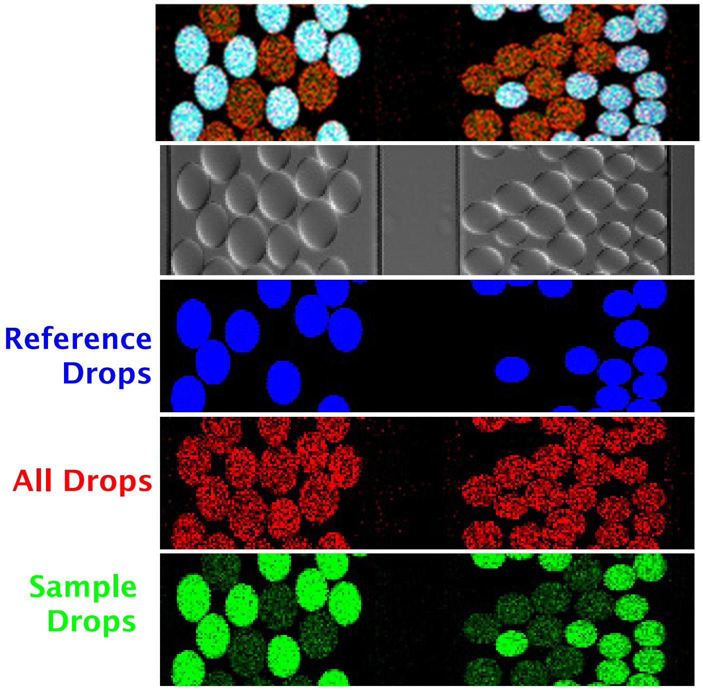

Figure 4.4 Images of various detection channels on the confocal microscope. The top image is a merged image of all fluorescence detectors. The second image shows the transmitted light. The third, fourth, and fifth images show the signals at 406 ± 25 nm (cascade blue), 640 ± 25 nm (Cy5), and 488 ± 25 nm (FAM-labeled probes). Reference droplets are identified by a cascade blue tracer, and all droplets are labeled with Cy5, allowing simple discrimination between sample and reference droplets in the green detection channel.

4.3: Results and Discussion

4.3.1: Limit of detection studies

To obtain a LOD of our fluorescence μChopper system, a calibration curve was generated using various concentrations of fluorescein as the sample. Instead of Cy5 as the marker, Alexa Fluor 647—which showed lower crosstalk with fluorescein emission—was added as the "all droplets" marker into the sample and reference droplets to identify the regions in each image where data will be processed. Cascade blue was again used as the marker to identify the reference droplets only. In reference droplets, we used fluorescein at 5 nM to create a stable baseline to compare the sample droplets against. Along with Alexa Fluor 647 marker, the sample droplets contained a range of fluorescein concentrations. This range consisted of a blank, 25 pM, 100 pM, 1 nM, 5 nM, and 25 nM. We performed 3 runs at each concentration and collected data for 20 seconds each in a region of the chip after mixing at one of the first chambers. Data collection was performed using a Nikon AR1 laser scanning confocal microscope. We then useed Fiji (NIH) for data processing. As shown in **Figure 4.5**, a linear response was observed, and we calculated 3σ LOD of 10 pM for fluorescein detection using the fluorescece lock-in detection method (μChopper).

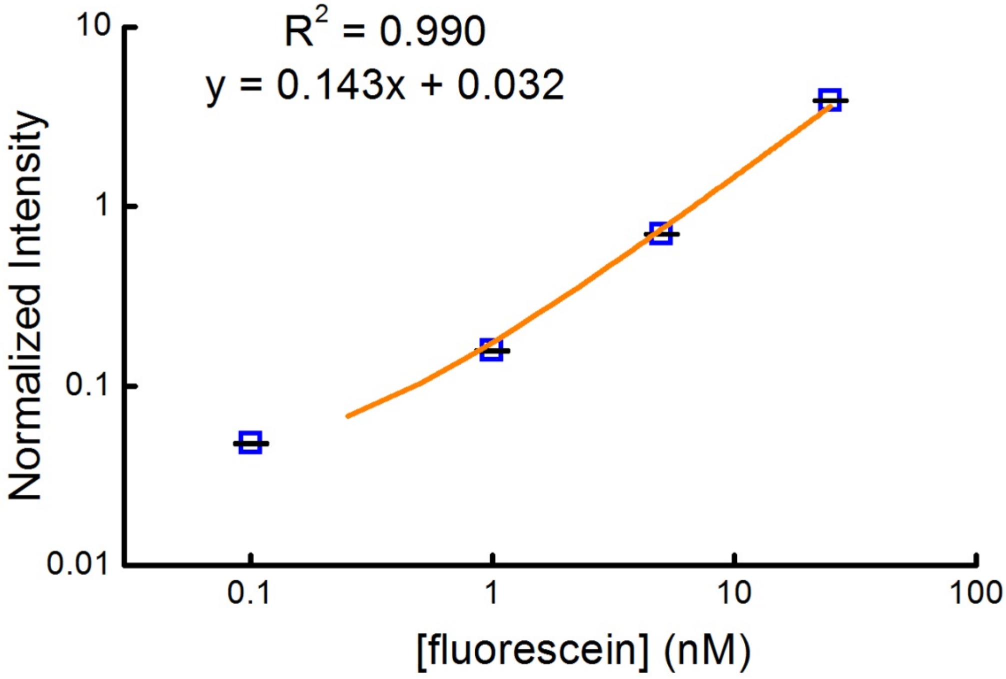

Figure 4.5 Plot of normalized intensity versus various concentrations of fluorescein to obtain a calibration curve. The 3σ LOD for fluorescein detection was calculated to be 10 pM using the fluorescence lock-in detection via the μChopper.

4.3.2: Proximity FRET assay (pFRET)

Proximity FRET (pFRET) is a homogenous protein assay using the target-driven assembly of fluorescenct probes. Two probes to detect insulin were prepared by conjugating two different insulin antibodies (3A6 and 8E2) to two different oligonucleotide tails having a fluorophore (TYE665) and a quencher (BHQ2), respectively. When the solutions are mixed, these two probes recognize insulin, and these oligonucleotide tails are thus in close proximity, promoting hybridization to a 30-base single-stranded DNA connector (C30), resulting in fluorescence quenching (**Figure 4.6).** This effect relies on high binding affinity of target protein and probes in solution, as demonstrated in a previous publication with a similar assay format [20]. Signal is highest at low concentration and decreases as analyte concentration increases. Since this approach provides direct fluorescence-based detection of proteins with high specificity, it is ideal for combination with the fluorescence μChopper described previously. The combined system is particularly useful for secretion sampling from small numbers of cells, where the droplets can act as individual compartments, minimizing dilution of the secreted analyte.

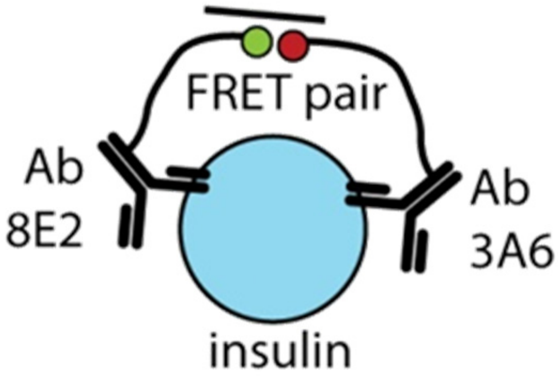

Figure 4.6 Illustration of pFRET assay mechanism, showing antibody-oligonucleotide conjugate probes bound to the target protein (insulin), as well as the FRET pair in close proximity after binding with the connector DNA.

4.3.3: Temporal resolution studies

In moving towards on-chip hormone secretion sampling, one of the biggest challenges lies in optimizing the temporal resolution of the droplet-based fluidic sampling system. As islets are stimulated, secretions usually occur in pulses upon release of insulin from pools of vesicles [4,22]. Ideally, each secreted pulse would be captured by multiple droplets, allowing us to preserve the shape of the pulses as they exit the cells; this result should be achievable with temporal resolution of about 1-3 s. The challenge is to minimize diffusion and laminar dispersion in the islet reservoir and the aqueous channel, and this has been achieved by our group previously in detecting zinc secretions at approximately one-second resolution [4]. However, the pFRET protein assays are more complex than the zinc assay, and they require several minutes of incubation time. This inferred that droplets needed to stay on the chip for several minutes, as opposed to only a few seconds in prior work [4]. Because of this, it was necessary to add an incubation channel, which inevitably degrades temporal resolution. Nonetheless, temporal resolution on the order of 10 s should still be possible, thus we set out to characterize the temporal resolution of our fluidic sampling device (μChopper). This was accomplished through two different methods: a droplet tracking method and a droplet photo-bleaching method. The results from these methods lead us through several different design modifications before we arrived at our current channel layout.

4.3.4: Droplet tracking through image analysis

Droplet tracking was performed by 2 different methods, both relying on imaging a working device with an inverted Nikon Ti-E microscope in transmission mode. Early in the investigation and not shown here, binary images of the droplets were created using ImageJ software. Each droplet was followed and marked in successive images as it flowed through the incubation channel. Plots of the X and Y positions were made of each droplet to determine the flow patterns. Although effective, this analysis method was tedious and time consuming. A more high throughput method of tracking droplets was with an ImageJ software plugin called mTrackJ; this plugin allows a user to point and click on droplets in order to follow and record their position through the channel without the need for manipulation of the images [22]. This tracking is demonstrated by the various colored lines shown in **Figure 4.7.** We were able to track 20 droplets in a channel and monitor the flow rates and flow profiles that occurred. With our initial design, it was observed that droplets travelled at different rates depending on their positions in the channel (**Figure 4.7**, top). In the first design of the incubation channel, as shown in **Figure 4.2b**, interferences were created by interactions with the walls of the channels, slowing down the droplets on the edges while the droplets in the middle of the channel flowed at a much higher speed. The speeds were also highly dependent on the number of droplets in the channel. Unexpectedly, if the droplets did not completely fill the incubation chamber, then the droplets on the edges would flow at much faster rates of speed than the droplets in the middle. This is believed to be caused by the higher flow rate of the carrier oil around the outside edges of the droplets. A more predictable parabolic flow pattern was observed when the channel was full of droplets. These problems occurred during flow in straight channels, but other problems occurred at the turns. When the droplets was forced to negotiate a turn, the droplets on the outer wall of the turn had a much longer distance to travel compared to droplets near the inner wall, resulting in a 'racetrack' effect through each turn. These factors will greatly reduce the temporal resolution of any time dependent study, as droplets in various positions in the channel will experience a multitude of flow rates at different times. Since our application is highly dependent on the temporal resolution of the droplet based sampling system, a new chip design was needed. In the new system, droplets opened into a chamber where they were allowed to flow for a short time period before they were funneled back to a more narrow, single-droplet-width channel connecting to the next chamber [18]. This process was repeated throughout the entire length of the incubation channel, through 50 chambers, then ended at the outlet. Measurements were made at various points in the incubation region, depending on the requirements of the experiment. After tracking droplets through turns and a few chambers, it was shown that the droplets retained much of the ordering in passing from chamber to chamber (**Figure 4.7**, bottom). These results were encouraging, but the method did not allow tracking of droplets through the entirety of the incubation region. This feat was accomplished using droplet photobleaching, as discussed below.

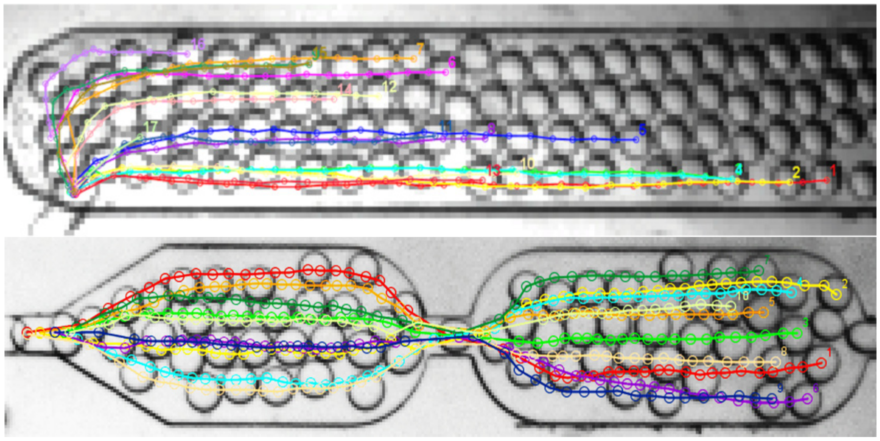

Figure 4.7 Comparison of two incubation channel designs. Long, wide channels greatly hindered the temporal resolution of the droplet based sampling method. Incorporating short, single droplet diameter channels periodically and around turns was shown to greatly improve the temporal resolution by keeping droplet ordering consistent throughout much of the 2-3 minute time frame of incubation. Channels are 470 μm in width.

4.3.5: Photobleaching droplets for tracking purposes

In order to obtain an estimate of our temporal resolution throughout the length of the incubation channel, we developed a photobleaching technique on droplets containing fluorescein. As droplets enter the incubation chamber, our resolution is inevitably decreased by ~5-fold, as this is how many droplets can fit across the width of the chamber. Our main concern was how closely spaced these five droplets would remain throughout the length of the incubation chamber. This will become an important factor when monitoring secretions from living islets, which occur as pulses instead of through a gradual release. Tracking was accomplished by first filling the first few incubation chambers with droplets that contained fluorescein, then stopping the flow and allowing them to stabilize in the chamber. We then used the 488 nm laser at 5.0% power and the 640 nm laser at 3.0 % power on the confocal microscope to bleach a row of droplets in the chamber for approximately 3 minutes, shown in the rightmost images of **Figure 4.8**. After bleaching, flow was reinstated, and the last chamber was monitored for the bleached droplets. It was observed over several trials that the five droplets exited the chip within 2-4 seconds of each other when using the typical vacuum levels applied during normal operation (**Figure 4.9).** These results were very encouraging and showed that the periodic channel restrictions successfully preserved droplet ordering and temporal resolution, even after travelling through all 50 chambers.

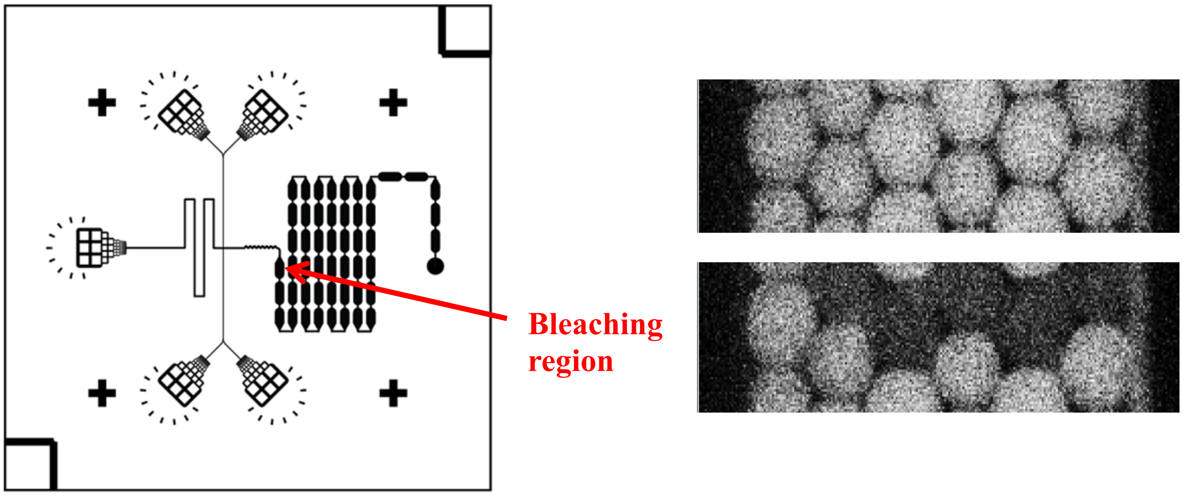

Figure 4.8 The secretion sampling device layout is shown at the left, and the images show the region where the droplets were bleached on the chip. The upper and lower images show the same set of droplets before and after bleaching, respectively. It was then a simple matter to track these five bleached droplets throughout the full length of the incubation chambers.

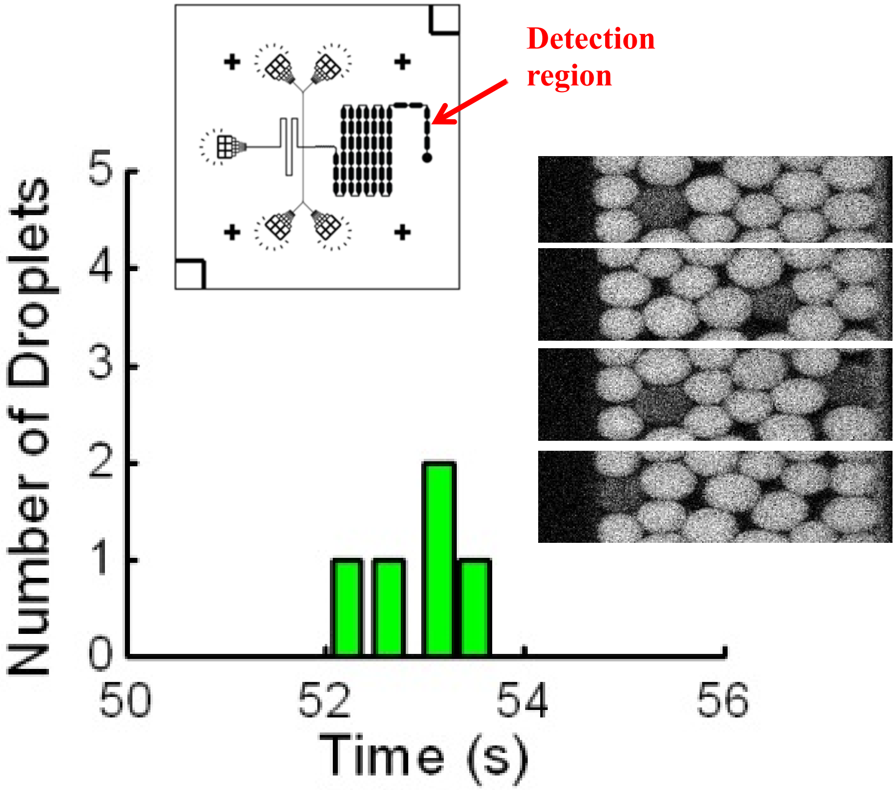

Figure 4.9 Temporal resolution study of the incubation region using photobleaching. The images at the right show all five bleached droplets as they passed through the final chamber at various time points. The plot shows the count of bleached droplets over time. In this run, all five droplets exited the full incubation region within 2 seconds of each another after a one-minute incubation on the chip.

Now that the temporal resolution of the incubation chip was established, some proof of concept experiments needed to be performed, as discussed below. To show this novel micro-analytical system could detect changes in concentration dynamically, we set up changes of concentration of two different proteins, thrombin and insulin, at 20 nM and 25 nM respectively. We also performed islet stimulation on chip with various concentrations of glucose. Again, data analysis is performed with a combination of Elements software and Fiji.

4.3.6: Dynamic detection assays

4.3.6.1: Thrombin and Insulin calibration

Our goal was to apply our fluorescent lock-in method to a dynamic protein detection scenario, in which the concentrations vary over time (e.g. cells secreting hormones). Our first check was simply to use thrombin as our target with either a blank or 20 nM thrombin added to the input reservoir, along with the required thrombin aptamer probes for pFRET, as a proof of concept. A blank was placed in the reservoir and droplets were formed. Flow was stopped and a droplet of the blank was imaged. 20 nM thrombin was added after the reservoir was washed, and the same process was performed. Settings for imaging were maintained for both droplet images. As seen in the droplets in **Figure 4.10,** there was a decrease in fluorescent signal when thrombin was present, providing proof-of-concept that proteins could be detected in picoliter volume droplets. In fact, the system was able to detect the presence of only 2 amol, or 70 fg, of thrombin.

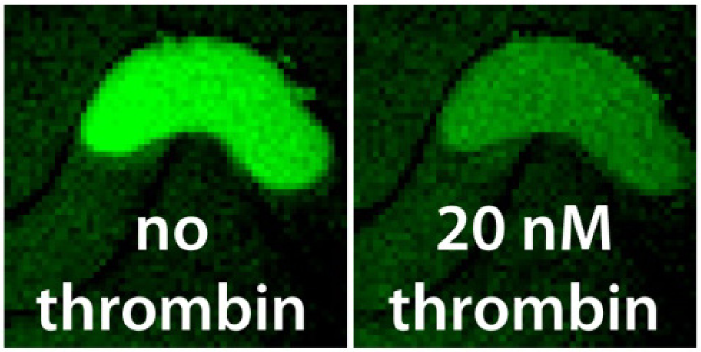

Figure 4.10 Droplets with and without thrombin, using pFRET for detection. On the left, a dropet containing probes and no thrombin showed a higher signal than a droplet containing 20 nM thrombin and probes. Here only 2 amol, or 70 fg, of thrombin was detectable.

We next shifted our focus to insulin detection on-chip; first, using calibration solutions made from stock insulin, then focusing on islets on-chip secreting insulin from stimulations of glucose at various concentrations. As with thrombin, we started with a blank in the reservoir and allowed droplets to form and collected data. Analysis was performed using the typical lock-in detection method of data collection for 20 seconds for 3 runs. Then, insulin at a concentration of 25 nM was added to the reservoir, droplets were formed and again, data was collected in triplicate. After data collection, sample and reference data was analyzed and the quenching ratio for all runs was compared. As expected, in the presence of insulin, the fluorescence signal decreased, easily allowing detection of 25 nM concentration of target (**Figure 4.11).**

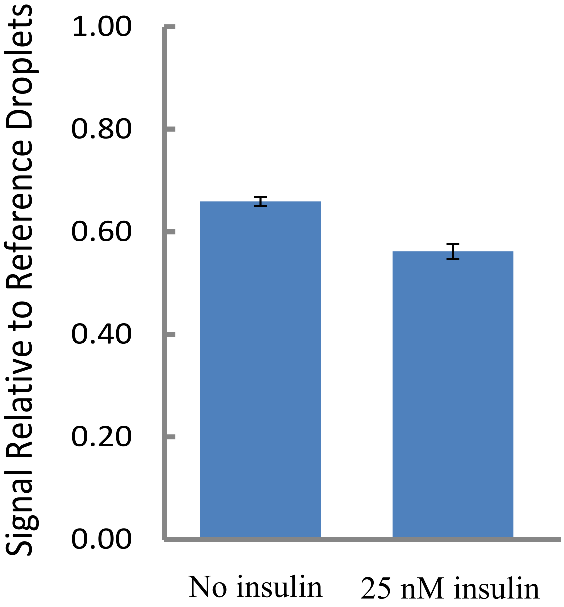

Figure 4.11 Relative intensity of signal to reference droplets with no insulin and with insulin in the presence of probes. As expected, the intensity is lower when 25 nM insulin was present in the droplets.

Now that our probes were capable of detecting target proteins within droplets, calibration curves for various concentrations of insulin standards were made. This was performed on-chip with a reference consisting of pFRET antibody A and B, fluorescein, bovine serum albumin (BSA), cascade blue, NaCl, Tris-HCl and $MgCl_2$; the reference channel only had one input, termed reservoir 'C'. The sampling reservoirs are termed 'A' and 'B', containing probes and insulin standards (in place of islets), respectively. 'A' reservoir contained the assay mixture: pFRET antibody A and B, fluorescein, BSA, NaCl, Tris-HCl and $MgCl_2$. 'B' reservoir contained the insulin standards (will contain islets later). As 'A' and 'B' solutions mix and the target is recognized, fluorescence signal is quenched in proportion to the amount of insulin. Several concentrations of insulin standards were used. Runs typically lasted 20 seconds and were repeated in triplicate. Data collection was performed at the end of the chip, and a calibration curve was generated through data analysis, as previously described (**Figure 4.12).**

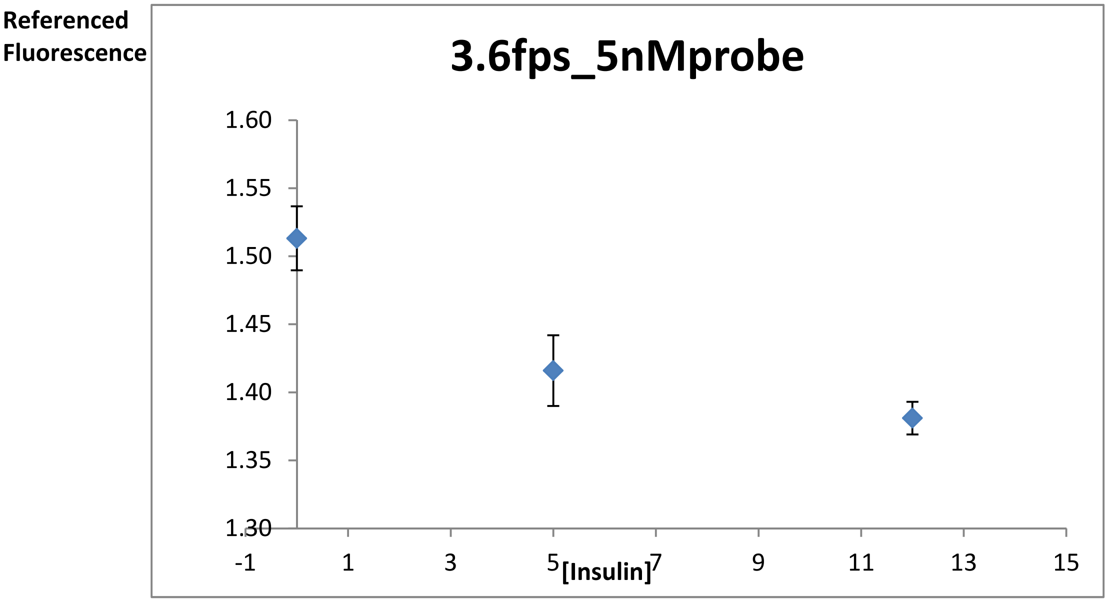

Figure 4.12 A calibration curve showing the referenced fluorescence intensity of droplets with three different concentrations of insulin. As expected, signal decreases with a higher concentration of insulin, and the assay responded to low nanomolar concentrations.

Although the results are promising, there are certainly more experiments to perform. The assay is very sensitive to the probe concentration, which should be tuned to the amount being secreted. For many of the preliminary runs, we were using various probe concentrations as well as varying our data analysis techniques. As shown below, even though we do show that fluorescent signal decreases with increasing insulin secretion, the calibration curve conditions were not well-matched with the islet sampling conditions, thus we have yet to obtain quantitative secretion sampling data

.

4.3.6.2: Islet secretion sampling

Although the calibration was not yet optimized, it was decided to go through a test run of monitoring glucose-stimulated insulin secretion from living islets using our novel fluorescence based μChopper. 15 murine pancreatic islets were loaded into reservoir ‘B’ on the chip with all required buffers, the probe solutions were loaded into reservoir ‘A’, and reference solutions were loaded into in the opposing aqueous channel fed by reservoir ‘C’. The oil reservoir was filled, and vacuum was applied to begin droplet formation. Once droplets were stable, data was collected at the last incubation chamber to monitor the islets’ secretions in the presence of 3 mM glucose for ~5 minutes. Once this baseline was established, 11 mM glucose was spiked into the reservoir, and the data was collected for 20 minutes before spiking the reservoir with diazoxide to inhibit insulin secretion. Data was collected for an additional 5 minutes. Analysis was performed by comparing sample and reference signal throughout the entire run. For the following runs, the sample is now identified as a red fluorescent signal labeled with TYE665 with a green fluorescent signal from the FAM labeled reference. While the reference signal remained relatively flat, the sample signal changed significantly over the 30 minute period.

Once the 11 mM glucose was added, an increase in quenching was observed (decrease in signal, **Figure 4.13**), and a prolonged 'pulse' of insulin appeared to be secreted by the 15 islets. When diazoxide was added to the reservoir, this pulse was attenuated. Although the signal continued to decrease (inferring quenching), the overall response pattern (compared to the stable baseline) was encouraging, indicating that insulin was changing in response to glucose and in response to pharmacological stimulation (**Figure 4.13).** This represents the first instance of hormone secretion sampling and direct fluorescence quantitation from living cells using a microfluidic droplet-generating device. Though further work is warranted, the results are highly encouraging for future application of the μChopper to sampling and quantitation of secreted hormones from small amounts of endocrine tissue.

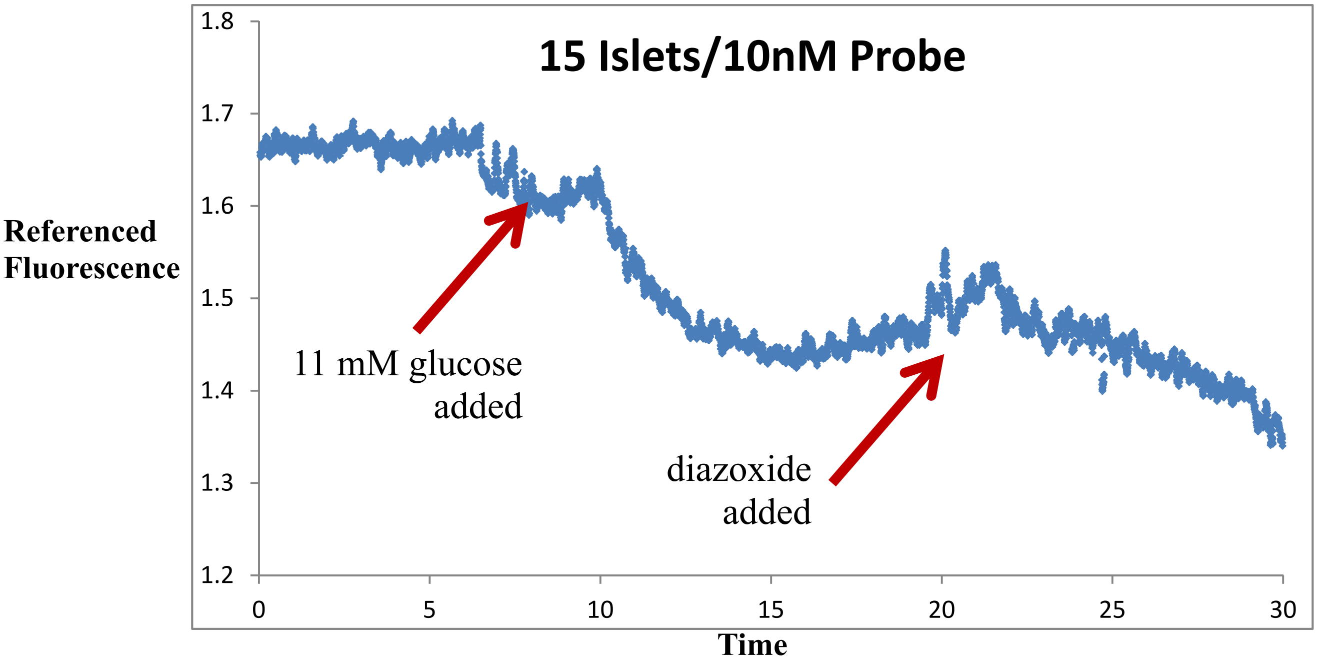

Figure 4.13 15 islets were monitored on-chip by the μChopper for stimulated secretion sampling over a 30 minute time period. A baseline was established with 3 mM glucose, then 11 mM glucose was added. Referenced signal decreased as more insulin was being secreted by the stimulated islets. After addition of diazoxide, the islets responded by a decrease in insulin secretion followed by a consistent, prolonged increase in secretion. This proof-of-concept experiment shows that the μChopper can detect islets' responses to stimuli and lays the foundation for future applications in endocrine sampling and quantitation of hormones at high temporal resolution.

4.4: Conclusions

We have designed a microfluidic device (µChopper) capable of cell secretion sampling, probe mixing, assay incubation, and direct readout fluorescence-based detection for homogenous protein assays. Incubation region design was fine-tuned toward optimal temporal resolution, and preliminary calibrations with insulin showed low nanomolar detection limits. Although more work is necessary, we have qualitatively shown insulin secretion sampling from pancreatic islets with droplet microfluidics on-chip after stimulation with glucose and pharmacological agents. Future work includes generation of thorough calibration curves under the same conditions as secretion sampling. This will require a more optimal design for consistent one-to-one mixing of pFRET probes and secreted hormones, as well as an increased incubation time for higher assay sensitivity.

4.5: References

1. Kovarik, M. L.; Ornoff, D. M.; Melvin, A. T.; Dobes, N. C.; Wang, Y.; Dickinson, A. J.;
2. Gach, P. C.;Shah, P. K.; Allbritton, N. L. *Anal. Chem.* **2013**, *85* 451–472.
3. Guo, M. T.; Rotem, A.; Heyman, J. A.; Weitz, D. A. *Lab Chip,* **2012,** 2146-2155.
4. Easley, C. J., Rocheleau, J. J.; Head, W. S.; Piston, D. W. *Anal. Chem.*, **2009,** *81*, 9086–9095.
5. Buranda, T.; Huang, J.; Perez-Luna, V. H.; Schreyer, B.; Sklar, L. A.; Lopez, G. P. *Anal. Chem.* **2002,** 74, 1149-1156.
6. Mangru, S.; Bentz, B. L.; Davis, T. J.; Desai, N.; Stabile, P. J.; Schmidt, J. J.; Millard, C. B.; Bavari, S.; Kodukula, K. *J. Biomol. Screen* **2005,** 10, 788-794.
7. Jung, J.; Chen, L.; Lee, S.; Kim, S.; Seong, G. H.; Choo, J.; Lee, E. K.; Oh, C.; Lee, S. *Anal. Bioanal. Chem.* **2007,** 387, 2609-2615.
8. Srisa-Art, M.; deMello, A. J.; Edel, J. B. *Anal. Chem.* **2007,** 79, 6682-6689.
9. Li. Y.; Xu, Y.; Feng, X.; Liu, B. *Anal. Chem.* **2012,** 84, 9025-9032.
10. Song, H.; Ismagilov, R. F. *J. Am. Chem. Soc.* **2003,** 125, 14613-14619.
11. Solvas, X. C.; Srisa-Art, M.; deMello, A. J.; Edel, J. B. *Anal. Chem.* **2010,** 82, 3950-3956.
12. Wang, S.; Huang, X.; Yang, C. *Lab Chip*, **2011,** 11, 2081-2087.
13. Egawa, T.; Durand, J. L.; Hayden, E. Y.; Rousseau, D. L.; Yeh, S. *Anal. Chem.* **2009,** 81, 1622-1627.
14. Kane, A. S.; Hoffmann, A.; Baumgärtel, P.; Seckler, R.; Reichardt, G.; Horsley, D. A.; Schuler, B.; Bakajin, O. *Anal. Chem.* **2008,** 80, 9534-9541.

15. DeJournette, C. J.; Kim, J.; Medlen, H.; Li, X.; Vincent, L. J.; Easley, C. J. *Anal. Chem.* **2013,** DOI: 10.1021/ac4026048.

16. Duffy, D. C.; McDonald, J. C.; Schueller, O. J. A.; Whitesides, G. M. *Anal. Chem.* **1998,** 70, 4974-4984.

17. Holtze, C. Rowat, A. C.; Agresti, J. J.; Hutchison, J. B.; Angilè, F. E.; Schmitz, C. H. J.; Köster, S.; Duan, H.; Humphry, K. J.; Scanga, R. A.; Johnson, J. S.; Pisignano, D.; Weitz, D. A. *Lab Chip,* **2008,** 8, 1632-1639.

18. Miller, O. J.; Harrack, A. E.; Mangeat, T.; Baret, J. C.; Frenz, L.; Debs, B. E.; Mayot, E.; Samuels, M. L.; Rooney, E. K.; Dieu, P.; Galvan, M.; Link, D. R.; Griffiths, A. D. *Proc. Natl. Acad. Sci USA,* **2012,** 109, 378-383.

19. Deal, K. S.; Easley, CJ. *Anal. Chem.;* **2012,** 84, 1510-1516.

20. Heyduk, T. *Biophys. Chem.* **2010,** 151, 91-95.

21. Baret, J. *Lab Chip* **2012,** 12, 422-433.

22. Roper. M. G.; Shackman, J. G.; Dahlgren, G. M.; Kennedy, R. T. *Anal. Chem.* **2003,** 75, 4711-4717.

23. Erik Meijering Research Home Page. http://www.imagescience.org/meijering/software/mtrackj/ (accessed Mar 29, 2012).

Chapter 5: Toward Feedback Control of Droplet Formation

5.1: Introduction to devices

The overall goal for the work in this chapter was to create a chip with more precise control of droplet formation, manipulation, and detection. The frequency, size, and flow rate of each phase needed to be detected in some way in order to make this feasible. This data could then be used to control an on chip variable resistor through LabVIEW to adjust to desired parameters. In order to fabricate valves on-chip, many different design strategies were employed, including partial curing, using magnetic pins, and performing multilayer chip fabrication. Along with fabricating the chips, a robust detection method had to be established in order to detect the droplets in each system. Several droplet detection schemes were tested as well, including on-chip waveguides using the microscope camera and software or PMT-based detection making use of a LabVIEW program.

5.1.1: Soft lithography channel characteristics

In order to control the resistance of these channels, the idea was always to apply a pressure to the top of the channel to reduce the cross-sectional area and control the fluid flow in that manner, creating a variable fluidic resistor (**Figure 5.1).** It was thought that a complete blockage of the phase, be it aqueous or oil, would be very difficult because of the channel shapes. Because of the nature of the SU-8 photoresist, there would always be straight walls intersecting with a flat surface, i.e. corners that could not be completely blocked by a deflected membrane, preventing complete blockage of flow. In order to correct for this, a method was developed to curve the corners of the channels. PDMS was poured over the silicon master and allowed to cure. After it was removed, more uncured PDMS was mixed at a ratio of 10:1, the air was removed, and then a small amount was applied to the channeled side of the chip. A flat surface, usually a razor blade, was used to spread the PDMS over and into the channels in all directions. The chip was then placed in the spin coater at 3500 RPM for approximately three minutes. After the device was again cured in the oven at 65 °C, the result was curved corners (**Figure 5.2).** This approach presents one option to allow more complete valving of channels. In our later designs, the curved corners were not absolutely required, as the valve region covered a significantly larger portion of the resistor, yet this approach should find use in future device fabrication.

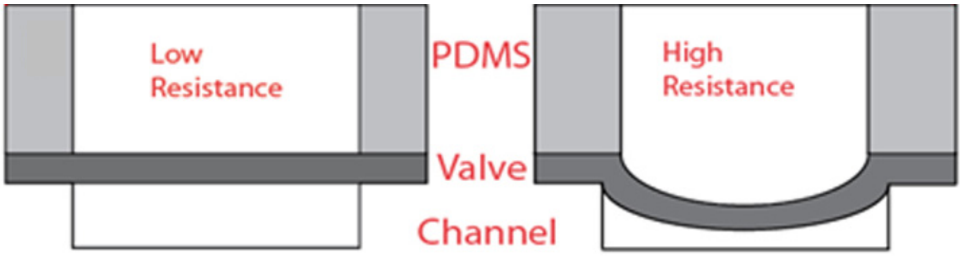

Figure 5.1 Illustration showing the deflection of the thin membrane of a variable resistor as pressure is applied.

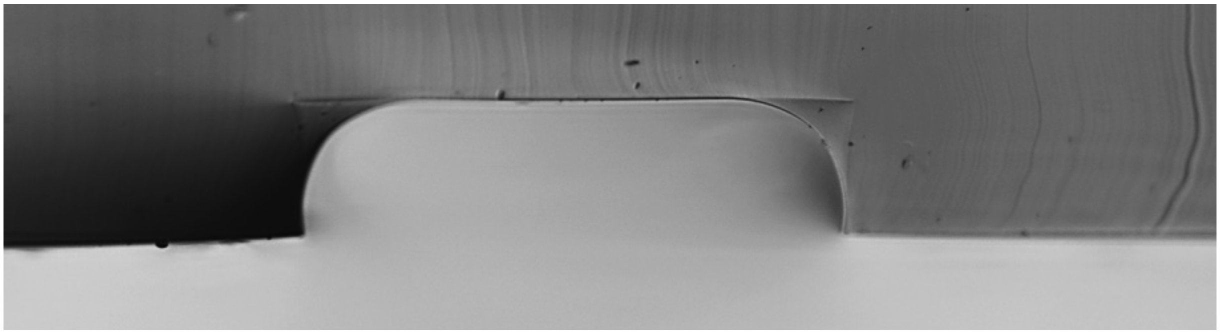

Figure 5.2 Image showing the curved portion of the channel created after PDMS spin coating modification of channeled surfaces. These curves should allow complete sealing of channels with deflected membranes in the future.

5.1.2: Multilayer valves: Partial curing of PDMS

The first attempt at making variable resistor valves involved using a partial curing method to bond two pieces of PDMS together in order to make a valving section on the chip. A thin layer of uncured PDMS was spin coated over the SU-8/silicon wafer master, then cured. Cylindrical plastic inserts of ~1-mm diameter and 1 cm tall were molded from Smooth-On, a fast curing white epoxy used by special effects artists in the movie-making industry. The next layer was poured over the thin layer of PDMS in order to completely cover up the inserts being used to form the valves. These inserts were placed over certain regions of the fluidic resistor portions of the chips, just after pouring the second layer of PDMS. Both layers were placed in the oven and allowed to cure at 65 °C for a few hours. Once cured, the inserts were removed, and the chip and thin layer portion were removed from the wafer. A third layer of PDMS was then used to cover the voids from the inserts. A small hole was punched in the PDMS, then bonded to the top of the chip either through plasma oxidation or partial curing. As is evident, this method is rather time consuming and tedious with a lot of chances for errors to occur. Inserts had a tendency to move around and shift during curing. Most often, a chip would fail because the top layer would not seal efficiently enough to be air tight. As soon as any pressure was applied to the valves, the chip would fail and become inoperable. An improved method was thus developed in order to simplify the fabrication process.

5.1.3: Valve fabrication using magnetic pins

In lieu of plastic inserts (which tended to drift), 1-mm diameter magnetic pins were used to create the valves over the resistor region of the chip. Again, a thin layer of PDMS was spin coated over the device and allowed to cure. Two magnetic pins were used, one above and one below the wafer, to create the valve on the chip. PDMS was poured over the chip and was allowed to cure, and these pins were very stable in their intended positions. After curing, the pins were removed. Since the magnetic pins and the tubing were about the same size, tubing was simply pressed into the PDMS forming an air tight seal (**Figure 5.3).** The pins were also small enough that more than one resistor valve could be created on each chip. That being said, it was difficult to place two or more resistors in close proximity, as they tended to become attracted to one another and move away from the selected regions. Nonetheless, the single-valve method was reproducible enough to create several different chips with one or more functional resistors on them. The results discussed below were obtained from chips fabricated through this method, thus its application will be discussed in the following section.

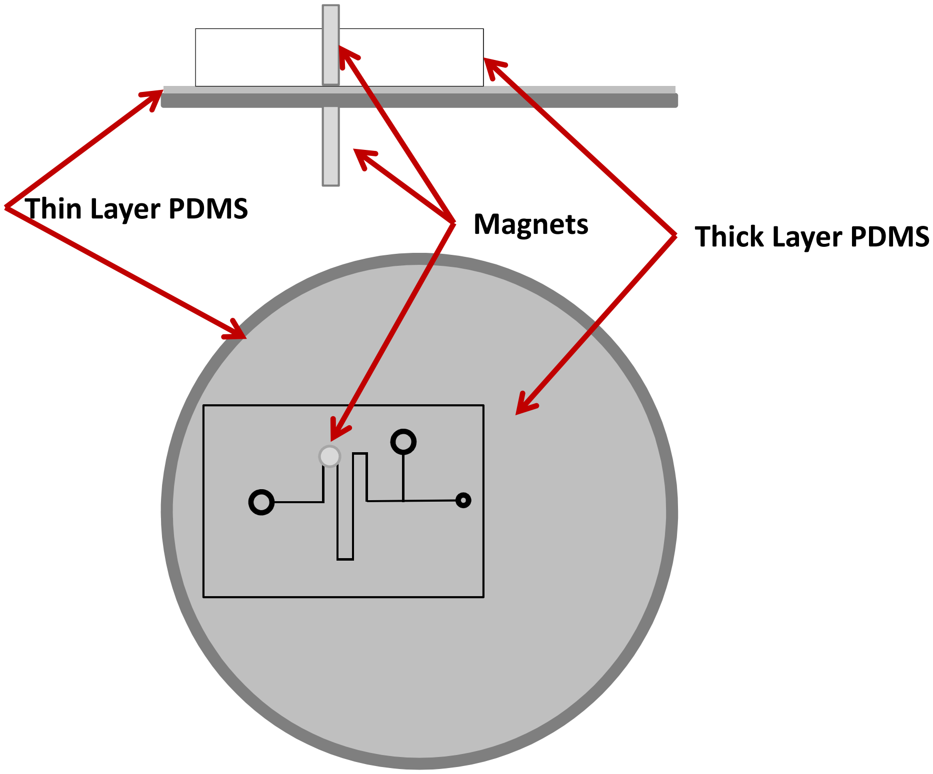

Figure 5.3 Illustration showing how magnetic pins were used to create variable resistors in the oil channels.

5.1.3.1: Dynamic fluidic resistance with a variable resistor

In combination with conductivity based approaches to fluidic resistance measurements that provide direct voltage readouts, a chip was designed with a variable resistor on the carrier oil channel. This set-up allows direct measurement of fluidic resistance on a microfluidic device by interfacing with a digital data acquisition system (DAQ, NI) capable of monitoring dynamic values [1,2]. The variability of the resistance is created by a portion of the rectangular channel that has a deformable ceiling controlled by pressure on the oil fluidic resistor. This valve is not considered digital, however because the geometry of the channel allows slight leakage. Applying pressure to the ceiling of the valve causes the membrane to curve into the channel, decreasing the cross-sectional area, and increasing the fluidic resistance ($R_{fluidic}$) **(Figure 5.4).** This system combines a variable resistor controlled by pressure with a fluidic resistance measurement device using conductivity to obtain electrical resistance. Data for each measurement is collected using a DAQ device, which collects data from the pressure sensors (Honeywell) to obtain the pressure applied to the variable resistor and the voltage drop from the fluidic resistance device which is across a series resistor with conductivity standards filling the channels. Voltages were measured across 2 reservoirs. The traces shown validate that the electric resistance waveform (red) closely mimicked the input waveform of the pressure membrane (blue). Two separate waveforms were used and these are shown: sawtooth and square waves, with the resistance trace following both patterns (**Figure 5.5).** This ability to dynamically monitor fluidic resistance is advantageous by demonstrating the ability to measure conductivity in more complex devices.

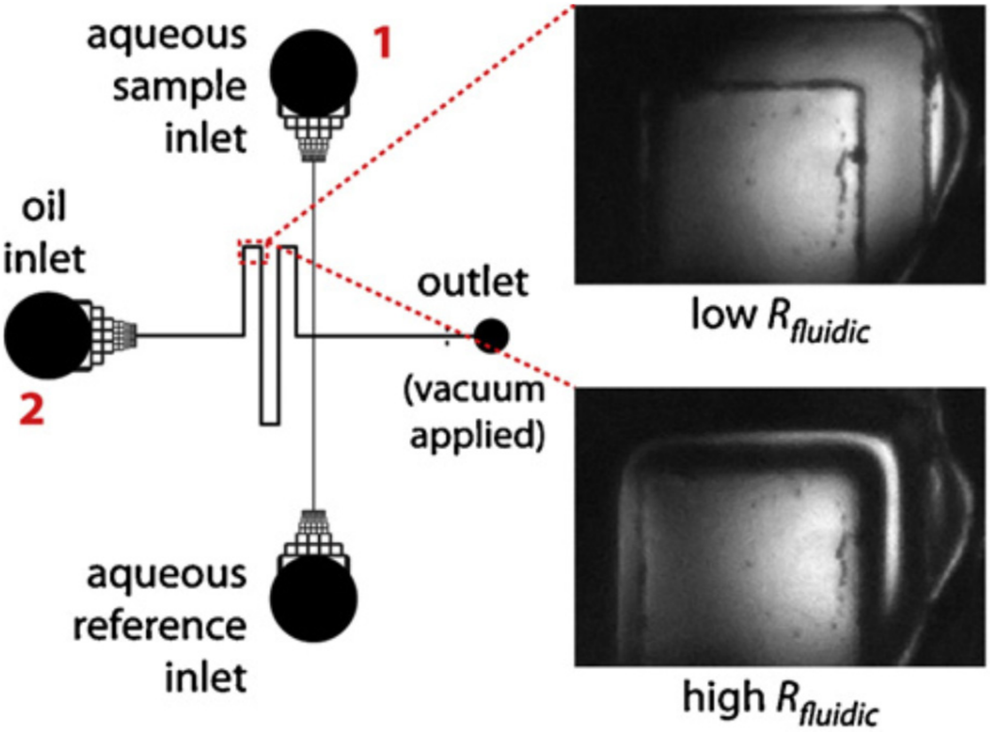

Figure 5.4 Channel layout of droplet generating microfluidic device. The inset images show the variable resistor region at low R_{fluidic} (upper image) and high R_{fluidic} (lower image) after pressure is applied.

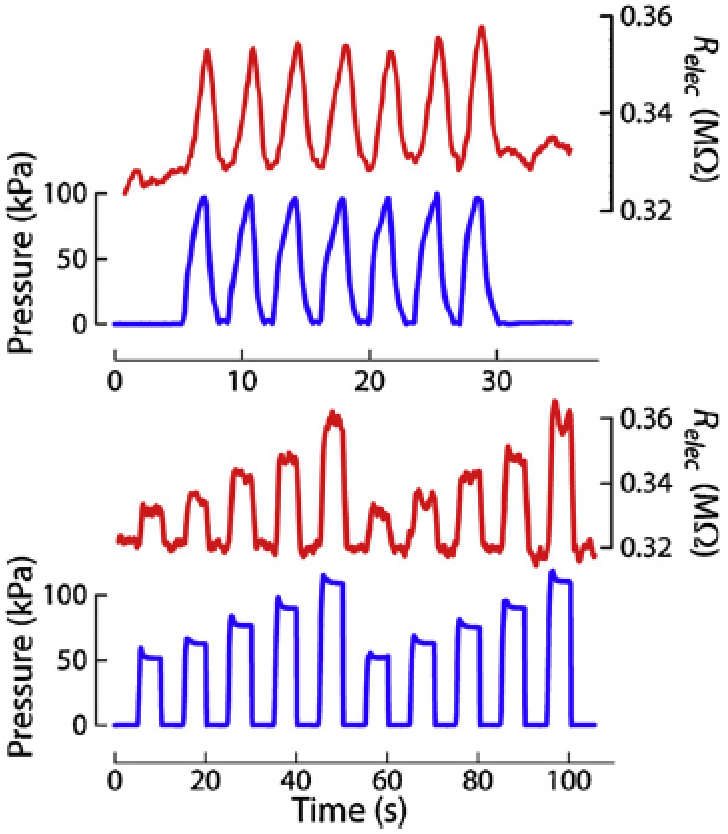

Figure 5.5 Traces showing how the electrical resistance (red trace) matches with the applied pressure (blue trace) on the variable fluidic resistor. This data shows the proof-of-concept of our variable fluidic resistors.

5.1.3.2: Variable fluidic resistors for control of droplet formation

In our variable fluidic resistors, electrical resistance varied linearly with respect to pressure, suggesting a similar trend for the fluidic resistance [2]. From this observation, the droplet generator was used for confirmation by allowing the variable resistor to control droplet formation. With the variable resistor, the fluidic resistances of input channels for oil and aqueous solutions were easily varied depending on the pressure applied to the membrane above the channels. The oil segment volume could be changed by 6 fold or more from 6.61 to 1.07 nL, and the aqueous segment volume was varied by approximately 2.5 fold from 0.71 to 1.75 nL. This allowed a change of the aqueous to oil segment volume ratio of more than 16-fold from 0.10 to 1.64 by simply applying pressure to the variable resistors. The size of the droplets could be greatly increased by changing the resistance in the oil channel through the variable resistor (**Figure 5.6).** The simplicity of operation and ability to tune to a wide range of segmented volumes could allow this novel type of dynamic control system to have major implications on future microfluidic systems for droplet generation.

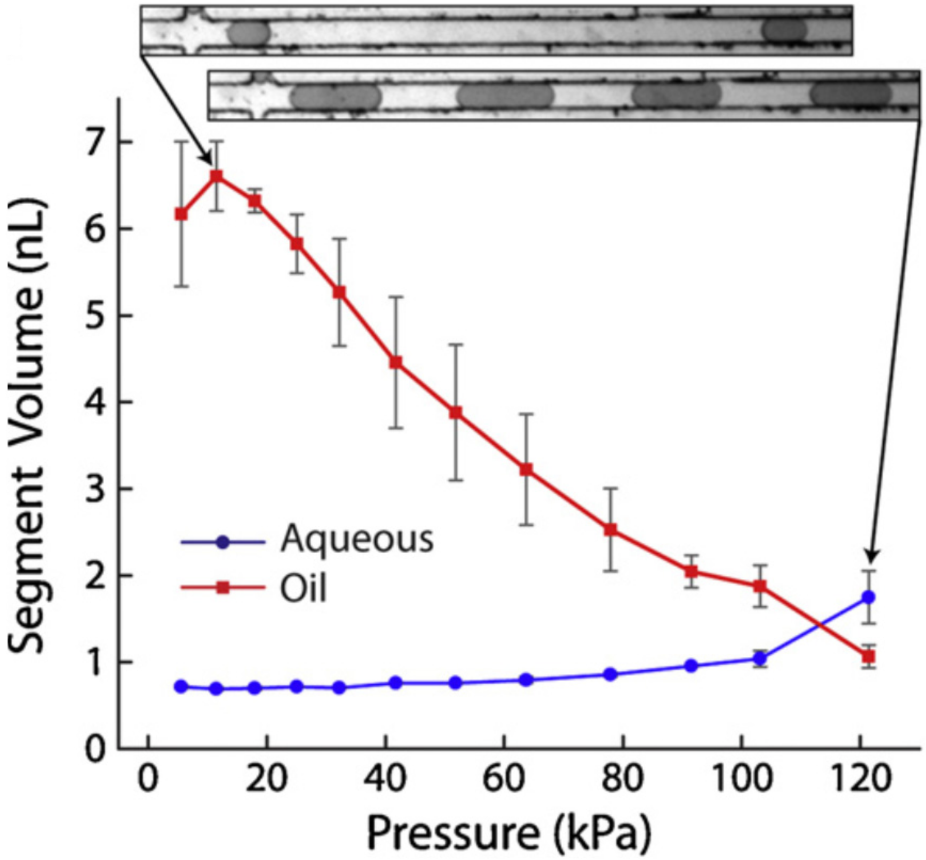

Figure 5.6 Plot of segment volume of the oil and aqueous phases over a range of pressures applied to the variable resistor. Increasing pressure resulted in increased aqueous droplet volume and decreased oil segment volume between droplets, providing dynamic control of droplet size and spacing. Inset images show examples of droplet sizes and spacing.

5.1.3.3: Multilayer soft lithography for improved fluidic resistors

The device used for this research is fabricated in a multi-step process that generates multiple layers of PDMS. The valve portion of the chip was fabricated first in a 10:1 elastomer to curing agent ratio. It was mixed, then degassed, then poured over the valve layer master and cured for approximately one hour and 30 minutes at 65^{o} C. While this layer was curing in the oven, the lower layer consisting of the channels and resistors was vapor deposited with chlorotrimethylsilane for 30 minutes. PDMS was mixed in a 15:1 ratio so that when placed into contact with the other PDMS, more crosslinking is available to form a bond between the two layers. After the mixture was stirred, it was degassed, then poured onto the wafer, which is mounted in a spin coater. The wafer was spun at 1300 RPM for 40 seconds before being placed in the oven for approximately 20 minutes at 65^{o} C. After this period of time, the valve layer was cured just enough to work with, and the channel layer was no longer fluid, but it was still a bit tacky. The valve layer was then cut out and placed onto the channel layer, being careful to line up the valves with the resistors. Once alignment was obtained, the chip was placed in the oven overnight to allow the 2 layers to bond. The next day, the wafer was removed from the oven, and a scalpel was used to score around the edge of the chips to cut the thin layer of PDMS from the silicon wafer. One corner of the chip was lifted slowly, removing it and the thin bottom layer of PDMS with it until the entire chip was free. Holes were then punched for the reservoirs as well as for the vacuum hose attachments. The chip was then cleaned with methanol and dried with air before being plasma oxidized to a glass slide. In order to maintain the pressure applied to the resistor, each valve was filled with water by placing the chip in a vacuum water bath overnight. The following day, all valve control tubing was attached to the chip after being filled with water, and inserted while the chip remains submerged. Images of the various layers and the final combined chip are shown in **Figure 5.7.** A cross section of the device with channel and valve dimensions is shown in **Figure 5.8.**

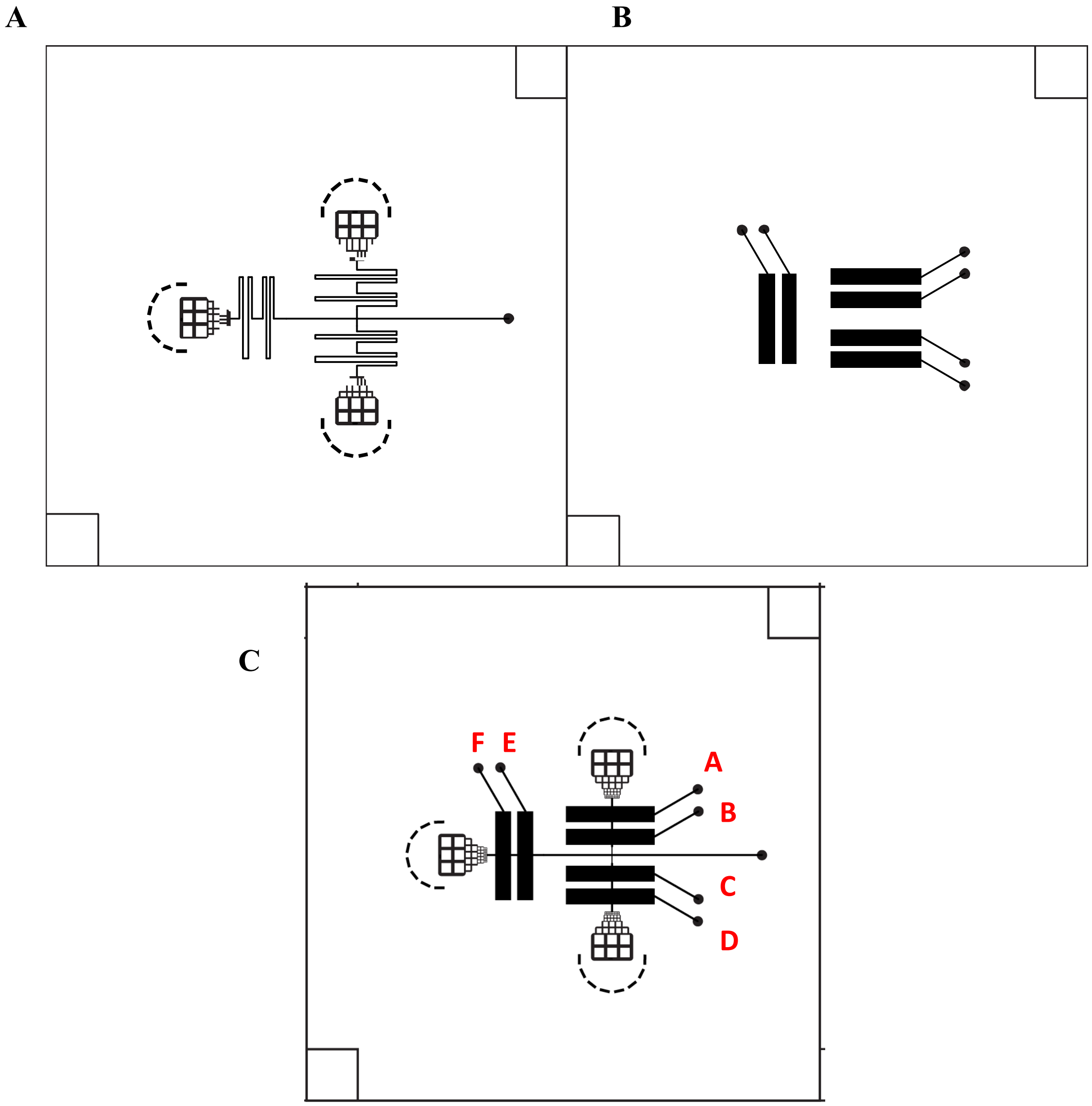

Figure 5.7 Designs for the multilayer variable resistor chip. **A**) Design containing the fluidic channels with resistors that are ~25 µm in height. **B**) Design containing the valves for the resistors, which were ~ 60 µm in height. **C**) A and B designs overlaid to show design alignment upon completion.

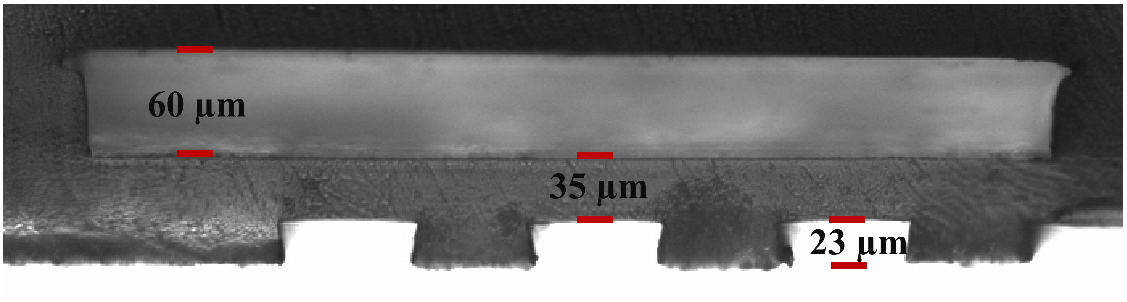

Figure 5.8 Cross section of the variable resistor valve showing the various dimensions. To increase the resistance of the lower fluidic channels, the upper layer was pressurized, pressing the 35 μm membrane down and decreasing the cross-sectional area of the channels.

Data collection was performed in the following manner. In order to calculate the vacuum and pressure applied to the chip and valves, the barometric pressure was noted at the beginning of the run. All syringes connected to the valves were filled with water to the same level and were set to the same starting point to ease the experimental set-up and time. For this instance, all syringes were started at the 20 mL mark. Valves were labeled from A-F. Valves A,B and C,D were the aqueous resistor valves while E,F are the oil channel valves. Several runs were performed for each valve. A vacuum pressure of 9.34 kPa was applied to the fluidic outlet channel to start droplet formation. Then, starting at 20 mL on the valve syringes, a 3 second baseline flow is established and imaged by microscopy, then pressures were applied to various valves. This was done for a range of valve pressures—starting at the 20 mL mark and moving to 19-16 mL marks for valves A-F. Resistor valves were actuated individually, as well as in pairs for varying combinations. Using the barometric pressure from each day's runs, the pressure applied to valves was calculated to range from 4 – 33 kPa. Even at these relatively low applied pressures, it was possible to change the droplet formation patterns drastically for each aqueous channel, and we were even able to stop the oil flow completely. **Figure 5.9** illustrates results from just a few of the variable resistor pressure combinations that were possible. The data shows that our unique approach in controlling droplet formation with variable resistors is capable of manipulating droplet sizes and frequencies over a wide range, and the technique should be highly useful for secretion sampling applications in the Easley lab in the future.

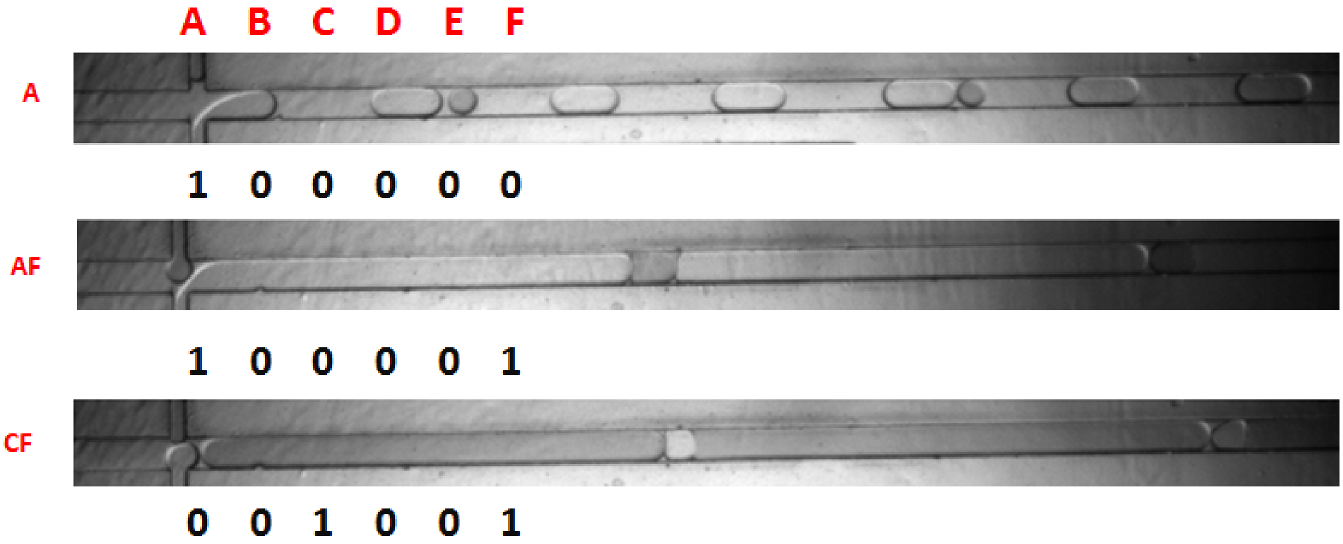

Figure 5.9 Variable resistors for control of droplet formation. These images illustrate the effects of pressure being applied to different variable resistors (A-F). This novel approach provided exquisite control over droplet size and frequency from multiple aqueous inlets.

5.2: Droplet detection methods

5.2.1: On-chip fluidic waveguides

5.2.1.1: Fluidic waveguide design and fabrication

As described earlier, droplet detection is an important component in developing a feedback control based droplet generator. Our results above showed that droplet formation can be precisely controlled by variable fluidic resistors, but we still need a real-time approach for monitoring these values; microscopy and image analysis is too computationally intensive for this purpose. A chip was designed to allow for droplet detection to be performed using on-chip waveguides, as presented recently by the Huang group [1]. The chip consisted of two aqueous channel and an oil channel, as usual for droplet formation. Downstream from the droplet formation region were two curved channels that serve as optical waveguides. The waveguide channels are in close proximity and are perpendicular to the droplet channel, but they do not intersect with it. When filled with oil of high refractive index (lens immersion oil), these channels can be used as excitation and emission waveguide channels [1], which we applied to droplet detection (**Figure 5.10).** A laser was placed up against the edge of the chip in line with the input waveguide channel. Based on Huang's work, the edges of the chip were made more optically clear by applying a small amount of uncured PDMS to the side of the chip and curing against a flat silicon wafer [1] (**Figure 5.11).**

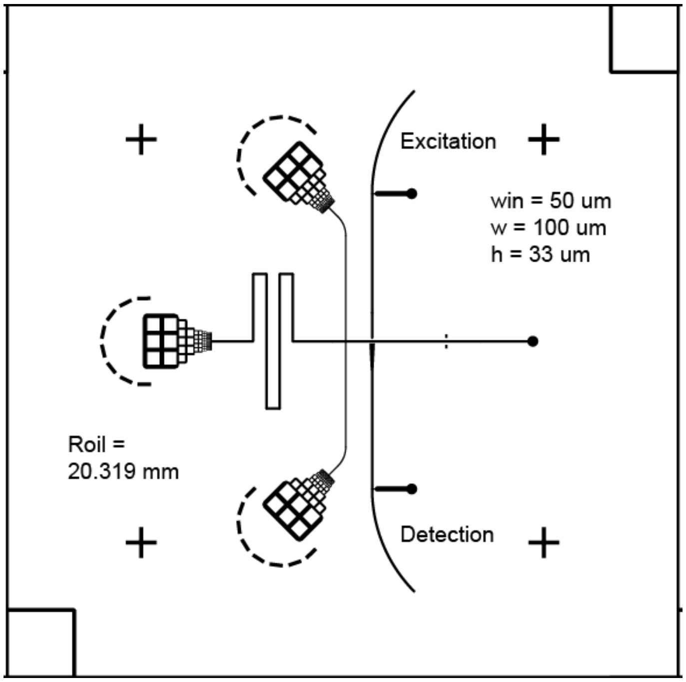

Figure 5.10 Droplet detection chip using waveguides to direct laser light through a flowing droplet train and to a detector.

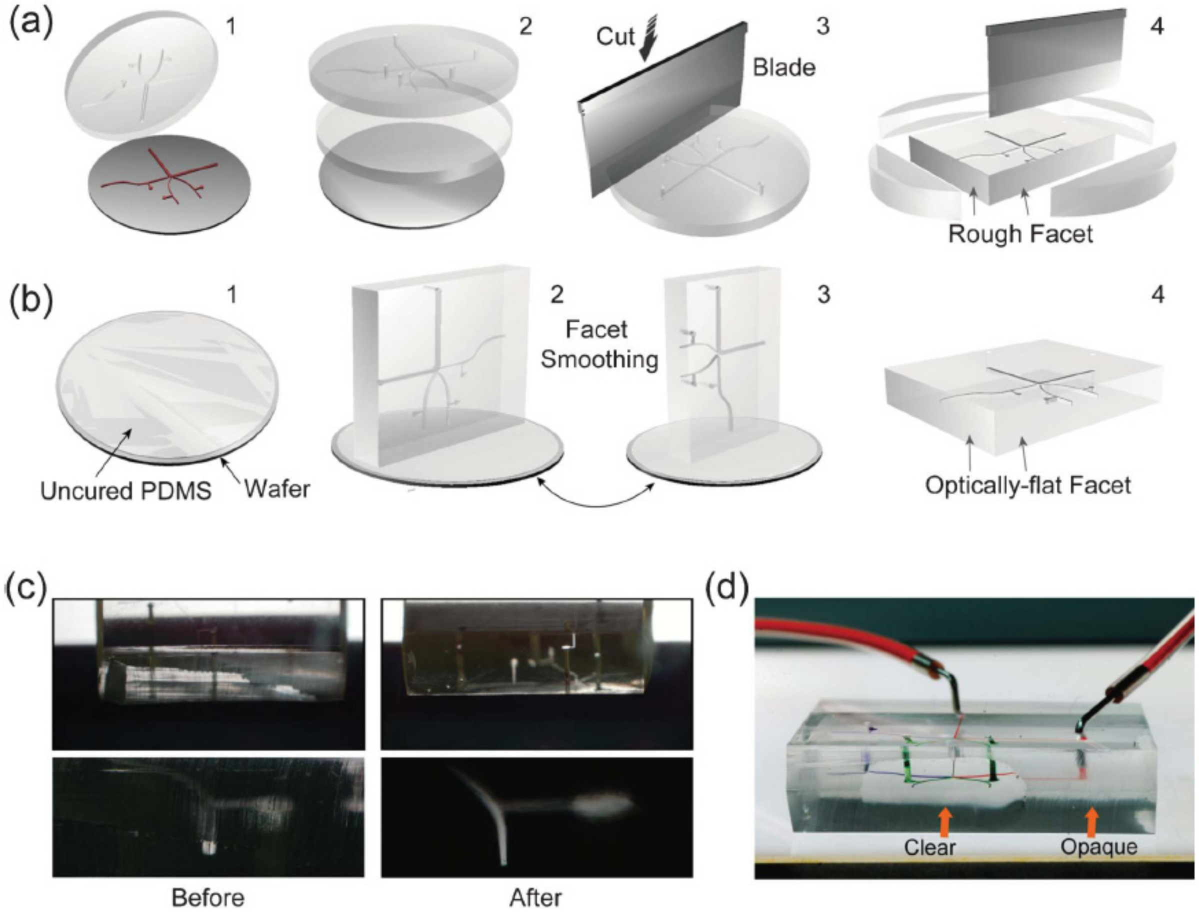

Figure 5.11 This figure demonstrates a creative method to make sliced edges of PDMS optically clear, removing razor blade striations. b) The edge of the chip is placed on a wafer containing uncured PDMS and allowed to cure. c, d) Once cured, the chip is removed from the wafer and the PDMS is smooth and optically transparent. Adapted from Ref. 1 with permission from The Royal Society of Chemistry.

5.2.1.2: Waveguide-based detection of droplets

First, droplet detection with a photodiode was attempted by monitoring the output using LabVIEW. Unfortunately, the change in voltage was not enough to detect, so a different method was used. The chip was placed perpendicularly onto the top of the Nikon Ti-E microscope with the emission channel aligned over the objective. A laser was aligned through the excitation waveguide channel while the chip was adjusted for optimal light signal (**Figure 5.12).** Droplet formation was begun, and video of the end of the detection waveguide channel was taken from the objective, focused through the optically transparent side of the PDMS device. The video was analyzed using the Nikon software by placing a region of interest over the collected video and monitoring the signal. As droplets passed by, decreases in transmitted laser light signal were observed (**Figure 5.13).** These results show that on-chip, channel-based waveguides can be useful for droplet detection, and future work includes incorporation of this type of detecting into feedback control systems, along with the variable resistors for droplet control.

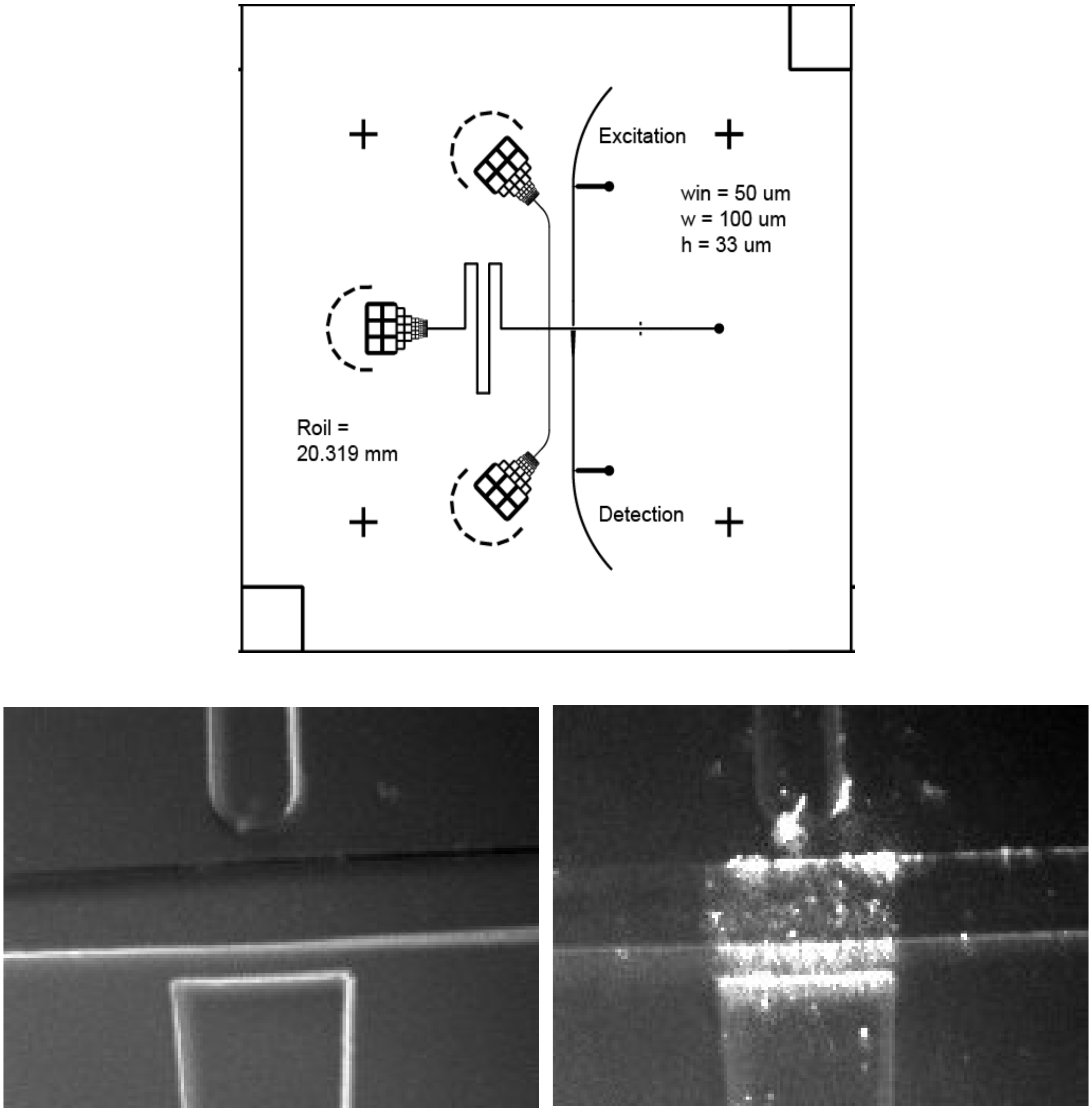

Figure 5.12 Images showign the waveguide channels (upper and lower) perpendicular to the droplet outlet channel (left to right). Images are shown with the laser off (left image) and on (right image), showing that the laser passes directly through the droplet outlet channel.

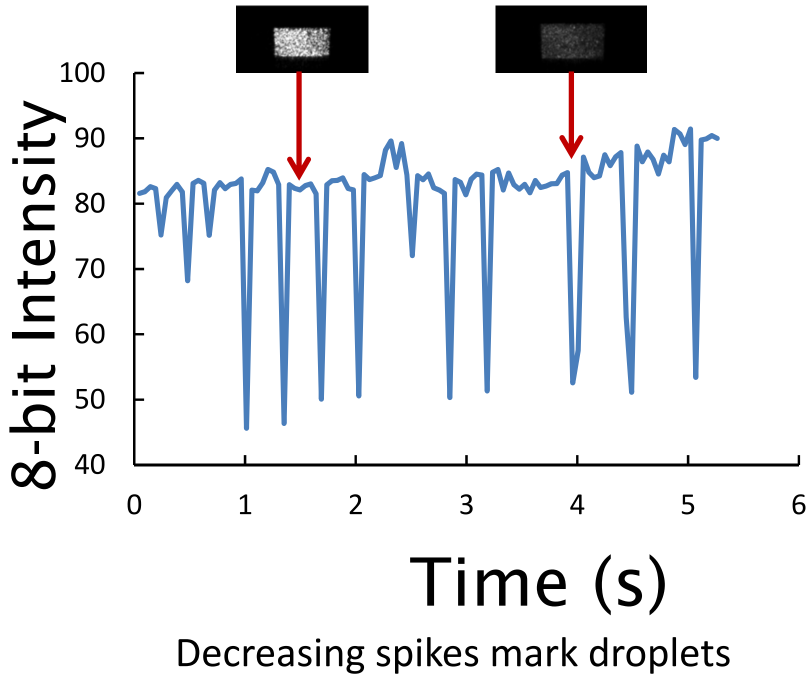

Figure 5.13 Plot of intensity from waveguide as viewed through the microscope. Negative spikes indicate when droplets pass through the waveguide intersection.

5.2.1.3: Future avenues

Further work needs to be done to further characterize droplet detection using waveguides. The type of laser being used as well as the method of detection needs to be optimized to improve upon our preliminary results. Instead of using a microscope, a more sensitive photodiode or photomultiplier tube should be used. This would be more effective than standing the chip on end in the microscope and would eliminate the need for a microscope altogether, making the system transportable.

5.2.2: Photomultiplier tube for sensitive droplet detection via standard optical microscopy

Another method for droplet detection was to use a photomultiplier tube (PMT) detector that was mounted to the Nikon Ti-E microscope. The chip was aligned downstream of the droplet generation portion over the objective. The shutters on the PMT were adjusted so that only a small portion of the channel was being imaged. Even at relatively high droplet formation frequencies, the temporal resolution of the PMT allowed for the detection of individual droplets. This system was used to easily detect changes in droplet frequency (**Figure 5.14).** Frequencies of 40 Hz were easily discernible, and although not as clean and easy to distinguish, frequencies of >100 Hz were detected. Again, this type of system could ideally be combined with the on-chip waveguide channels to give a robust optical droplet detection method to feed signal into droplet control regions (variable fluidic resistors).

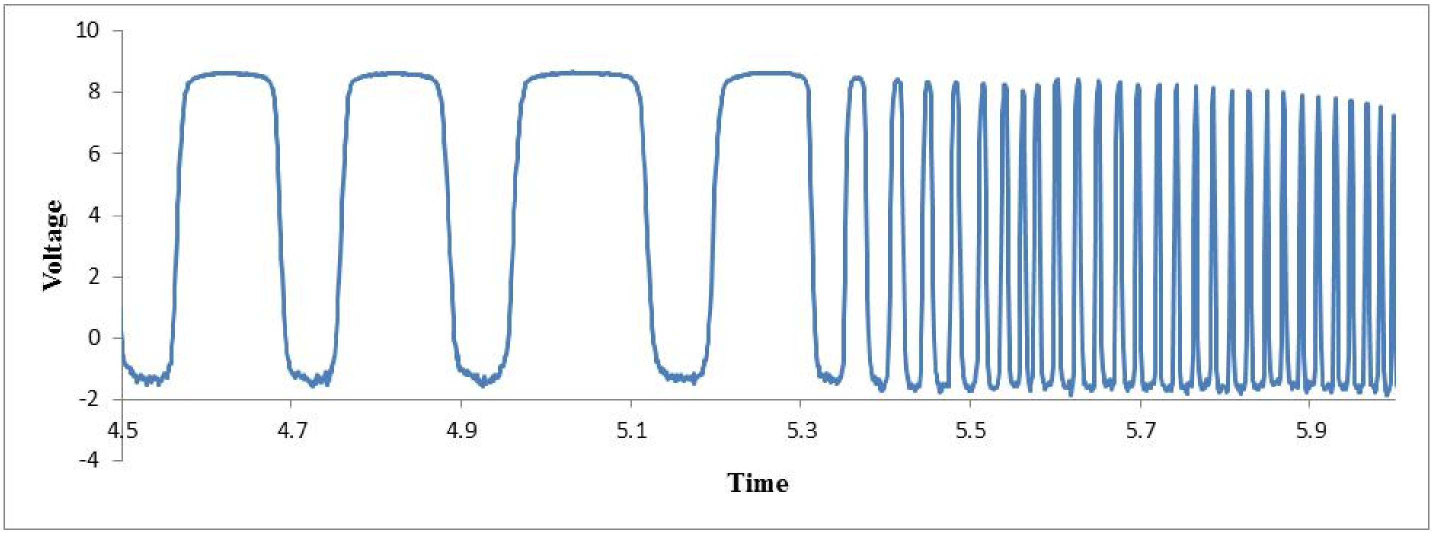

Figure 5.14 Droplet detection using a PMT represented as a voltage in a LabVIEW program. Low vacuum was applied to the droplet outlet first, then a high vacuum was applied at around 5.3 seconds, greatly increasing the droplet formation frequency.

5.3: Conclusions and future work

We have shown in this chapter that droplet frequency and volume can be adjusted on-chip and that droplets can be detected through various optical methods. For future work, there are several immediate questions that should be answered. What are the limits of controlling droplet frequency and formation? What is the most effective method of detecting the droplets? What is the maximum frequency or minimum volume that can be detected by each method? Once these questions have been answered, it should be possible to progress toward a variable resistor-based feedback control system for droplet generation. The end goal would be to develop a single chip and measurement/control system with the ability to control droplets, detect droplets, then use a program such as LabVIEW capable of analyzing detection data, and applying various pressures to the resistors in order to optimize the formation based on user entered parameters.

5.4: References

1. Fei, P.; Chen, Z.; Men, Y.; Li, A.; Shen, Y.; Huang, Y. *Lab Chip* **2012,** 12, 3700-3706.
2. Godwin, L. A.; Deal, K. S.; Hoepfner, L. D.; Jackson, L. A.; Easley, C. J. *Anal. Chim. Acta* **2013,** 758, 101-107.

Chapter 6: Conclusions and Future Directions

6.1: Conclusions

The work that has been presented in this dissertation has proven that a lock-in detection system can be used with droplet-generating microfluidic devices to significantly improve the LODs for systems utilizing absorbance as well as fluorescence detection. Our novel, passive method of alternating sample and reference droplets was key in obtaining these results. This system was applied to absorbance detection at short optical paths, as well as to secretion sampling and protein quantitation from pancreatic islets using fluorescence detection. Also presented were various new methods for device fabrication, a variable fluidic resistor system to control frequency and volume of droplets, and several approaches for droplet detection that progress toward a future servo-type system for on-demand droplet formation and control. Ultimately, these types of improvements in the droplet formation and control systems will be important for the applications at hand in the Easley laboratory, specifically for secretion sampling from endocrine tissue.

6.2: Future Directions

Absorbance and fluorescence methods have been proven feasible with our μChopper system. This suggests promise of being able to apply this method to other optical techniques such as Raman scattering and even to UV or IR detection. Lock-in detection has the potential to expand microfluidics to these methods, which are often prohibited by low sensitivity at short path lengths. Since fluorescence detection has shown promise with insulin secretion detection, the technique involving pFRET assays should be immediately applicable to detect other secreted proteins, as long as the protein of interest has two available antibodies for attachment. Even for insulin secretion sampling, more work needs to be done to improve the methodology and achieve a quantitative hormone detection at high temporal resolution, as well as developing a more consistent and standard method for stimulated secretion of hormones. A new design has been developed to increase incubation times as well as promote more efficient one to one mixing of target and probe (**Figure 6.1).**

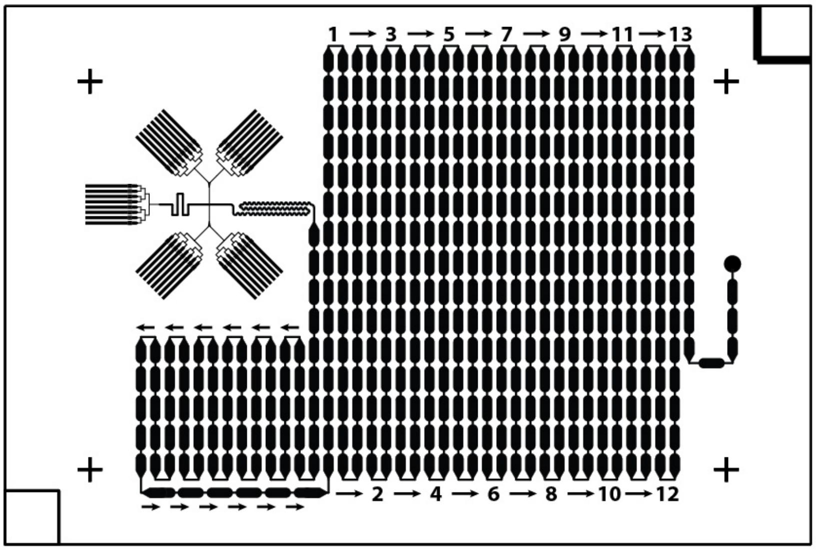

Figure 6.1 New design developed to increase incubation time on chip, promote more effective mixing, and ensure one to one flow rates from the reservoirs.

Once accomplished, it is believed that these methods could be combined with the variable resistor control and real-time droplet detection to be incorporated into a feedback loop system that controls droplet size and frequency automatically and on-demand. A chip could be interfaced with detection devices such as a PMT to determine the size and frequency of droplets, then relay this information to a LabVIEW application capable of applying pressures to each variable fluidic resistor in response to input set points. Frequency and volume set points could be adjusted either direction depending on how the system is responding. A schematic of this hypothetical system is given in **Figure 6.2**. In fact, this system could be directly useful in the secretion sampling application, in order to help with the concentration of hormones in the droplets. For example, if the signal is too low, the volume of the droplets and speed of droplet formation could be decreased by the users in order to increase the concentration of proteins in each droplet.

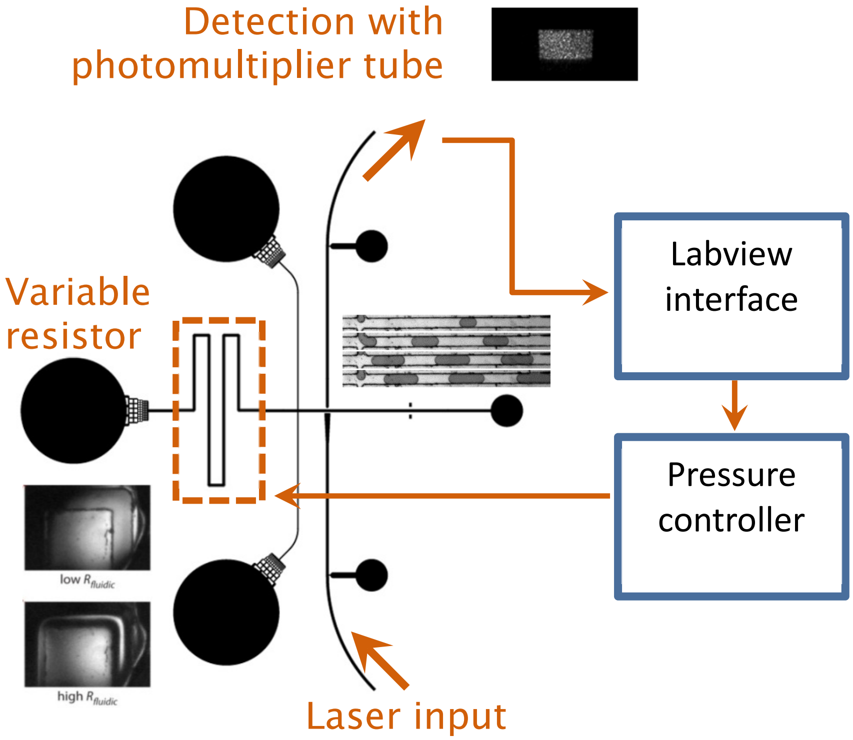

Figure 6.2 Representation of a future combination of variable resistors with droplet detection methods in order to create a feedback loop, allowing a user to enter parameters for droplet volume and frequency. A program capable of analyzing droplet data and optimizing droplet formation by adjusting variable resistors to match user settings is proposed. This design could also be integrated with the secretion sampling application in order to control the speed and volume of droplets containing secreted hormones.

Further work could also be performed on a device that uses 4 or more alternating channels to form droplets (instead of 2 as used in the μChopper). It has been shown successfully that as many as 4 droplet generators can be fluidically coupled and used to spontaneously form alternating droplets in a sequential arrangement (**Figure 6.3)**. It is believed that this design could be used as a calibration device with one channel containing a blank, two channels containing calibration standards, and the fourth channel containing the analyte of interest. In this way, signal from sample droplets could be compared directly to the other 3 droplets at ~10 Hz. Essentially, at frequencies ~10 Hz, instead of just having a constant reference as in typical lock-in detection schemes, we would have a 3-point calibration curve for instant quantitation. In future endeavors, it may be possible to increase the number of alternating droplet channels on chip to greater than 4.

Figure 6.3 Image of droplets output from a 4 aqueous channel alternating droplet chip as it maintains the same repeating pattern in a spontaneous, passively-operated manner.

Appendix 1: Wiring Diagrams for LabVIEW Applications

A1.1 Pressure sensor for lock-in detection

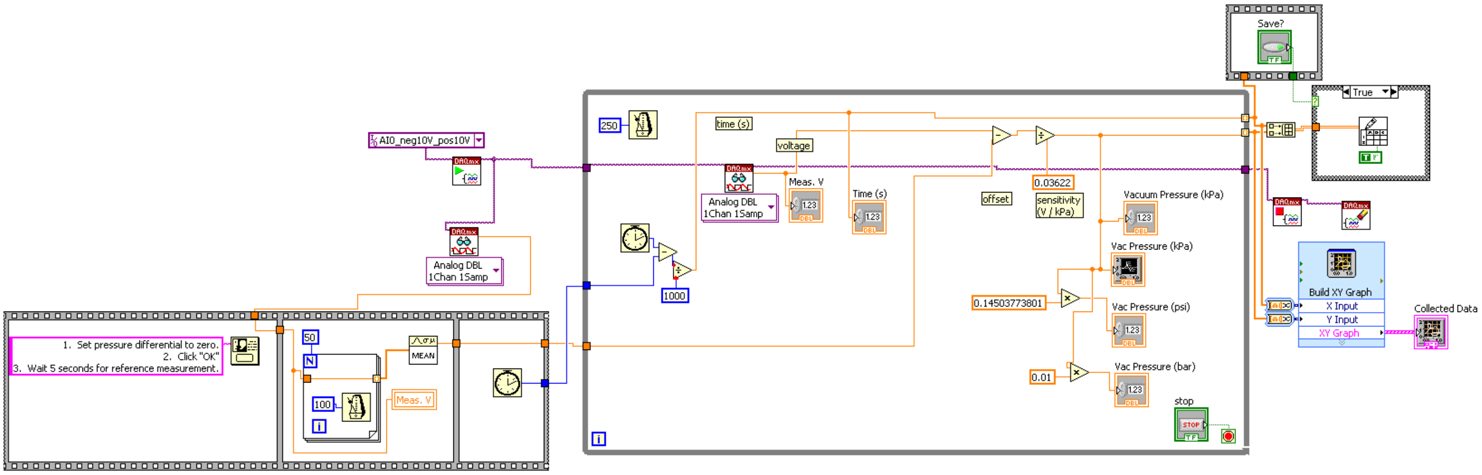

A1.2: Photomultiplier